DYNAMICS OF A COLLAPSING PROTOSTAR

Thesis by

Richard Bondo Larson

In Partial Fulfillment of the Requirements

For the Degree of

Doctor of Philosophy

California Institute of Technology

Pasadena, California

1968

(Submitted 18 March 1968)

ACKNOWLEDGMENTS

I am indebted to my thesis adviser, Dr. Guido Münch, for originally suggesting this topic and for providing guidance and many helpful discussions throughout the course of this work. Other faculty members to whom I am indebted for helpful discussions include Dr. M. Schmidt, Dr. J. B. Oke, and Dr. R. F. Christy. I have also benefitted greatly from discussions with a large number of fellow students in the Astronomy and Physics departments at Caltech. Among these I would particularly like to thank John Castor for discussions on theoretical and computational aspects of the problem, and Eric Becklin and other members of the infrared group for information and discussions on observational aspects.

I would like to thank the staff of the Caltech Computing Center for the courteous and efficient service which they have provided. I have been supported during most of my student days by Institute funds as a Graduate Teaching Assistant.

ABSTRACT

Numerical calculations of the dynamics of a spherically symmetric collapsing protostar have been made for various assumed initial conditions. In all cases the collapse is found to be extremely nonhomologous, the density distribution becoming more and more sharply peaked at the center as the collapse proceeds. As a result, a very small part of the cloud's mass at the center reaches stellar densities and temperatures and stops collapsing before most of the cloud has had time to collapse very far. The central stellar core thus formed subsequently grows in mass as the surrounding material falls into it, finally becoming an ordinary star when all of the original protostellar material has been accreted. During most of this time the forming star is completely obscured by the dust in the infalling cloud, the absorbed radiation reappearing in the infrared as thermal emission from the dust grains. For $M = M_\odot$ the resulting star is almost a conventional Hayashi pre-main sequence model, but it appears quite low on the Hayashi track, at about $R \sim 2R_\odot$. For masses greater than about 2 or $3M_\odot$ the convective Hayashi phase does not exist at all. The emitted spectrum of a protostar has been calculated from a simple approximation for the radiative transfer problem in the infalling cloud, and the results have been compared with some observations which may be relevant. It appears that some observations of infrared objects and some properties of T Tauri stars may be explainable from our results.

TABLE OF CONTENTS

PART III. OBSERVATIONAL APPEARANCE OF A COLLAPSING PROTOSTAR

APPENDICES

PART I: ASSUMPTIONS AND INPUT DATA

1. INTRODUCTION: THE INITIATION OF STAR FORMATION

The process of star formation and the conditions under which star formation begins have been the subject of much speculation, but so far little if any hard factual knowledge on the subject can be claimed. It is generally thought that stars form as the result of the gravitational instability and collapse of condensations or dense regions in the interstellar medium. A condensation with a given temperature can become unstable and collapse gravitationally if it has either a sufficiently large mass or a sufficiently high density, as required by the criterion for gravitational instability first established by Jeans (1928). It is well known that, with the densities and temperatures of typical HI clouds, a mass of at least several hundred solar masses is required for a cloud to collapse gravitationally. On the other hand, the gravitational collapse of only one solar mass requires a minimum density several orders of magnitude higher than typical interstellar cloud densities. It is therefore thought that star formation begins with the collapse of a massive cloud of perhaps several hundred or a thousand solar masses--i.e., a "protocluster." As the density of such a cloud increases, it becomes possible for smaller sub-condensations within the cloud to form and collapse under their own self-gravitation; presumably in this way condensations of one solar mass or less can form and collapse gravitationally into stars.

The conditions under which these subcondensations form and begin to collapse are unknown, except that from the Jeans criterion we can get an idea of the minimum density required. It seems likely that turbulence, quite possibly supersonic, will be of major importance for the formation and early evolution of the sub-condensations in a collapsing protocluster. Since nothing is known about the turbulent flow in such a situation, it is impossible to specify in any detail the proper initial conditions for the collapse of a protostar. In any case the conditions are undoubtedly quite complicated and variable from case to case in details. Thus probably all that one can hope to calculate with any confidence at present is the general features of the collapse, assuming that these general features are not strongly sensitive to the details of the starting conditions (as is confirmed by the results of the present project). In view of this situation, it has for the most part not seemed worthwhile in the present project to consider other than the simplest possible assumptions and idealizations.

Most of the previous investigations of the early stages of star formation, including the recent work of Hayashi (1966) which may be consulted for further references, have assumed complete spherical symmetry for the collapsing protostar and have neglected any effects of rotation, magnetic fields, or internal turbulent motions. In order to make the present project practicable, and because it was thought advisable to tackle first the simplest possible case, these assumptions have been retained in the present calculations. Possibly large deviations from these assumptions, such as rapid rotation, can be rejected from consideration since such effects might prevent the material from collapsing at all or cause it to collapse into several stellar objects. Nevertheless it is difficult to justify the complete neglect of rotation, magnetic fields, deviations from spherical symmetry, etc. on any other basis than simplicity; in fact, rotation at least seems certain to be an important effect in general. Thus in neglecting all these phenomena we are clearly restricting ourselves to a highly idealized case which may at best be realistic for only a very few real stars.

It has usually been imagined that some sort of spherical hydrostatic equilibrium configuration might be a suitable approximation for the initial state of a protostar; most authors have assumed the initial state to be either an isothermal sphere or a polytropic sphere. It seems doubtful however whether hydrostatic equilibrium can be of much relevance for the early stages of a protostar, since this presupposes quiescent conditions and changes which are slow compared to the free fall time. Such conditions seem unlikely to exist in our collapsing protocluster, in which overall collapse and internal turbulent motions are expected to occur on roughly the free fall time scale. Thus hydrostatic equilibrium may never exist, and a protostellar condensation when formed may already be collapsing at an appreciable rate. We note that if there is no hydrostatic equilibrium, there is no physical basis for the assumption of spherical symmetry.

Thus there seems to be no firm basis for the type of assumptions which have usually been made concerning the initial conditions for a protostar, or indeed for any other simple assumptions.

Fortunately it turns out from the results of this project that, at least within the range of assumptions considered, the details of the assumed starting conditions are not of critical importance, and it appears that rather arbitrary simple choices of these conditions may be made without altering the general features of the results. The various initial conditions and boundary conditions which have been used in this project and the ones we consider least unrealistic will be discussed in detail in sections 4 and 5. First, however, we shall discuss in some detail in sections 2 and 3 the assumed physical properties of the protostellar material.

2. PHYSICAL PROPERTIES OF THE PROTOSTELLAR MATERIAL

2.1 Composition and Equation of State

In this and the following sections we shall discuss the physical properties (composition and equation of state, opacity, and temperature) expected for the material of a protostar of mass near one solar mass. These properties have already been discussed by Gaustad (1963), Hayashi and Nakano (1965), and Hayashi (1966), and to a considerable extent the results of these authors form the basis for the present work.

We shall assume, as do the above authors, that we are dealing with star formation in an HI region with typical population I composition. We adopt Gaustad's composition, for which the mass fractions of hydrogen, helium, and heavier elements are $X = .65$, $Y = .32$, and $Z = .03$ respectively. It is assumed that at the rather high densities ($\gtrsim 10^{-19}$gm/cm^3) required for the gravitational collapse of one solar mass the hydrogen will be essentially all in molecular form. (In order to find the effect of this assumption, one collapse calculation was made in which no molecular hydrogen was assumed to exist at any time.) Dust grains are assumed to exist with the properties adopted by Gaustad, namely a grain radius of 2×10^{-5} cm and an abundance of 3×10^{-13} grains per atomic mass unit or 1.8×10^{11} grains per gram of material. With Van de Hulst's (1949) assumed grain density of 1.1 gm/cm^3, this implies that the grains constitute 0.7% of the total mass of the material.

The equation of state of the protostellar material (essentially hydrogen with a small admixture of helium) is well known over most of the range of temperatures and densities encountered in this work, and need not be discussed in detail here; detailed discussion of the equation of state is given in Appendix C. Throughout the early stages of the collapse the material satisfies the perfect gas law $P = \rho \mathfrak{R} T$ where the gas constant $\mathfrak{R}$, for future reference, is equal to 3.36×10^7 (cgs). At higher temperatures molecular dissociation and ionization are of great importance, and they must of course be taken into account in the appropriate temperature and density ranges. The complete equation of state adopted in the calculations, which contains some approximations, is described in Appendix C.

2.2 Opacity

The opacity of the material in the early stages of star formation has been studied by Gaustad (1963), and for the most part the opacities used in the present work have been based on the work of Gaustad. Gaustad found that as long as dust grains exist at all, they are the dominant source of opacity. He attempted to derive theoretically the probable composition and the infrared absorption coefficient of the dust grains. At the lowest temperatures (up to about 120 - 150 °K, depending on density), solid H_2O can exist, and it was assumed by Gaustad to be the main constituent of the grains and the primary contributor to the absorption. Gaustad gives the absorption coefficient for grains of pure solid H_2O as a function of wavelength, and Rosseland mean absorption coefficients based on these data are given as a function of temperature by Hayashi and Nakano (1965). Unfortunately there seems to be observational evidence that H_2O is not a primary constituent of the interstellar grains (Danielson, Woolf, and Gaustad 1965). The absorption data assuming H_2O grains must therefore be considered as very uncertain. Nevertheless, there do not appear to be any better data available for the absorption coefficient of the dust grains at the far infrared wavelengths relevant for the present situation.

At temperatures above about 150 °K, H_2O evaporates and the main constituent of the grains, according to Gaustad, is $MgSiO_4$. Experimental data for the infrared absorption coefficient of $MgSiO_4$ are available only in a small wavelength range centered near 10 μ. Gaustad has attempted extrapolation of these data and calculated Rosseland mean absorption coefficients at 500 °K and 1500 °K. However, a look at the actual data shows that reliable extrapolation is impossible, and the resulting Rosseland means must be exceedingly uncertain, perhaps by orders of magnitude. Again, however, there seem to be no other data available for the "mineral grains" envisioned by Gaustad. $MgSiO_4$ and the other possible mineral grain constituents evaporate at temperatures of 1200-1500 °K, depending again on density. Gaustad concluded that solid carbon would not form and that therefore there would be no solid grains at all above about 1500 °K.

Clearly the infrared dust absorption properties are highly uncertain. It is doubtful even whether the types of grains envisioned by Gaustad actually exist. Alternative theories of the grains have been proposed, and one of them in particular, the graphite core-ice mantle model, seems to have gained some observational support

(Krishna Swamy and O'Dell 1967). If this model is correct, then at the higher temperatures the grains would probably consist mainly of graphite, which evaporates at 2100-2500 ^{o}K. Fortunately the dynamics of the later stages of the collapse and the properties of the resulting star turn out to be insensitive to the dust opacity over the whole temperature range above about 100 ^{o}K (at least within the approximations we have used for the radiation transfer; see section 8.3). It is therefore believed that no serious errors arise from the use of Gaustad's opacity data, even though they may be wrong.

Knowledge of the dust absorption properties is of course important in treating the radiation transfer in the collapsing cloud and in calculating the spectrum of the radiation emitted from it. This problem can fortunately be separated from the calculation of the dynamics, at least during the later stages of the collapse, and we shall consider it separately in Part III, where discussion of the grain absorption coefficient will again be taken up.

When the dust grains evaporate the opacity depends on a variety of atomic and molecular processes. Gaustad concluded that the main contributions to the opacity in the temperature range 1500-3000 ^{o}K would come from H^- and H_2^- absorption and Rayleigh scattering of H_2, and that molecular absorption bands would be unimportant. More detailed work by Yamashita (1962) and Tsuji (1966) has shown that Gaustad underestimated the molecular absorption coefficient, which in the molecular absorption bands may be many orders of magnitude greater than the absorption without molecules. However, because radiation can still come through between the molecular absorption bands, the effect of molecules on the Rosseland mean opacity, while uncertain, is considerably reduced and may not exceed one order of magnitude. At any rate, the various available calculations of the Rosseland mean opacity above 1500 $^{\circ}$K, with and without molecules (Gaustad 1963, Yamashita 1962, Tsuji 1966, and Cox 1966) are in fair agreement (within about one order of magnitude), and the opacity in the temperature range 1500-3000 $^{\circ}$K can therefore probably be considered as known to an accuracy adequate for the present work, where it is not of great importance. At temperatures above 3000 $^{\circ}$K the opacity is relatively well known; in the present work the calculations of Cox (1966) have been used.

Gaustad's data for the opacity due to dust grains are plotted as a function of temperature in Fig. 1 (p. 10). The curve for $T \leq 150$ $^{\circ}$K is the Rosseland mean opacity for H_2O grains as tabulated by Hayashi and Nakano (1965), multiplied by 3 to make it consistent with Gaustad's grain abundance. The two open circles at 500 $^{\circ}$K and 1500 $^{\circ}$K are Gaustad's calculations for $MgSiO_4$ grains. Because of the large uncertainty in Gaustad's data, and because it was soon found that the general features of the collapse of a protostar were not strongly sensitive to the grain opacity, it was not thought worthwhile to accurately represent Gaustad's data, and a simple constant value for the grain opacity was adopted: $\kappa_R = 0.15$ cm^2/gm. This is shown by the horizontal straight line in Fig. 1. The grains were assumed to evaporate at 1400 $^{\circ}$K. (To find the effect of uncertainties in the grain opacity or in the grain abundance, one collapse calculation was made with the dust opacity reduced two orders of magnitude

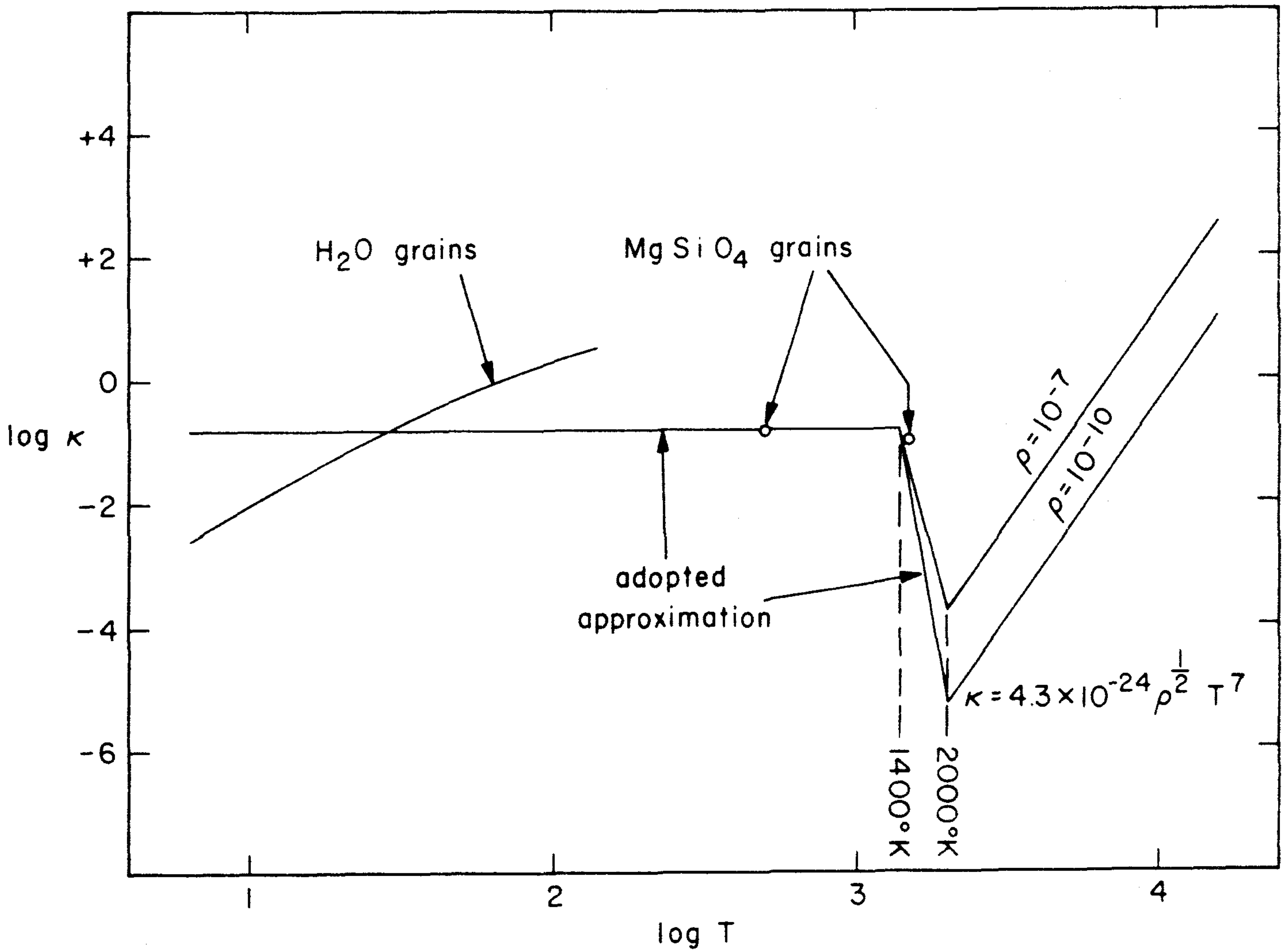
+4
+2
0
-2
-4
-6
log κ
1
2
3
4
log T
H_2O grains
$MgSiO_4$ grains
adopted approximation
$\rho=10^{-7}$
$\rho=10^{-10}$
$\kappa=4.3\times10^{-24}\rho^{\frac{1}{2}}T^{7}$
1400°K
2000°K

FIGURE 1

Fig. 1 (p. 10): The assumed Rosseland mean opacity of the protostellar material as a function of temperature. The unit for κ is cm^2/gm and the unit for T is ^oK. The curved line on the left side of the diagram shows the Rosseland mean opacity for H_2O grains as calculated by Hayashi and Nakano (1965) using the data of Gaustad (1963). The two open circles are Gaustad's calculations for $MgSiO_4$ grains. The approximation adopted for use in the calculations is illustrated by the straight lines in the figure; see text for explanation.

to 0.0015 cm^2/gm.)

At temperatures between about 2000 ^{o}K and 8000 ^{o}K the available data, if averaged and smoothed somewhat, are roughly represented by the following simple power law:

$$\kappa_R = 4.3 \times 10^{-24} \rho^{\frac{1}{2}} T^7 \ cm^2/gm \qquad (2.1)$$

This formula was adopted for $T \geq 2000\ ^{o}K$ and is shown for $\rho = 10^{-7}$ and 10^{-10} gm/cm^3 by the two parallel straight lines on the right side of Fig. 1. This rough formula represents the opacity within approximately a factor of 2 at the most important temperatures and densities, although it may be in error by an order of magnitude or more at other temperatures and densities. Again, because of uncertainties in the data and because accurate opacities are not of critical importance for the present purposes, it was not thought worthwhile in most of the calculations to use a more accurate representation of the opacity.

Equation (2.1) gives opacities which are much too large for $T \gtrsim 10^4\ ^{o}K$. For a star of one solar mass this makes no difference until the star gets close to the main sequence because it turns out that radiation transfer in material with $T \gtrsim 10^4\ ^{o}K$ is of negligible importance anyway during the whole course of the collapse. For stars of larger mass and for a star of one solar mass near the main sequence it is necessary to use the correct high temperature opacities; in these cases a complete tabular representation of the opacity based on the calculations of Cox (1966) has been used for $T \geq 2000\ ^{o}K$.

Finally, in place of a discontinuous drop in opacity at the assumed grain evaporation temperature of 1400 °K, a logarithmically linear interpolation between the grain opacity at 1400 °K and the power law formula at 2000 °K has arbitrarily been made, as shown in Fig. 1. This was done mainly because of numerical difficulties sometimes encountered with the discontinuous drop, but in view of the great uncertainties involved and the fact that the time required for evaporation of the grains is not always negligible, perhaps the gradual drop in opacity is no more unrealistic than the discontinuous drop.

3. THERMAL BALANCE AND TEMPERATURE DURING THE EARLY STAGES OF THE COLLAPSE

It is generally believed, mainly on the basis of 21 cm observations, that the gas in typical interstellar HI regions has a temperature of the order of 100 $^{\circ}$K. This value however is not necessarily relevant for the early stages of a protostar of one solar mass, because such a protostar must start with a density much higher than that of typical interstellar HI clouds, and at these higher densities different processes are of importance in determining the temperature. The heating and cooling processes and the expected temperature have been discussed by Hayashi (1966); we discuss the situation again below, but the results will not be very different from Hayashi's.

We consider first the heating mechanisms. In normal HI clouds the gas is thought to be heated by photoionization caused by absorption of starlight. However if we take Gaustad's grain parameters and the grain absorption coefficient given by Van de Hulst (1949) for his theoretical curve #15, we find that, even at the minimum density of about 10^{-19} gm/cm^3 required for the collapse of one solar mass, the protostar has a center-to-surface optical depth at 5000 Å of about 4. If we consider the whole protocluster, its optical depth will be several times larger. Therefore the heating effects of absorption of starlight will be greatly reduced for both the gas and the dust grains, and we shall neglect this source of heating.

A second heating process which may still be important is ionization by cosmic ray particles. The cosmic ray heating rate adopted by Hayashi is $\Gamma_{CR} = 10^{-5}$ ergs/gm/sec; this value is a lower limit based only on the observed flux of cosmic rays at energies above a few Bev. Hayakawa et al. (1961) showed that unobserved cosmic rays of lower energy can be quite important; on the basis of a rather arbitrary extrapolation of the cosmic ray spectrum to lower energies, they obtained a cosmic ray heating rate three orders of magnitude higher, i.e. $\Gamma_{CR} \approx 10^{-2}$ ergs/gm/sec. This value may be too high, even assuming the hypothesized cosmic ray spectrum, since it appears on the basis of data given by Hayakawa et al. that the lower energy cosmic rays mainly important in this case may be subject to significant absorption. We shall therefore consider Hayakawa's value as an upper limit, and in estimating the temperature we shall consider the following two limiting cases: (a) $\Gamma_{CR} = 10^{-5}$ ergs/gm/sec, and (b) $\Gamma_{CR} = 10^{-2}$ ergs/gm/sec.

A third heating mechanism which is of essential importance in the present circumstances is compressional heating of the material as it collapses gravitationally. The collapse is expected to be almost a free fall; the free fall compressional heating rate for material with the adopted composition is

$$\Gamma_{ff} = 7.5 \times 10^{4} \rho^{\frac{1}{2}} T \text{ ergs/gm/sec} . \tag{3.1}$$

We now consider the cooling processes. An important process in normal HI clouds is electron collisional excitation of fine structure transitions in ions such as C^{+}, followed by radiative de-excitation (Seaton 1955). In the present circumstances this process is reduced in importance because the electron and ion densities are reduced due to the absence of ionizing stellar radiation, and because at these high densities the optical depth for the emitted line radiation becomes large. The effectiveness of this process is thus uncertain, but it is probably not of major importance and will be neglected here. If this or similar processes should contribute significantly, the temperature could be reduced somewhat at the lowest densities considered, but this would not affect our major conclusions, except perhaps to strengthen them.

A second radiative cooling process which may still contribute significantly and which we shall take into account is cooling by H_2 molecules. For our adopted composition and in the relevant density range the H_2 cooling rate is

$$\Lambda_{H_2} = 1.67 e^{-512/T} \text{ ergs/gm/sec} . \tag{3.2}$$

The cooling process which turns out to be most important at the high densities relevant here is the collisional transfer of energy from the gas molecules to the cooler dust grains. Assuming that the colliding molecules leave the grains with a kinetic energy corresponding to the grain temperature, the energy transfer rate is

$$\Lambda_g = 1.1 \times 10^{14} \rho T^{\frac{1}{2}} (T - T_g) \text{ ergs/gm/sec} \tag{3.3}$$

where T_g is the grain temperature. The grain temperature is determined by the balance between heating of the grains by the above process and cooling of the grains by thermal emission at the rate

$$j = 2.3 \times 10^{-4} \kappa_p T_g^{\,4} \text{ ergs/gm/sec} \tag{3.4}$$

where κ_p is the Planck mean opacity for the dust grains. Values of κ_p for the present calculations have been taken from the tabulation of Hayashi and Nakano (1965), somewhat extrapolated where necessary and multiplied by 3 to make it consistent with Gaustad's grain abundance. In the early stages of the collapse the cloud is optically thin at the far infrared wavelengths where radiation from the grains is emitted, so radiation transfer effects need not be considered.

The temperatures of the gas and of the dust grains in thermal equilibrium are then determined by the following two equations:

$$\Gamma_{CR} + \Gamma_{ff} = \Lambda_{H_2} + \Lambda_g \tag{3.5}$$

$$\Lambda_g = j \quad . \tag{3.6}$$

Actually, in the situation envisioned, with the material collapsing in free fall and changing in temperature, we do <u>not</u> have thermal equilibrium, and the equations should really include a term in dT/dt. In the present case this term makes no essential difference to the results and will be neglected.

The temperatures calculated from equations (3.5) and (3.6) are shown in Table 1 (p. 18) as a function of density over the relevant density range. In case (a) it turns out that cosmic ray heating and H_2 cooling are of negligible importance at all the densities considered, and the temperature is determined just by the balance between compressional heating and cooling by dust grains. For $\rho \gtrsim 10^{-19}$ gm/cm^3 the collisional transfer of energy from gas molecules to dust grains becomes very effective and brings the gas

TABLE 1

TEMPERATURES OF GAS AND DUST DURING EARLY STAGES OF COLLAPSE OF A PROTOSTAR

	(a) $\Gamma_{CR} = 10^{-5}$		(b) $\Gamma_{CR} = 10^{-2}$	
log ρ	T	T_g	T	T_g
-20	48.3	4.8	99.5	5.6
-19	12.7	4.7	85.3	7.4
-18	7.0	5.1	28.6	7.9
-17	6.5	5.9	11.4	7.9
-16	7.2	7.0	8.8	8.3
-15	8.5	8.5	9.1	9.0
-14	10.2	10.2	10.4	10.4
-13	12.3	12.3	12.4	12.4
-12	14.9	14.9	14.9	14.9

temperature down close to the dust temperature, which is always of the order of 10 °K and is only weakly sensitive to the heating rate. In case (b), H_2 cooling is important for the first two entries in Table 1 and cosmic ray heating is important up to about 10^{-16} gm/cm^3. Even with the high cosmic ray heating rate, however, cooling by dust grains again dominates and brings the gas temperature down to near 10 °K for densities $\gtrsim 10^{-17}$ gm/cm^3.

Rather similar results are obtained under various assumptions by Hayashi and Nakano (1965) and Hayashi (1966); Hayashi for example considers both transparent and opaque cases, and in both cases he gets temperatures of the order of 15 °K at the relevant densities. In fact a similar result will always be obtained as long as dust grains are assumed to exist and as long as the density is high enough, i.e. greater than about 10^{-19} or 10^{-18} gm/cm^3, because of the great effectiveness of molecule-grain collisions in equalizing the gas and dust temperatures.

As will be shown in section 5, if we assume a temperature of 10 °K the minimum initial density required for the gravitational collapse of a protostar of one solar mass is about 10^{-19} gm/cm^3. Hence we see from Table 1 that in case (a) the temperature will remain near 10 °K throughout the early stages of the collapse, i.e. until the central part of the cloud becomes optically thick in the far infrared, which happens at a central density of about 10^{-14} or 10^{-13} gm/cm^3. In the collapse calculations it has been assumed that throughout the early optically thin stages of the collapse the cloud remains isothermal at a fixed temperature, taken in most cases to be

10 °K. In reality the cloud will not be strictly isothermal because the density and the collapse rate vary throughout the cloud, but Table 1 shows that the temperature is not very sensitive to the heating rate, so that the isothermal assumption should be a reasonably good approximation.

If the cosmic ray heating rate is much higher, as in case (b), the initial temperature will be higher than 10 °K and the initial density must therefore also be higher than 10^{-19} gm/cm^3. A consistent set of starting values for case (b) would be a density slightly over 10^{-18} gm/cm^3 and a temperature of about 25 °K. It is clear from Table 1, however, that as soon as the collapse starts the temperature will start to drop, and it will soon reach approximately 10 °K as before. Thus it may still not be a bad approximation to assume a temperature of 10 °K throughout the early stages of the collapse. The main effect of the higher cosmic ray heating rate will be that a somewhat higher initial density is required to start the collapse.

In order to explore the effect of uncertainty in the temperature during the early stages of the collapse, and to allow for the possibility of some large error in our estimation of this quantity, one collapse calculation was made with an initial temperature of 100 °K instead of 10 °K, with a corresponding initial density of 10^{-16} gm/cm^3 instead of 10^{-19} gm/cm^3.

4. BOUNDARY CONDITIONS

In calculating the dynamics of a collapsing protostar we have a combination initial and boundary value problem: the state of the material must be specified completely at the initial instant, and conditions at the boundary must be specified at all times during the collapse. In reality, in the turbulent field of motion in which protostars begin to condense there is no well-defined "initial instant" at which a particular region begins to condense as a single protostar, and likewise there is no well-defined surface constituting its "boundary." In fact, "initial instant" and "boundary" are rather artificial concepts which arise when we attempt to separate out from the complicated flow field a particular region, to be called a "protostar," which for simplicity we wish to study as a separate entity and represent by a simple mathematical model. Thus the initial and boundary conditions are subject to some arbitrariness of choice, depending on just how one chooses to define the initial instant and the boundary.

We discuss first the treatment of the boundary. We shall arbitrarily take our boundary to be a spherical surface enclosing a given fixed mass, eg. one solar mass, and moving with the material as it expands or contracts. This choice has been made because it seemed most natural and because the Lagrangian computational scheme initially used in the collapse calculations requires conditions to be specified at points which move with the material. It should be noted, however, that when the boundary is chosen in this way it is not necessarily true that the boundary will contract as the collapse proceeds or even that all of the material inside the boundary will collapse into a star; under some conditions the outer part of the cloud may expand as the inner part contracts, and the resulting star may end up with considerably less than one solar mass.

The important boundary condition is the pressure exerted on the boundary of the collapsing protostar by the surrounding material, if any; this is of dominant importance in determining the motion of the boundary and the material in the outer parts of the cloud. Three types of boundary conditions have been considered in this project:

(a) The protostar is assumed to be surrounded by a vacuum, i.e. there is assumed to be zero pressure on the boundary. Since the boundary temperature is finite, even though the density may go to zero, there can be no hydrostatic balance with zero boundary pressure, as has sometimes been imagined; the pressure gradient always wins over the gravitational force and the boundary material is immediately blown off at roughly the speed of sound. Such a situation seems hardly likely to arise in the first place, but even if something like this does happen, it would seem more appropriate to choose as the boundary of the protostar some mass level farther inside the cloud where the material does not immediately start to expand. Therefore calculations with this boundary condition were pursued only far enough to show that the interior part of the cloud which does still collapse does so in much the same way as in the other cases tried.

(b) It would seem more realistic to suppose that our collapsing protostar is surrounded by material which exerts a finite pressure on its boundary. The one solar mass of interstellar material destined to become a collapsing protostar can achieve the required initial density of 10^{-19} gm/cm^3 only through being compressed by surrounding material, and presumably this surrounding material would be still present and still exerting pressure on the boundary when the protostar starts to collapse gravitationally. One simple assumption which may be considered is that there is a finite boundary pressure which is equal to the initial pressure just inside the boundary and remains constant in time as the protostar collapses. This assumption was used in most of the early calculations in this project because of its simplicity in Lagrangian form. In this case the boundary is continuously accelerated inward by the pressure of the external material. However this assumption may again be unrealistic since it would seem that the pressure of the surrounding material should decrease as most of it condenses into stars. Thus perhaps case (a), in which the boundary expands, and case (b), in which it contracts, may be regarded as limiting cases, with something intermediate probably more realistic.

(c) A possible intermediate case is one in which there is a finite outside pressure sufficient to keep the boundary from expanding but not large enough to make it contract; i.e., the boundary remains fixed in space. This corresponds to allotting a constant volume to each collapsing protostar in a protocluster, which seems reasonable, assuming that the protocluster stops contracting as a whole when it fragments into stars. Actually the fixed boundary assumption was first introduced when it was found necessary in calculating the later stages of the collapse to switch to an Eulerian computational scheme, which requires that conditions be specified at points fixed in space. Because it seemed more realistic than the other assumptions considered and because it was the easiest one to use in the Eulerian computational method, the fixed boundary assumption was eventually adopted for use throughout the collapse calculations.

5. INITIAL CONDITIONS

As the initial conditions for the collapse of a protostar it is necessary to specify initial values for the temperature, density, and velocity at all points within the protostar. The temperature has already been discussed in section 4; we have assumed the temperature to be initially uniform and equal in most cases to 10 °K. As for the initial velocity, we have assumed for simplicity that the protostar starts from rest, i.e. with zero initial velocity. This assumption is not necessarily very realistic since, as was pointed out in section 1, the protostar may already be collapsing at a significant rate when it forms. However the initial velocity distribution is not expected to have any important effect on the general features of the collapse, once the collapse is well under way; some calculations made with the cloud initially contracting or expanding showed no essential difference from other cases in the nature of the collapse, once the collapse was well under way.

We now consider the initial density distribution. It was pointed out in section 1 that the polytropic or isothermal sphere density distributions which have usually been assumed are probably not particularly relevant. Instead it appears more likely that during the initial stages of a protostar the density distribution changes more or less rapidly without ever coming into hydrostatic equilibrium. The one solar mass of material destined to collapse into a star may at a very early stage appear as a density perturbation or a compressed region in a turbulent flow, with probably little or no central condensation.

If its density is high enough, its self-gravitation will start it collapsing and begin to produce a centrally peaked density distribution. This density perturbation will of course be subject to disturbing influences, and an enduring existence as a gravitationally coherent object may not be ensured until it has already built up some kind of central density peak; in this event there is some problem in just what stage should be considered as the initial state of a collapsing protostar. For simplicity and definiteness we have imagined the initial state to be a very early stage when the density perturbation has just appeared but its self-gravitation has not yet had time to produce a significant central condensation, and we have accordingly assumed a uniform initial density distribution in all of the calculations. Again this assumption is not expected to be of critical importance, and there are reasons from the results for believing that the initial density distribution doesn't make much difference once the collapse is well under way.

Some support for the above assertions about the non-critical nature of the initial density and velocity distributions is provided by the work of Penston (1966). He computed the early stages of the collapse of an isothermal gas sphere with several choices of initial conditions different from those considered here. While there are of course some quantitative differences, the qualitative features of the collapse as computed by Penston are quite similar in the various cases and similar also to the results obtained in the present project.

We have now only to specify the value of the uniform initial density with which the calculations are to be started. For a cloud of given mass and temperature, such as we are considering, a certain minimum density is required in order for gravitational forces to overcome pressure forces and make the cloud collapse gravitationally. This minimum density can be estimated either by the Jeans gravitational instability criterion or by application of the virial theorem.

We consider first the Jeans criterion. Derivation of the Jeans gravitational instability criterion for spherical density perturbations has been given by Bonnor (1957) for a particular assumed radial dependence of the perturbation amplitude. The resulting minimum density for instability of a spherical density perturbation with mass M, temperature T, and gas constant $\Re$ is

$$\rho = \frac{3}{4\pi}\left(\frac{\pi^2}{3}\,\frac{\Re T}{G}\right)^3 \frac{1}{M^2} = 2.7 \times 10^{-19}\ \mathrm{gm/cm^3} \qquad (5.1)$$

where we have substituted $M = M_\odot$, $T = 10\ {}^\circ K$, and $\Re = 3.36 \times 10^7$ (cgs).

The other way to estimate the initial density is to imagine a cloud in which gravitation just balances pressure forces, so that there is no net tendency toward expansion or contraction, and apply the virial theorem to find the corresponding density. (Hydrostatic equilibrium is not implied by this "balance"; it need only be that a tendency to contract in one part of the cloud is balanced by a tendency to expand in another part.) Considering first an isolated cloud with no external pressure, the virial theorem is $2K + \Omega = 0$, where K is the total thermal kinetic energy and Ω is the gravitational potential energy. (We have neglected any effects of rotation, magnetic fields, or internal mass motions.) Assuming a uniform density, this gives an initial density of

$$\rho = \frac{3}{4\pi}\left(\frac{5\Re T}{G}\right)^3 \frac{1}{M^2} = 9.5 \times 10^{-19} \text{ gm/cm}^3 , \qquad (5.2)$$

using the same values as above for the parameters.

We have seen however that it would be more realistic to assume a finite external pressure on the cloud. In this case an extra term must be inserted in the virial theorem, as was shown by McCrea (1957); it now becomes $2K + \Omega = 3PV$, where P is the boundary pressure and V is the volume of the cloud. Clearly the existence of a finite external pressure allows gravitational collapse to start from a lower initial density. In fact, if we assume a uniform initial density and set the initial boundary pressure equal to the (uniform) internal pressure, as required by the boundary conditions (b) or (c) discussed in section 4, the virial theorem predicts that collapse can start from an arbitrarily low initial density. While it is true that the cloud will always start to collapse, what happens subsequently if the denstiy is too low is that pressure gradients soon build up sufficiently to stop the collapse, and the cloud then rebounds and oscillates about a hydrostatic equilibrium configuration without ever collapsing to a star. Thus the virial theorem alone does not in this case establish a minimum density sufficient to ensure collapse all the way to a star.

A sufficient condition for collapse to a star has been established by the work of Ebert (1955), Bonnor (1956), and McCrea (1957). Their result may for our purposes be re-expressed as follows:

Consider an isothermal gas cloud of mass M and temperature T confined by an external pressure to a spherical volume of radius R. Then for large enough R (small enough mean density), the material can always arrange itself in a hydrostatic equilibrium configuration which is stable against gravitational collapse. However there is a critical radius R_c such that if the cloud is compressed to a radius smaller than R_c, stable hydrostatic equilibrium is no longer possible and the cloud must collapse, no matter what the initial density and velocity distributions. The critical radius is given by

$$R_c = 0.41 \frac{GM}{\Re T} = 1.63 \times 10^{17} \text{ cm}, \tag{5.3}$$

and the corresponding mean density is

$$\rho_c = \frac{3}{4\pi}\left(\frac{\Re T}{0.41\, G}\right)^3 \frac{1}{M^2} = 1.10 \times 10^{-19} \text{ gm/cm}^3, \tag{5.4}$$

again with the same values of the parameters as above.

Thus with our fixed boundary assumption a sufficient condition for collapse to a star is an initial density greater than ρ_c. This is however not a necessary condition; with our assumed initial conditions, for example, the cloud starts off far out of hydrostatic equilibrium, and by the time pressure gradients have built up sufficiently to support an equilibrium there is already a substantial collapse velocity, which enables the material to continue collapsing even from an initial density somewhat lower than ρ_c. In order to find the minimum initial density (or maximum radius) from which collapse can take place assuming a fixed boundary and starting with a uniform density and zero velocity, a number of trial collapse calculations were made. Different values for the radius R were tried until a value R_{max} was established such that for $R < R_{max}$ the cloud collapses all the way to a star whereas for $R > R_{max}$ it rebounds and oscillates without ever collapsing to a star. The resulting empirical value of R_{max} was found to be

$$R_{max} = 0.46 \frac{GM}{\Re T} = 1.83 \times 10^{17} \text{ cm}; \qquad (5.5)$$

the corresponding minimum initial density is 7.9×10^{-20} gm/cm^3.

If we assume a protostar to begin its collapse as soon as the density becomes high enough, then the radius and density given just above could be considered the appropriate starting values. Actually, it was found that when the calculations were started with a value of R close to R_{max}, small inaccuracies due to the necessarily coarse space and time steps could shift the sensitive balance and make the cloud rebound instead of collapse. In order to avoid this difficulty, and because R_{max} is not very different from R_c anyway, the cloud radius was for most of the calculations set equal to R_c as given by eqn. (5.3).

SUMMARY OF ASSUMPTIONS

Before proceeding to describe the calculations, we shall summarize here the major assumptions which have been made for most of the calculations, as discussed in detail in the past few sections.

(1) Spherical symmetry has been assumed throughout, and no non-spherically symmetric motions or forces have been considered. In particular, we have neglected (a) rotation, (b) magnetic fields, and (c) internal turbulence.

(2) The material is assumed to remain isothermal throughout the early optically thin stages of the collapse. A temperature of 10 °K has been assumed in most cases, but a temperature of 100 °K has also been tried.

(3) The boundary is in most cases assumed to remain fixed in space at a constant radius R. A constant boundary pressure has also been tried as a boundary condition.

(4) The density is assumed to be initially uniform, and the collapse is assumed to start from rest. The initial density is assumed in most cases to be given by eqn. (5.4).

PART II: DYNAMICS OF THE COLLAPSE

6. EQUATIONS AND APPROXIMATIONS FOR THE EARLY STAGES OF THE COLLAPSE

6.1 The Lagrangian Equations

In this project we have used the equations of fluid dynamics in both the Lagrangian and Eulerian forms; accordingly we shall give both forms of the equations, starting with the Lagrangian equations. In the Lagrangian formulation the physical variables describing the flow are referred to a coordinate system embedded in the fluid and moving with it, so that a particular "fluid particle" is always labeled with the same Lagrangian coordinates. In our spherically symmetric problem, the Lagrangian coordinate for a particular spherical surface is most conveniently taken as the mass m contained inside that surface. The differential equations then give the rate of change of the physical variables and of the radius r on a surface of constant m as it expands or contracts with the flow. The Lagrangian differential equations are given below in the form most closely related to the difference equations used in the calculations. In writing these equations we allow for heat transport by radiation or other means but not for nuclear or other non-mechanical energy sources.

$$\frac{\partial r}{\partial t} = u \tag{6.1}$$

$$\frac{\partial u}{\partial t} + \frac{Gm}{r^2} + 4\pi r^2 \frac{\partial P}{\partial m} = 0 \tag{6.2}$$

$$\frac{\partial E}{\partial t} + P\frac{\partial V}{\partial t} + \frac{\partial L}{\partial m} = 0 \tag{6.3}$$

where

$$V \equiv \frac{1}{\rho} = \frac{4\pi}{3}\frac{\partial r^3}{\partial m} \; . \tag{6.4}$$

In these equations the pressure P and the internal energy per gram E are assumed to be given as functions of the temperature T and the specific volume V by the equations of state:

$$P = P(T,V)$$

$$E = E(T,V) \; .$$

These relations are discussed in Appendix C. In equation (6.3) L is the total heat flux transported outward across a surface of given m. It turns out that in the early stages of the collapse under consideration here, the only important heat transfer process is radiation; convection does not occur. The calculation of L is therefore a problem in radiative transfer, in general quite complicated. If the material is quite optically thick, the calculation of the radiation transfer simplifies greatly and we can use the radiation diffusion equation used in the theory of stellar interiors. This equation may be written as follows:

$$L = -\frac{256\,\pi^2\sigma}{3}\, r^4\, \frac{T^3}{\kappa}\, \frac{\partial T}{\partial m} \tag{6.5}$$

where σ is the Stefan-Boltzmann constant and $\kappa = \kappa(T,V)$ is the Rosseland mean opacity, already discussed in section 2.2. We postpone to section 6.3 a discussion of the radiation transfer problem in cases where the material is not completely optically thick.

We now have 5 differential equations, and if P, E, and κ are specified as functions of T and V we have 5 basic unknowns, which we may for example take to be r, u, V, T, and L. (Note that these are just the 4 variables of stellar structure plus the velocity u.) Correspondingly we require 5 boundary conditions. There are 3 obvious boundary conditions at the center: at $m = 0$, we have $r = u = L = 0$. Two boundary conditions, one mechanical and one thermal, must be specified at the outer boundary $m = M$. The mechanical boundary condition may for example take the form of a specification of either P or u at the boundary, as has already been discussed in section 4. The thermal boundary condition might for example be a specification of T or of a relation between L and T at the boundary; we shall postpone discussion of this, along with further discussion of the radiation transfer problem, until after we have given the Eulerian equations, since the same problem occurs in the Eulerian case.

6.2 The Eulerian Equations

In the Eulerian formulation of the differential equations the flow variables are referred to a coordinate system which is fixed in space and through which the fluid moves. In our spherically symmetric problem the Eulerian space coordinate is r, so that r in this case becomes one of the independent variables along with t. The Eulerian differential equations then give the rate of change of the flow variables and of the mass m on a surface of constant r. Again we write the differential equations in the form most closely related to the difference equations used, and we write the diffusion equation for radiation transfer when the material is optically thick:

$$\frac{\partial m}{\partial t} = -\frac{4\pi r^2 u}{V} \tag{6.6}$$

$$\frac{\partial u}{\partial t} + u\frac{\partial u}{\partial r} + \frac{Gm}{r^2} + V\frac{\partial P}{\partial r} = 0 \tag{6.7}$$

$$\frac{\partial E}{\partial t} + P\frac{\partial V}{\partial t} + u\left(\frac{\partial E}{\partial r} + P\frac{\partial V}{\partial r}\right) + \frac{3}{4\pi}V\frac{\partial L}{\partial r^3} = 0 \tag{6.8}$$

$$\frac{1}{V} - \frac{3}{4\pi}\frac{\partial m}{\partial r^3} = 0 \tag{6.9}$$

$$L = -\frac{64\pi\sigma}{3} r^2 \frac{VT^3}{\kappa}\frac{\partial T}{\partial r} \;. \tag{6.10}$$

In this case the 5 basic dependent variables may be taken as m, u, V, T, and L. Again we require 5 corresponding boundary conditions, of which there are 3 obvious ones at the center: at $r = 0$, $m = u = L = 0$. In the Eulerian case the only simple way to handle the outer boundary conditions is to take the outer boundary to be a fixed surface $r = R$, and specify conditions on this surface. Since by assumption our boundary encloses a fixed mass of material, we must in this case allow no mass flow across the surface $r = R$; i.e. the mechanical outer boundary condition must be taken as $u = 0$ at $r = R$. As has been discussed in section 4, this type of boundary condition was considered to be as reasonable as any other; therefore other possible ways of treating the Eulerian boundary conditions have not been investigated.

6.3 The Treatment of Radiation Transfer

We still have to discuss in more detail the radiation transfer problem. The equations (6.5) or (6.10) are valid only when the material is optically thick at the relevant wavelengths near the peak of the blackbody curve, but this is certainly not always the case. With our adopted opacity data and initial conditions, the optical depth of the whole protostar is initially $<< 1$ at the relevant far infrared wavelengths, and it does not approach unity until the central density has risen several orders of magnitude above its initial value. Even then only a very small central region of high density becomes optically thick, while most of the cloud remains optically thin.

The thermal conditions in the optically thin material during the early stages of the collapse come under the discussion in section 3, where it was shown that a reasonably good approximation would be obtained by assuming the optically thin material to remain isothermal at 10 ^{o}K. It happens that when the diffusion equation (6.5) or (6.10) is applied in an optically thin region, where it is physically completely invalid, it has the effect of artificially making the whole optically thin region very nearly isothermal at whatever temperature is specified as the boundary temperature. Thus if we apply the diffusion equation throughout, even when the material is optically thin, and specifiy $T = 10\ ^{o}K$ as the thermal boundary condition, the temperature during the optically thin stages of the collapse is artificially kept very nearly isothermal at 10 °K, as desired. In the opaque core which eventually forms at the center, on the other hand, the diffusion equation correctly describes the radiation transfer, and the temperature is correctly calculated.

Thus it happens rather fortunately that we can use equations (6.1) - (6.5) or (6.6) - (6.10) as they stand throughout the calculations and obtain results which are correct in the limit of large optical depths and a reasonably good approximation for small optical depths. This is the procedure which has been used in all of the present calculations. This procedure is not so clearly justified in the intermediate case where neither the optically thick nor the optically thin limits apply, but one can show by approximate arguments that the diffusion equation still gives approximately the correct temperature even in this transition case. The adopted procedure is therefore believed to provide a satisfactory approximation for the present purposes, particularly in view of the fact that the dust opacity is quite uncertain anyway.

This fortunate situation holds only during the early stages of the collapse. Later on the luminosity generated by the collapse in the central part of the cloud becomes an important source of heating for the outer optically thin regions; this is not properly accounted for by the diffusion equation, which gives a temperature which is too low under these circumstances. In the early stages of the collapse under consideration here, this error begins to appear but does not yet become serious, so we need not worry about it here. Further discussion of this problem will be given in section 8.3 in connection with the later stages of the collapse.

7. RESULTS FOR THE EARLY STAGES OF THE COLLAPSE

7.1 Explanation of the Calculations

The numerical methods which have been used for computing the early stages of the collapse are described in detail in Appendix A. Both Lagrangian and Eulerian computational schemes have been developed, and each was used where most advantageous, as explained in Appendix A. In both cases shock fronts have been treated by the von Neumann-Richtmyer pseudoviscosity method which artificially spreads a shock transition out over several mass zones, thus allowing shock fronts to be handled automatically wherever they arise in the flow without the need for a special treatment.

Since the present project has represented an exploratory venture whose outcome would not necessarily bear any relation to anything in the real world, let alone anything observable or measurable, it was mainly the qualitative features of the results which were of interest, and not so much the quantitative details. In any case, we have seen in the preceding sections that there are so many uncertainties in the various assumptions and input data that probably only the general qualitative features of the collapse can be calculated with any confidence anyway. Therefore high numerical accuracy has not been sought in this project, and the numerical calculations have been made with space and time grids which are quite coarse compared with what might usually be considered adequate. A general level of accuracy of the order of 20% or so appeared for the most part to be a reasonable goal, being quite adequate for the present purposes but still usually attainable without requiring large amounts of computing time. The accuracy actually achieved in the results is discussed in section A.7; various checks described there verify that accuracies of the order of 20% or so in the important quantities were in fact usually attained.

In this project numerical collapse calculations have been made using a variety of different assumptions and choices of parameters in an effort to find out how the results would be affected by uncertainties or variations in these assumed conditions. Of the various sets of assumptions considered, seven cases covering a fairly wide range in parameters were selected for reasonably complete and systematic calculations extending all the way through to a star approaching the main sequence. These seven cases will be described in detail below. Other calculations were made for the initial stages of the collapse using different assumptions, but in general these other calculations were not systematic or complete enough, nor were the results different enough to merit a separate description in detail. Usually the outcome of these other calculations was that some particular change in assumptions was found to make no basic qualitative difference in the results; since it was mainly the qualitative features of the results which were of interest, it was not considered worthwhile to pursue these calculations further. Their results, as far as they go, will be (or have been) summarized in some general assertions about the effect of varying certain assumptions; for example, it was mentioned in section 5 that different initial velocity distributions do not appear to affect the nature of the collapse very much, once the collapse is well under way.

The 7 cases to be described are listed in Table 2 (p. 41), which shows the conditions assumed in each case. In all cases the calculations were started with a uniform initial density and zero initial velocity, as discussed in section 5. In all cases except no. 6 the boundary has been assumed to be fixed in space, as was discussed in section 4. In each case the temperature listed under "$T_{\text{init.}}$" is the value which has been specified as the boundary temperature in the procedure described in section 6.3, and it represents not only the initial temperature but the temperature during the whole isothermal phase of the collapse. We explain the individual cases in more detail below.

Case 1 is the "standard case" for one solar mass, calculated with what are thought to be the best values of all parameters, according to the discussion in Part I.

Case 2 has an initial temperature chosen to be one order of magnitude higher than in Case 1 to allow for the possibility of a serious error in the estimated initial temperature. The initial density must then be 3 orders of magnitude higher than in Case 1 to ensure gravitational collapse.

Case 3 has the same initial temperature as Case 1 but an initial density 3 orders of magnitude higher, as in Case 2. This choice was made because it was desired to find the effect of increasing the density alone, without changing the temperature. (The initial density derived in section 5 and used in Case 1 is after all only a minimum, and the actual initial density could conceivably be considerably higher.)

TABLE 2

DEFINING PROPERTIES OF THE CASES CALCULATED

Case No.	$M/M_\odot$	$T_{init.}$ (^oK)	$\rho_{init.}$ (gm/cm^3)	$R_{init.}$ (cm)	κ_{dust} (cm^2/gm)	H_2 ?	boundary cond.
1	1	10	1.1×10^{-19}	1.63×10^{17}	0.15	yes	$u = 0$
2	1	100	1.1×10^{-16}	1.63×10^{16}	0.15	yes	$u = 0$
3	1	10	1.1×10^{-16}	1.63×10^{16}	0.15	yes	$u = 0$
4	1	10	1.1×10^{-19}	1.63×10^{17}	0.0015	yes	$u = 0$
5	1	10	6.4×10^{-19}	9.06×10^{16}	0.15	no	$u = 0$
6	2	10	2.5×10^{-19}	1.56×10^{17}	0.15	yes	$P = const.$
7	5	100	4.4×10^{-18}	8.15×10^{16}	0.15	yes	$u = 0$

Case 4 has an assumed dust opacity reduced by two orders of magnitude from Case 1 in order to find the effect of a large error in the dust opacity, which is very uncertain as was seen in section 2.2. It was hoped also to get an idea of how star formation might differ in a region with greatly reduced dust content, as might be appropriate for example for the formation of Population II stars.

Case 5 was calculated assuming no H_2 molecules to exist at any time during the collapse. This case may have no relation to reality, even if molecules are not present initially, because as long as molecules form before the material becomes optically thick at about 10^{-13} gm/cm^3, the collapse will proceed essentially as in Case 1; still, this case provides another test of the sensitivity of the final result to large changes in the conditions during the early stages of the collapse.

Case 6, with $M = 2M_{\odot}$, was actually the first one calculated, and was done before the more systematic procedure used in the other cases had been adopted. Thus it was calculated with the Lagrangian method and the constant boundary pressure assumption, rather than the Eulerian method and the fixed boundary assumption as in the other cases. Also, the initial density was determined using the virial theorem with no external pressure, and is about a factor 10 higher than is required to ensure collapse. Nevertheless, it was thought that this early calculation was still of sufficient interest to merit inclusion.

Case 7, with $M = 5M_{\odot}$, was calculated in order to find the effect of an increase in mass, and it was desired to be able to compare the results with one of the cases already calculated for one solar mass. If a temperature of 10 °K had been chosen and the initial density calculated as in Case 1, this density would have been 4.4×10^{-21} gm/cm^3; at this low density, however, the temperature would in reality be much higher than 10 °K, necessitating in turn a much higher starting density. In order that there might be some comparison with one of the cases already calculated, a temperature of 100 °K was chosen, as in Case 2, and the corresponding minimum initial density was taken. It is not argued that this choice of parameters is necessarily realistic.

The results for the early stages of the collapse in each of these cases will be described in detail in the following subsections. As it turns out, the qualitative features of the collapse are much the same in nearly all of the cases tried, including those not listed in Table 2; even the quantitative numerical results are not very different, considering the large differences in assumed parameters. Thus it will be possible to a large extent, at least for qualitative purposes, to include all of the cases under common descriptions. We begin by describing the initial optically thin isothermal stages of the collapse.

7.2 Isothermal Stages of the Collapse

At the initial instant, the temperature and density and therefore also the pressure are by assumption uniform throughout the cloud. Consequently there are no pressure gradients, and the whole cloud begins to collapse in free fall. The density and pressure in the interior of the cloud then rise, whereas the pressure at the surface may decrease or remain constant, depending on the assumed boundary conditions, but it at least does not increase. A pressure gradient therefore arises near the surface of the cloud, causing the collapse near the surface to be significantly retarded from a free fall. As the collapse proceeds, this pressure gradient and the consequent retardation of the collapse propagate inward in the cloud; what we have, in fact, is just an expansion wave which starts at the surface of the cloud as soon as it begins to collapse and then travels inward at the speed of sound relative to the infalling material. Since the central part of the cloud continues to collapse rapidly whereas the collapse of the outer parts is progressively retarded, the density rises faster at the center than in the outer parts of the cloud, and the density distribution soon becomes strongly peaked at the center.

If the initial density is near the minimum value required for gravitational collapse, the expansion wave reaches the center before the collapse has gotten very far, and the collapse at the center is strongly decelerated. If the initial density is too low, in fact, the material at the center stops collapsing and rebounds. With a higher initial density the expansion wave does not reach the center until a later stage in the collapse, and the deceleration is insufficient to halt the collapse completely. In this case gravitational forces eventually regain dominance over pressure forces, and the collapse is again accelerated. Thereafter the collapse continues approximately as a free fall. Since the free fall collapse time depends inversely on the density, the collapse proceeds most rapidly at the center where the density is highest; consequently the density distribution becomes more and more sharply peaked at the center. A situation is soon reached in which the density at the center is orders of magnitude higher than the density in the outer parts of the cloud, and the time scale for collapse at the center is correspondingly orders of magnitude shorter than the time scale for collapse of the outer parts of the cloud.

The development of the central density peak is illustrated for Case 1 in Fig. 2 (p. 46); the results in all other cases are quite similar. The diagram shows log ρ plotted vs. log r at several times during the isothermal phase of the collapse. At the latest time shown the central density is 7 orders of magnitude higher than the density at the surface, and the central density peak has a width only about 10^{-3} times the total radius; the mass in this central dense region is also only about 10^{-3} times the total mass. It is clear in Fig. 2 that as the collapse proceeds, large increases in density occur on a short time scale at the center while practically nothing happens in the outer parts of the cloud where most of the mass still resides.

This extremely non-homologous character of the collapse, with the consequent great disparity in time scales between the central and outer parts of the cloud, was found in all of the cases tried. Furthermore, the same kind of result was obtained by Penston (1966), who used different initial conditions. Thus it appears that this is a universal property of isothermal spherical collapse problems of this type. The extent of the deviation from homologous collapse and its full importance for star formation have apparently not been previously

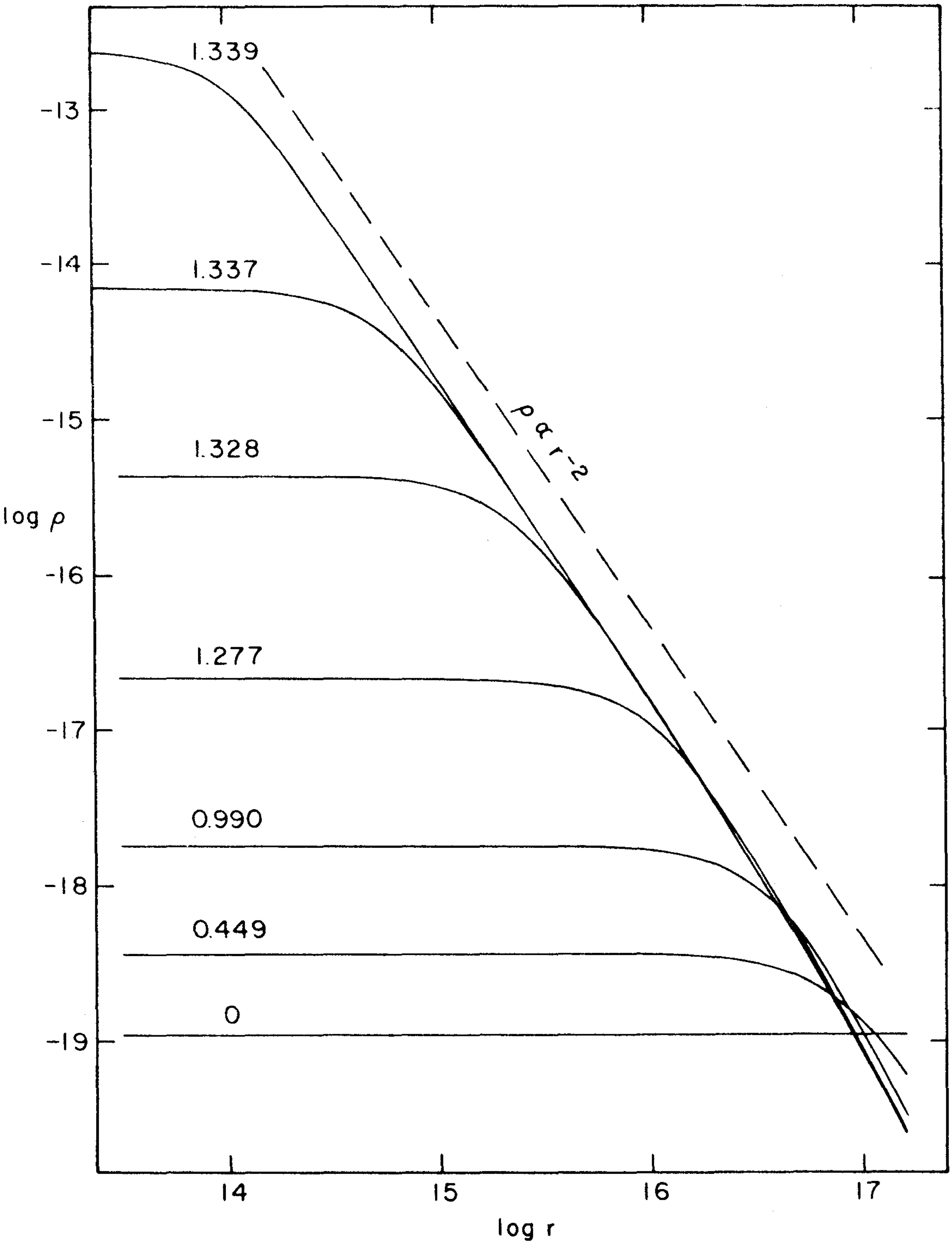
1.339
1.337
1.328
1.277
0.990
0.449
0
$\rho \propto r^{-2}$
log ρ
-13
-14
-15
-16
-17
-18
-19
14
15
16
17
log r

FIGURE 2

Fig. 2 (p. 46): The evolution of the density distribution in the collapsing cloud for Case 1. The unit for r is cm and the unit for ρ is gm/cm^3. The curves are labeled with the times in units of 10^{13} seconds since the beginning of the collapse. The time scale in the Eulerian calculations is somewhat inaccurate, as explained in Appendix A, so the time scale indicated by these numbers is different from the corrected time scale given in Table 5 (p. 63).

realized; consequently, as will be seen, some of the results of Gaustad (1963), Hayashi and Nakano (1965), and Hayashi (1966), which were obtained assuming homologous collapse or polytropic density distributions, are invalidated.

An important aspect of the collapse is that although gravitation is dominant over pressure forces, making the collapse proceed approximately as a free fall, the pressure forces are never completely negligible (except initially), and they play an essential role in determining the density distribution. In Case 1, for example, the outward pressure gradient force is typically somewhat more than half of the inward gravitational force, and this ratio remains nearly constant as the collapse proceeds. Thus the collapse, while qualitatively like a free fall, is significantly retarded from the free fall collapse rate.

It may be noted that at the later times shown in Fig. 2, the curves of log ρ vs. log r in the inner part of the cloud are at different times very nearly identical except for scale shifts. This fact, together with the fact that the ratio of pressure to gravity forces at corresponding points remains nearly constant as the collapse proceeds, suggests that the flow variables in the inner part of the cloud may at different times be represented by functions of r having the same form, differing only by scale factors which vary as a function of time. In the calculations this is found to be nearly the case, becoming a better and better approximation the longer the collapse proceeds (as long as the material remains isothermal). It can be shown mathematically that such invariant functional forms are in fact a possible solution of the equations in the limit where the outer boundary can be considered as infinitely far away; some of the mathematical analysis is given in Appendix D. The actual solution always approaches this limiting "similarity solution" near the center if the collapse proceeds far enough.

One of the results derived in Appendix D is that the density distribution in the rapidly collapsing region should approach the form $\rho \propto r^{-2}$. We see in Fig. 2 that in Case 1 the density distribution does indeed closely approach an r^{-2} law; the same kind of result is found in all the other cases tried.

7.3 Formation of the Opaque Core

When the central density reaches a value in the neighborhood of 10^{-13} gm/cm^3 (plus or minus about one order of magnitude), the infrared optical depth of the dense central region becomes greater than unity; the thermal energy generated by the collapse is then no longer freely radiated away, and the central temperature begins to rise above its initial value. (Optical depths have been calculated using the dust opacity of 0.15 cm^2/gm adopted in section 2.2; this value is of course highly uncertain.) As the collapse proceeds, the optical depth of the central region increases, while the collapse time scale decreases; as a result of these two effects, the energy transported by radiation during the collapse time scale soon becomes negligible in comparison with the internal energy of the material, and the collapse at the center becomes very nearly adiabatic. The central temperature then rises rapidly, and the pressure soon becomes sufficient to decelerate and eventually even stop the collapse at the center. In Case 1, for example, the collapse at the center begins to decelerate at a central density of about 10^{-12} gm/cm^3, and it has practically stopped by the time the central density reaches about 10^{-10} gm/cm^3 and the central temperature a value somewhat over 100 °K.

All of the above statements apply only to a very small region at the center of the collapsing cloud, having a mass of the order of only 10^{-2} solar masses and a radius of only a few astronomical units, or about 10^{-3} times the total radius; the material outside this region, i.e. nearly all of the mass of the cloud, remains optically thin and nearly isothermal, and it continues to collapse inward almost in free fall. Between the central region of decelerating collapse and the surrounding region of continuing near free fall collapse, there consequently arises a steep velocity gradient, which rapidly steepens into a shock front. By the time the collapse has stopped at the center this shock front is well developed, the velocity of infall being reduced almost to zero inside the shock front. The situation which then exists is that we have a central "core" in which the material has practically stopped collapsing and is approaching hydrostatic equilibrium; bounding this core is a shock front, in which the rapidly infalling material outside the core is suddenly stopped. As the collapse proceeds, this core grows steadily in mass as more material falls into it.

When the collapse at the center is first brought to a halt, the pressure forces are more than sufficient to balance gravity, with the result that the material at the center rebounds and starts expanding again. This sets up radial oscillatory motions in the core, which continue for a considerable time, superimposed on a slow contraction as the core accumulates more material. The rebound and the ensuing radial oscillations were found in the calculations to have amplitudes of the order of 10 to 20% in radius, although these motions were not accurately calculated. The basic phenomenon is just adiabatic pulsations about a hydrostatic equilibrium configuration, but the motion is in fact quite complicated, since many modes are excited. Calculating these pulsations in any detail would require finer space and time grids and hence more computing time than would otherwise be desirable, and since these pulsations are not particularly of interest anyway for the present purposes, we have favored numerical methods which tend to suppress such motions, as explained in Appendix A. In fact with the Eulerian method used in most of these calculations the rebound and radial pulsations are suppressed almost completely out of existence.

Some properties of the core at a time soon after its formation are listed in Table 3 (p. 52); this table gives the initial mass, radius, central density, and central temperature of the core for each of the seven cases. The quantities in this table are intended to refer approximately to the time of the first rebound at the center. In most cases, however, since the rebound is suppressed by the numerical method, this instant is difficult to define and has necessarily been chosen somewhat arbitrarily. Because of this arbitrariness and because of other uncertainties, the numbers in the table have not much more than an order of magnitude significance.

TABLE 3

INITIAL PROPERTIES OF THE FIRST CORE

Case No.	M (gm)	R (cm)	ρ_c (gm/cm^3)	T_c (^oK)
1	1.0×10^{31}	6×10^{13}	2×10^{-10}	1.7×10^{2}
2	5×10^{31}	4×10^{13}	3×10^{-9}	1.4×10^{3}
3	1.3×10^{31}	6×10^{13}	3×10^{-10}	2.3×10^{2}
4	2×10^{30}	1.3×10^{13}	4×10^{-9}	1.7×10^{2}
5	4×10^{31}	1.5×10^{14}	4×10^{-11}	1.8×10^{2}
6	1.6×10^{31}	6×10^{13}	2×10^{-10}	2.8×10^{2}
7	5×10^{31}	4×10^{13}	3×10^{-9}	1.4×10^{3}

In Table 3 note first of all that the quantities listed for the various cases do not vary greatly, at least in order of magnitude, despite large differences in the assumptions; in no case do they differ by more than about one order of magnitude from our "standard" Case 1. Thus it appears that the results so far are not too strongly sensitive to the considerable uncertainties in the assumed conditions. Note that the results are closely similar in Cases 1 and 3, which were calculated with the same temperature and opacity but with initial densities differing by 3 orders of magnitude. The results are even more nearly identical in Cases 2 and 7, which differ in mass as well as in initial density. The reason for this similarity is that after the collapse has proceeded through a few orders of magnitude in density, the solutions in both cases approach the same "similarity solution" near the center, as discussed in the previous subsection and in Appendix D. Since the opacity is the same in the two cases, the solutions remain nearly the same during the formation and growth of the opaque core.

7.4 Growth and Central Collapse of the Core

As the infall continues and the core grows in mass, the material near the center of the core is compressed adiabatically (since radiation transfer is negligible), and the central temperature and density rise together following the isentropic relation $T \propto \rho^{\gamma-1}$. The radius of the core actually decreases somewhat as it grows in mass; thus the shock front moves inward in radius, although it moves outward in mass. Part of the reason for the contraction of the core is that although radiation transfer is negligible in the dense central part of the core, the density near the surface is low enough for radiation transfer and radiative cooling to be important in the outer part of the core. In fact, most of the thermal energy generated in the shock front from the conversion of kinetic energy to thermal energy is immediately radiated away again just inside the shock front.

After the mass of the core has increased by a moderate factor (typically about 2 or 3) and the radius has decreased by a similar factor, the central temperature has risen substantially to a value of about 2000 °K, at which point hydrogen molecules at the center of the core begin to dissociate. Dissociation of H_2 molecules reduces the ratio of specific heats γ below the critical value 4/3; the central pressure then no longer rises sufficiently rapidly with increasing density to maintain hydrostatic equilibrium, and the material at the center becomes unstable and begins to collapse gravitationally. As the material collapses, most of the internal energy generated by the compression goes into molecular dissociation and not into the thermal motion of the particles; consequently, even though the collapse is adiabatic, the central temperature rises only slowly with increasing density. Therefore the material at the center of the core approaches a state of near free fall, which is quite similar in many respects to the earlier isothermal collapse of the whole cloud, as described previously in section 7.2.

In this second dynamical collapse phase, as in the first, the density distribution in the collapsing region becomes more and more sharply peaked at the center, and the time scale for collapse at the center becomes shorter and shorter with increasing central density. In this case the collapse is not isothermal, so the similarity considerations of Appendix D do not apply; nevertheless, the density distribution in the collapsing region approaches a form quite similar to that in the isothermal case. In this case the density distribution approaches approximately the form $\rho \propto r^{-2.4}$, compared with $\rho \propto r^{-2}$ in the isothermal case.

When the material at the center of the core collapses, its pressure is no longer sufficient to support the outer parts of the core in hydrostatic equilibrium, and these outer parts also begin to collapse. However since the density at the center of the core at the time the collapse begins is typically at least 2 or 3 orders of magnitude higher than the density near the surface of the core, the time scale for collapse is much shorter at the center of the core than near the surface. Consequently the conditions in the outer part of the core and the properties of the shock front change very little over the whole time scale of the collapse at the center. Farther out in the protostellar cloud, of course, the time scale is even longer, and the changes are completely negligible during the whole phase of central collapse of the core.

The descriptions of the results in this section obviously do not apply to Case 5, in which hydrogen molecules were assumed never to exist. In order to preserve continuity, we shall postpone the description of the results in Case 5 to section 7.6.

7.5 Formation of the Final Stellar Core

The central collapse of the core continues through several orders of magnitude in density, following the isentropic temperature-density relation, until the hydrogen molecules are nearly all dissociated at the center and γ is again greater than 4/3. The central pressure then rises sufficiently to decelerate the collapse, and the collapse at the center finally stops at a central density of the order of 10^{-2} gm/cm^3 and a central temperature of about 2×10^4 °K. At this point the hydrogen is nearly all in atomic form; only a few per cent remains in molecular form. Despite the temperature, the degree of ionization is still small, amounting to only a few per cent; this is because of the high density of about 10^{-2} gm/cm^3, which is much higher than is normally encountered in association with a temperature of 2×10^4 °K in stars. Also because of the high density, the degree of ionization increases only slowly with increasing temperature, the rate of increase being insufficient to reduce γ below 4/3. Thus the material is stable against further gravitational collapse.

When the collapse at the center is stopped for the second time, the resulting dynamical phenomena are very similar to those which occurred the first time the collapse was halted at the center after the initial isothermal collapse phase. A shock front arises, in which the infalling material is suddenly stopped and its kinetic energy is converted into thermal energy. Inside the shock front a second core develops, in which the material has stopped collapsing and is approaching hydrostatic equilibrium. After it has stopped collapsing, the material at the center of this second core rebounds, and the core is set into a series of complicated adiabatic pulsations which continue for a considerable time after the formation of the core. Again it has been found desirable to use numerical techniques which tend to damp out these motions, and in the Eulerian method usually used the rebound and the ensuing oscillations are strongly damped.

When the second core and shock front form, the outer parts of the first core and its bounding shock front have hardly changed. Thus at this stage we have two concentric shock fronts. The density and velocity distributions at a time soon after the formation of the second core are illustrated for Case 1 in Fig. 3 (p. 58). The corresponding diagrams for all the other cases (except Case 5) are qualitatively quite similar in appearance. The artificial viscosity method which has been used for calculating shock fronts spreads each shock front out over 2 or 3 adjacent grid points (see Appendix A), so that shock fronts appear not as discontinuities but as regions of smooth but rapid variation of the velocity and density with r. The shock transitions have been plotted just as calculated, without attempting to reconstruct the discontinuity to which the smooth transition is an approximation. Thus for example in Fig. 3 the shock fronts appear most conspicuously as regions of steep positive slope in the velocity curve, where the velocity decreases rapidly moving inward.

The initial properties of the inner core are listed for the various cases in Table 4 (p. 60), which also gives the mass and radius for the outer shock front at this time. Again the tabulated numbers are intended to refer approximately to the time of the first

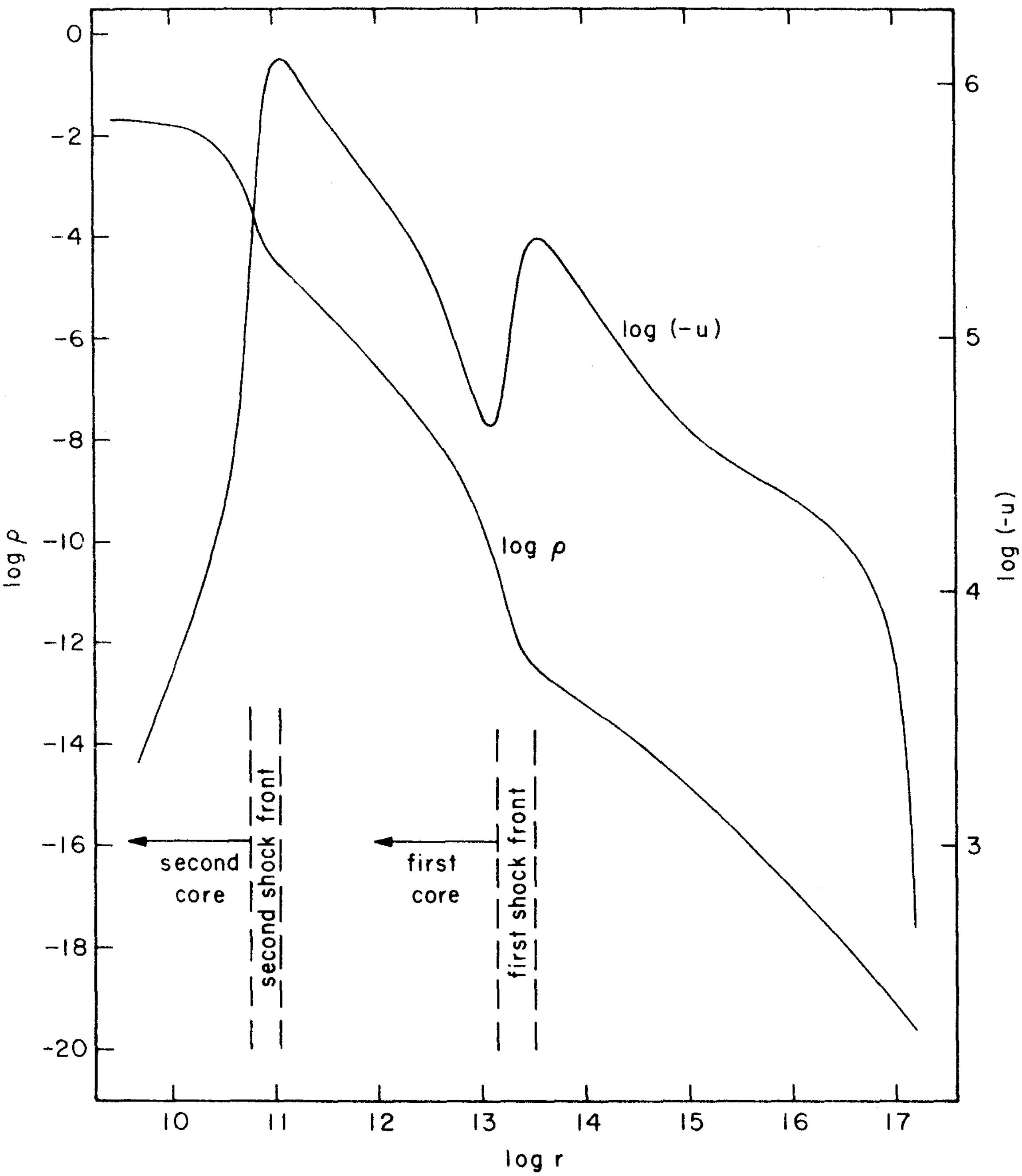
0
-2
-4
-6
-8
-10
-12
-14
-16
-18
-20
log ρ
6
5
4
3
log (-u)
log (-u)
log ρ
second core
second shock front
first core
first shock front
10
11
12
13
14
15
16
17
log r

FIGURE 3

Fig. 3 (p. 58): The density and velocity distributions in Case 1 at a time shortly after the formation of the second core. All quantities are in CGS units. The shock fronts are represented by the regions of steep positive slope in the velocity curve.

TABLE 4

INITIAL PROPERTIES OF THE SECOND (STELLAR) CORE

Case No.	M_{outer} shock (gm)	R_{outer} shock (cm)	$M_{stellar}$ core (gm)	$R_{stellar}$ core (cm)	ρ_c (gm/cm^3)	T_c (^oK)
1	2×10^{31}	2×10^{13}	3×10^{30}	9×10^{10}	2×10^{-2}	2.2×10^4
2	7×10^{31}	4×10^{13}	6×10^{30}	1.5×10^{11}	9×10^{-3}	2.3×10^4
3	3×10^{31}	3×10^{13}	4×10^{30}	1.0×10^{11}	1.7×10^{-2}	2.2×10^4
4	5×10^{30}	5×10^{12}	1.5×10^{30}	4×10^{10}	9×10^{-2}	2.2×10^4
5	1.5×10^{32}	1.2×10^{15}	6×10^{31}	5×10^{11}	3×10^{-3}	6×10^4
6	4×10^{31}	3×10^{13}	4×10^{30}	1.4×10^{11}	2×10^{-3}	1.9×10^4
7	7×10^{31}	4×10^{13}	5×10^{30}	1.4×10^{11}	9×10^{-3}	2.3×10^4

rebound at the center, but this instant is not very well defined in the calculations because the rebound is partially suppressed. Thus the numbers are again subject to some uncertainty, although the uncertainty may be less in this case than it was with the first core.

We notice in Table 4 that (excluding Case 5) the initial properties of the second core vary remarkably little from case to case--even less than the initial properties of the first core. The initial mass and radius, for example, in no case differ from the "standard" Case 1 by more than a factor of 2. The initial mass of the second core is about one tenth the mass of the first core, or roughly 10^{-3} solar masses in order of magnitude. The radius is typically about one half of one per cent of the radius of the first core, or roughly one solar radius in order of magnitude. Again the near identity of the results in Cases 1 and 3 and in Cases 2 and 7 is evident.

It is interesting to note that the surface properties of this second core are much like those of an ordinary star. Thus in addition to a radius of slightly over one solar radius, the core has an initial surface temperature (inside the shock front) of about 10^4 ^oK. If the core were plotted on an HR diagram on the basis of its radius and surface temperature, it would fall near the main sequence position of a star of surface temperature 10^4 ^oK. It also of course emits the same luminosity as such a star, but this radiation is immediately reabsorbed in the very optically thick infalling material just outside the shock front and thus never escapes from the immediate vicinity of the shock front. The luminosity leaving the protostellar cloud at this stage is considerably smaller, being only of the order of one solar luminosity or less, and it is not of much interest from an observational point of view because of the very short associated time scale (less than 100 years).

The total time elapsed during the early stages of the collapse, i.e. from the beginning of the collapse to the formation of the second core, is listed for each case in Table 5 (p. 63). This table also shows for comparison the free fall time of the cloud, calculated from the formula

$$t_{ff} = \left(\frac{3\pi}{32\, G\rho_{init.}} \right)^{\frac{1}{2}} \tag{7.1}$$

We see from Table 5 that in Cases 3 and 6 the actual collapse time is essentially equal to the free fall time, and in the other cases it is about $1\frac{1}{2}$ times larger than the free fall time. The extra time in these other cases is taken up near the beginning of the collapse, when the collapse is significantly retarded from a free fall.

As the collapse proceeds, material falls away from inside the outer shock front, and it gradually dies out. We are then left with a single central core of approximately stellar dimensions, which continues to grow in mass as the rest of the protostellar cloud falls into it. The core undergoes no further dynamical collapse, and the accretion continues until all of the protostellar material has fallen into the core; at this point the core becomes a more or less ordinary pre-main sequence star. The later stages of this accretion process involve different physical processes and require different numerical methods from those used for the early stages of the collapse, and we shall therefore postpone further description of the

TABLE 5

TIME REQUIRED FOR THE EARLY STAGES OF THE COLLAPSE

Case No.	t_{ff} (yrs)	t_{actual} (yrs)
1	2.0×10^5	3×10^5
2	6.3×10^3	9×10^3
3	6.3×10^3	6×10^3
4	2.0×10^5	3×10^5
5	8.3×10^4	1.2×10^5
6	1.3×10^5	1.3×10^5
7	3.2×10^4	5×10^4

results for the later stages of the collapse until section 9, after we have discussed in section 8 the relevant physics and the special assumptions and approximations which we have used.

7.6 Results in Case 5 (No Molecular Hydrogen)

In Case 5 the initial isothermal collapse phase and the formation of the first core proceed much as in the other cases. The main difference is that since γ and the gas constant $\Re$ are larger for atomic than for molecular hydrogen, the pressure rises more rapidly with increasing density once the core starts to become opaque, and the collapse is halted at a lower density (see Table 3, p. 52). After its formation, the core grows in mass and decreases in radius as in the other cases. Because of the lower density, however, radiative cooling is more important than in the other cases.

In this case there is of course no molecular dissociation and no corresponding dynamical collapse at the center. However another phenomenon becomes important in about the same temperature range. According to our assumptions in section 2.2, the dust grains evaporate at a temperature of 1400 $^{\circ}$K and the opacity then decreases rapidly with increasing temperature. In Case 5 the core density is low enough that when the central temperature rises above 1400 $^{\circ}$K and the opacity accordingly drops, radiative cooling of the central part of the core becomes important on a time scale comparable to or less than the time scale for accretion of material by the core. Thus the central part of the core radiates strongly, cools, and contracts. (It may be noted that despite the large decrease in opacity, the material remains optically thick at all times, so that the radiation diffusion equation remains applicable.) At the same time, radiation emitted from the central part of the core is absorbed in the outer part of the core where the opacity is still large; consequently the outer part of the core heats up and expands. As a result the shock front is in this case driven outward in radius. These motions occur on a time scale somewhat shorter than the time scale for accretion of material by the core, so that the core mass changes little while they are taking place.

Eventually, as the inner part of the core contracts and the outer part expands, the density near the boundary of the inner contracting region becomes so low that the velocity required to maintain the mass inflow begins to approach the free fall velocity. A shock front then develops between the slowly contracting central region and the more rapidly collapsing surrounding region. Thus there again appears a central core in hydrostatic equilibrium, bounded by a shock front outside which the material is falling inward almost in free fall. This second core is fairly well established by the time the central density reaches about 10^{-6} gm/cm^3 and the central temperature about 10^4 °K. By this time radiative cooling at the center has again become negligible, so that the further evolution of the second core is adiabatic.

When the central temperature reaches a value somewhat over 10^4 °K, hydrogen ionization reduces γ below 4/3 at the center, thereby causing a dynamical collapse at the center of the core, similar to what happened in the other cases due to H_2 dissociation.

In this case however the instability is shorter lived and the central collapse is stopped after an increase of only about 3 orders of magnitude in density. Once again when the collapse stops a central core and bounding shock front form. Since this is the third shock front to form and the other two are still in existence, there are at this point three shock fronts existing simultaneously. The initial properties of the final (third) core are listed in Table 4. At this time the second shock front is at a mass of about 7×10^{31} gm and a radius of about 4×10^{12} cm.

8. EQUATIONS AND APPROXIMATIONS FOR THE LATER STAGES OF THE COLLAPSE

As is explained in Appendix B, the time step limitation for the Lagrangian method becomes so severe during the later stages of the collapse that the use of the Lagrangian method becomes totally impracticable. It is therefore essential to use the Eulerian method or some modified form thereof. The Eulerian differential equations have already been given and discussed in section 6 (equations 6.6 - 6.10). These equations are of course applicable also during the later stages of the collapse, except for equation (6.10) which we shall discuss separately in section 8.3. The main modifications required in calculating the later stages of the collapse are a special treatment of the shock front and the inclusion of convective energy transport in the stellar core. We shall discuss these modifications in some detail in the following subsections.

8.1 The Shock Front

During the later stages of the collapse the pseudoviscosity method becomes no longer satisfactory for treating the strong shock front bounding the stellar core. For one thing, the pseudoviscosity method eventually encounters serious numerical difficulties, as is discussed in Appendix B. Also, we would like to obtain a reasonably accurate representation of the structure of the outer layers of the stellar core, and for this purpose the pseudoviscosity technique seems unacceptably crude. This is particularly true toward the end of the collapse, when the stellar core becomes essentially an ordinary pre-main sequence star and the shock front bounding it becomes essentially an ordinary stellar atmosphere. In a pre-main sequence star the properties of the atmosphere are of considerable importance, and some improvement on the pseudoviscosity treatment is clearly necessary in order to adequately represent its structure.

For these reasons it was decided to switch to a "shock fitting" technique for handling the shock front, treating the shock front as an actual discontinuity or step function in the flow variables. In this method limiting values of all quantities are defined on both sides of the discontinuity, and a set of equations known as the shock jump relations are derived relating the values of the variables on both sides of the shock front. In the present case radiative energy transport is of essential importance in the shock front (which is actually a combination shock front and stellar atmosphere), and the usual adiabatic shock jump relations cannot be used. The treatment of the shock front therefore requires some special discussion.

Let us consider first the various physical processes going on in the vicinity of the shock front. First of all we have the mechanical shock jump itself, at which kinetic energy is suddenly converted into thermal energy and there is a discontinuous jump in the temperature and density. Following the shock jump there is a region of relaxation of the internal degrees of freedom; for our purposes this region is of negligible thickness, and it may be considered as part of the shock jump. The hot material inside the shock jump radiates strongly and cools as it moves inward; thus the temperature has a peak value just at the shock jump and falls off rapidly moving inward. The temperature decrease extends inward to an optical depth of order unity, a distance which is always small compared with the radius of the core; beyond this point radiative cooling is no longer important and the temperature and other variables level off and approach constant values.

The radiation emitted from inside the shock jump is partially absorbed in the infalling material just outside the shock front. Consequently the infalling material is heated up, and some of the energy lost by radiation is carried back into the shock front in the form of the thermal energy. Initially, in fact, the radiation emitted from the shock front is totally absorbed within a very short distance outside the shock front, so that the shock front is effectively adiabatic. The form of the temperature distribution in the vicinity of the shock front is sketched in Fig. 4 (p. 70), which shows schematically the effects which we have described.

In general there will also be radiative energy inflow to the shock front, both from the interior of the core and from the infalling material outside the shock front. As it turns out, radiation emitted from the infalling material and travelling inward across the shock front is never of major importance. Radiative energy outflow from the core is initially also unimportant, but toward the end of the collapse when the accretion rate becomes negligible, energy outflow from the interior of the core (which may be partially carried by convection) becomes the dominant energy input to the surface layers

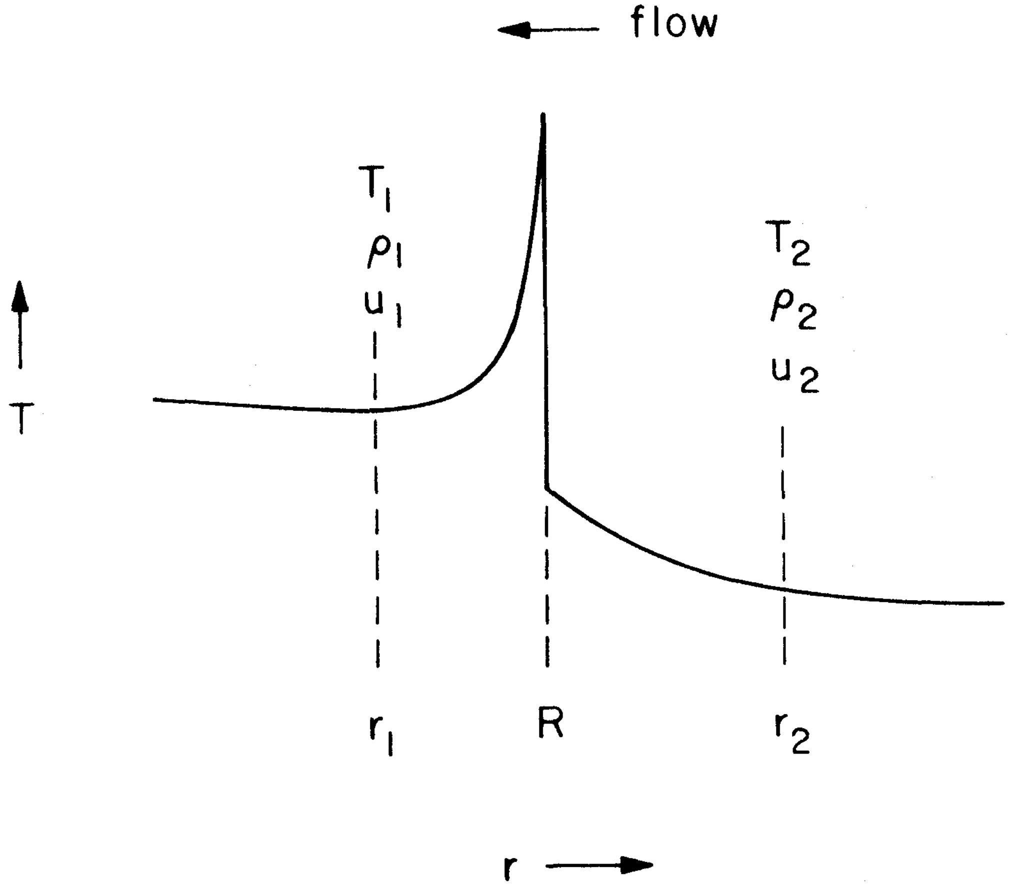

Fig. 4: A schematic illustration of the temperature distribution in the immediate vicinity of the shock jump, which occurs at $r = R$.

of the core. This energy is radiated away into space from the region just inside the shock jump, which thus becomes essentially a stellar atmosphere. Thus it is necessary in treating the shock front to include some of the physics of a stellar atmosphere, at least in some crude approximation.

For the present purposes the fine structure of the temperature distribution and the details of the radiation field in the immediate vicinity of the shock front are not particularly of interest. All that we require for the collapse calculations is a set of relations analogous to the ordinary shock jump equations, relating the values of the variables at some suitable point inside the shock jump to their values at another point outside the shock front. These two points should preferably lie outside the region in which the variables change most rapidly; this relieves the numerical method of the necessity of handling these rapid variations, which usually take place on a scale small compared with any reasonable grid spacing. Thus for example the point inside the shock jump should be at a sufficient optical depth that radiative energy losses are no longer important and the temperature and other variables have nearly reached their limiting values inside the shock jump. Two such suitable points are illustrated in Fig. 4, where values of the variables at the point inside the shock jump are denoted by a subscript 1 and values at the point outside the shock jump are denoted with a subscript 2.

We wish to derive a set of equations analogous to the 3 ordinary shock jump relations expressing the conservation of mass, energy, and momentum across the shock front. We assume that the thickness $r_2 - r_1$ of the shock region is much less than the radius R of the shock jump; we can then neglect the curvature of the shock front and treat it as plane. The shock jump relations are usually derived in a frame of reference which moves with the shock front, so that steady flow may be assumed. In the present case the motion of the shock front is so slow relative to the infall velocity that we can to good accuracy forget about the distinction between a fixed frame and one moving with the shock front and simply derive the equations in a fixed frame of reference. The mass conservation relation may then be written down immediately, being the same as in the usual shock jump relations:

$$\rho_1 u_1 = \rho_2 u_2 \quad . \tag{8.1}$$

We next consider the energy conservation relation. We treat the region between r_1 and r_2 as a "black box" in which energy is conserved but the detailed physical processes are not of interest, and we consider the rates of energy inflow and outflow across the two surfaces of this region. First of all we have the mechanical energy transport terms, which are the same as in the usual adiabatic shock jump relations. The mechanical energy flux into the shock region at r_2 is equal to $\rho_2 |u_2| (H_2 + \frac{1}{2} u_2^2)$, and the mechanical energy flux out of the shock region at r_1 is $\rho_1 |u_1| (H_1 + \frac{1}{2} u_1^2)$ (ergs/cm^2/sec). In these expressions $H = E + PV$ is the specific enthalpy (enthalpy per unit mass), which includes the transport of internal energy plus the mechanical work done on the material inside a particular surface by the material outside that surface. In addition, we have the term $\frac{1}{2}u^2$ representing the flux of kinetic energy. (See for example Liepmann and Roshko 1957, ch. 2.)

In addition to the mechanical energy transport we also have to consider radiative energy flow into and out of the shock region. Let F_{int} denote the net radiative flux at r_1 (ergs/cm^2/sec) travelling outward from the interior of the core. This quantity can be considered as known, given the interior structure of the core, and it counts as an energy input to the shock region. Let F_s denote the net outward flux of radiation right at the shock jump; this will consist mainly of radiation emitted outward from the hot material inside the shock jump, with a small negative contribution from radiation travelling inward from the material outside the shock front. The net radiative flux leaving the shock region at r_2 will in general be less than F_s because part of the flux is absorbed between the shock jump and r_2. It has been arbitrarily assumed in the calculations that the flux is reduced by a factor of $e^{-\tau}$ between the shock jump and r_2, where τ is the optical depth between R and r_2; the net outward flux at r_2 is then equal to $e^{-\tau}F_s$. If we now collect the energy inflow and outflow rates for the shock region and equate the gains to the losses, we have

$$\rho_2 |u_2| (H_2 + \tfrac{1}{2}u_2^2) + F_{int} = \rho_1 |u_1| (H_1 + \tfrac{1}{2}u_1^2) + e^{-\tau}F_s \; . \qquad (8.2)$$

Actually the factor $e^{-\tau}$ in the above equation is not correct, except qualitatively, since it fails to take into account of all the physics of the situation. It was not thought that the use of the factor $e^{-\tau}$ would cause any serious error in the results, since the choice of the point r_2 is rather arbitrary anyway, being mainly a matter of numerical convenience (see section B.3). Examination of the results shows that in Case 1 the above procedure should introduce no significant error in the results; this has been verified by trial calculations using different choices of τ. In some of the other cases the situation is more complicated (see section 9.3), and it is more difficult to be sure that no serious error has been made; however it again appears from calculations made using different procedures that the error is probably not serious. In any case, the error can affect only the early stages of the evolution of the core; the latter stages and the properties of the resulting star are virtually unaffected, as is again verified by trial calculations.

We have still to evaluate the net radiative flux F_s at the shock jump. First of all, it turns out that for our purposes the inward radiative flux from material outside the shock front can be neglected without making any significant difference to the results. F_s may then be taken as just the outward radiative flux from the hot material inside the shock jump. It is convenient to define an effective temperature T_e for the shock front or stellar core by setting $F_s = \sigma T_e^4$. The problem is then to relate T_e to the values of the flow variables inside the shock front. In particular, we would like to relate T_e to T_1, the limiting temperature reached inside the shock front after radiative cooling has become negligible.

To do this in general would be a very complicated problem in radiative transfer, requiring a complete solution for the radiation field and the temperature distribution as a function of optical depth inside the shock front. This problem seems not to have been solved before, but to tackle it in detail would be out of the question for the present project. Therefore we are forced to rely on some simple approximation. We note first of all that T_e must be intermediate between the peak temperature at the shock jump and the limiting temperature T_1 inside the shock jump. Thus for the early stages of the core accretion process, when the peak temperature is not much different from T_1, we could as an adequate approximation just set $T_e = T_1$. The more important situation, however, occurs during the later stages of the collapse, when the peak temperature becomes orders of magnitude higher than either T_e or T_1. In these circumstances T_e is essentially fixed by the mechanical energy inflow to the shock front, and the problem becomes to determine how far below T_e the temperature inside the shock front drops before leveling off at a constant value T_1. We know that a radiative energy flux of σT_e^4 is emitted outward from the hot material just inside the shock jump; a similar amount of energy must also be radiated inward, and one would therefore expect the radiation intensity inside the shock front to be comparable with or at least not much less than that for a blackbody of temperature T_e. Thus it would seem unlikely that the temperature inside the shock front could drop much below T_e before leveling off at a constant value. Accordingly we have adopted in the calculations the following simple approximation:

$$T_e = T_1 \quad . \tag{8.3}$$

This approximation clearly gives an underestimate for T_e, or since in practice it is usually T_e which is fixed, it gives an overestimate for T_1 and for the interior temperature in the core generally.

An upper limit on the error in equation (8.3) can be set by a simple and general argument based on the radiative equation of transfer; the derivation is given in Appendix E. The result is that we must always have

$$T_1{}^4 > \frac{3}{8} T_e{}^4 \quad ,$$

i.e.

$$T_1 > 0.78\, T_e \quad . \tag{8.4}$$

Thus the error in eqn. (8.3) can at most be a factor of 0.78 in T_1. Considering that the actual error will probably be somewhat less than this limit and that the general level of accuracy sought in the calculations is only about 20% anyway, it appears that eqn. (8.3) is an adequate approximation for the present purposes.

Of course when the accretion rate falls off and the shock front becomes a stellar atmosphere the above considerations are no longer relevant. The choice of a suitable point r_1 inside the shock jump then becomes a matter of choosing a suitable photospheric boundary point for a stellar interior model. The usual practice is to take the boundary point to be that point in the stellar atmosphere at which the actual temperature is equal to the effective temperature. In the present case this choice of boundary point is very conveniently achieved by simply retaining equation (8.3) throughout the calculations.

We can now finally write the energy conservation relation (8.2) in the form actually used in the calculations. We make use of the mass conservation relation $\rho_1 u_1 = \rho_2 u_2$, and we substitute $F_s = \sigma T_e^4 = \sigma T_1^4$. We then have

$$\rho_2 |u_2| (H_2 + \tfrac{1}{2}u_2^2 - H_1 - \tfrac{1}{2}u_1^2) + F_{int} = e^{-\tau} \sigma T_1^4 \; . \qquad (8.5)$$

We now have two relations between the values of the variables at r_1 and r_2, i.e. equations (8.1) and (8.5). A third relation is required, corresponding to the momentum equation in the ordinary shock jump relations. In the present situation we require a more general relation, which we shall derive from the Eulerian differential equation (6.7). We multiply eqn. (6.7) by ρ, obtaining

$$\rho \frac{\partial u}{\partial t} + \rho u \frac{\partial u}{\partial r} + \frac{\partial P}{\partial r} + g\rho = 0 \quad , \qquad (8.6)$$

where $g \equiv Gm/r^2$ can be taken as constant throughout the shock region. We then integrate eqn. (8.6) with respect to r between r_1 and r_2, taking account of the constancy of ρu and neglecting the time derivative term because we have very nearly a steady flow; the result is

$$\rho_2 u_2^{\,2} - \rho_1 u_1^{\,2} + P_2 - P_1 + g\int_{r_1}^{r_2} \rho \, dr = 0 \, .$$

Here the contribution to the integral term from material outside the shock jump is always negligible, so the upper limit on the integral may be replaced by the shock jump radius R; this equation can then be written

$$P_1 + \rho_1 u_1^{\,2} = P_2 + \rho_2 u_2^{\,2} + g\int_{r_1}^{R} \rho \, dr \, . \tag{8.7}$$

Initially the integral term in eqn. (8.7) is negligible, and the equation becomes just the ordinary momentum relation for a shock front. Toward the end of the collapse, however, when the infall rate falls off and the shock front becomes a stellar atmosphere, P_2, ρ_2, and u_1 all become negligibly small, and it is the integral term in eqn. (8.7) which determines the photospheric pressure P_1. In fact equation (8.7) then becomes just the integrated form of the hydrostatic equilibrium equation for a stellar atmosphere, i.e.

$$dP = - g\rho \, dr = \frac{g}{\kappa} \, d\tau \, . \tag{8.8}$$

By definition, the photospheric pressure P_1 is the pressure at that point in the stellar atmosphere where the actual temperature T_1 is equal to the effective temperature T_e. According to the Eddington approximation, which will suffice for the present purposes, this occurs at an optical depth of 2/3. Accordingly, since both P and τ at the shock jump eventually become negligibly small, we obtain P_1

in this limit just by integrating equation (8.8) between $\tau = 0$ and $\tau = 2/3$. If we assume a relation of the form $\kappa \propto P^{\alpha}$, the result is

$$P_1 = \frac{2}{3}(1 + \alpha)\frac{g}{\kappa_1} \quad . \tag{8.9}$$

If we assume the material to be isothermal for $\tau \leq 2/3$ and use formula (2.1) for the opacity, we have $\alpha = \frac{1}{2}$; the right hand side in eqn. (8.9) then becomes just g/κ_1. This is of course only an approximation, but it should be quite adequate for our purposes. We can now substitute this expression in place of the integral term in eqn. (8.7) to obtain the required generalization of the shock momentum relation:

$$P_1 + \rho_1 u_1^{\,2} = P_2 + \rho_2 u_2^{\,2} + \frac{g}{\kappa_1} \quad . \tag{8.10}$$

Throughout much of the collapse the last term in eqn. (8.10) is only of minor importance, so this equation cannot be significantly in error. Equation (8.10) also gives a satisfactory approximation in the stellar atmosphere limit, as has been discussed above. It is less readily justified during those stages of the collapse, particularly toward the end, when the last term becomes important even though infall effects are still of major importance. However, although the situation becomes quite complicated, the effect of the last term in eqn. (8.10) will always be approximately to make P_1 equal to the pressure at an optical depth of the order of unity inside the shock jump. This seems reasonable, since T_1 is supposed to represent the temperature at an optical depth of the order of unity. In any case, eqn. (8.10) does not appear to have been responsible for any major errors in the results, and considering the other uncertainties and the accuracy of the calculations, it appears to be adequate for the present purposes. We now have all the equations required to treat the shock front, namely equations (8.1), (8.5), and (8.10). The way in which these equations have been incorporated in the numerical method is described in Appendix B.

8.2 Convection

We have used a simplified form of the conventional mixing length treatment of convection, as given for example by Vitense (1953). First, we shall re-derive the usual expression for the convective heat flux in a simpler and for our purposes more convenient form. It is known from elementary gas dynamics that the energy (thermal plus mechanical) transported per unit mass by a flowing fluid is given by the specific enthalpy $H = E + PV$. We suppose that the convective elements passing a particular point move with an average velocity v and have an average enthalpy exess (or deficiency) relative to the surroundings of δH. We assume pressure equality between the element and its surroundings, in which case $\delta H = T\delta S + V\delta P = T\delta S$, where S is the specific entropy. Since the average mass flux is ρv, the convective energy flux is then

$$F_c = \rho v T\delta S. \tag{8.11}$$

We assume the convective elements to move isentropically, and we suppose that they move a total distance ℓ (the "mixing length") before merging with the surroundings. The average entropy excess will then be approximately

$$\delta S = -\frac{\ell}{2}\frac{dS}{dr} ,$$

and the expression for the convective flux then becomes

$$F_c = -\tfrac{1}{2}\rho v \ell \frac{T\,dS}{dr} . \tag{8.12}$$

For a perfect gas this expression becomes identical with the one usually given for the convective flux, apart from our neglect of radiative cooling or heating of the convective elements. Equation (8.12) is of course applicable only if $dS/dr < 0$, i.e. if the material is unstable against convection; if $dS/dr > 0$ the material is stable against convection and there is no convective heat flux.

We have assumed the mixing length ℓ to be equal to some constant α times the density scale height, i.e.

$$\ell = -\alpha \frac{dr}{d\ln\rho} = \alpha \frac{dr}{d\ln V} .$$

The convective flux can then be written

$$F_c = -\frac{\alpha v}{2}\,\frac{T\,dS}{dr}\Big/\frac{dV}{dr} ,$$

or

$$F_c = -\frac{\alpha v}{2}\frac{T\,dS}{dV} = -\frac{\alpha v}{2}\,\frac{dE + P\,dV}{dV} \tag{8.13}$$

where the differentials here represent differences taken between neighboring points in the convection zone. In the numerical calculations these differentials are of course replaced by differences between adjacent grid points. We have not considered it worthwhile to follow the usual mixing length calculations for v (which give some unphysical results), but have simply considered αv as an undetermined parameter for which some arbitrary but reasonable value might be inserted. A plot of v vs. r for pre-main sequence stars given by Ezer and Cameron (1963) suggests that 1 km/sec may be a reasonable order of magnitude value for v; accordingly αv has in most cases been set equal to 1 km/sec. The only exception is Case 6, in which we have used 2 km/sec.

Clearly the whole procedure outlined above for calculating the convective flux is only a very crude order-of-magnitude approximation. The mixing length theory is itself only a rather uncertain approximation to reality, and our procedure is only an approximation to the mixing length theory. By way of justification of this rough approach, we mention here that the results of the calculations do not seem for our purposes to be very sensitive to the parameter αv; also, comparison of the end result with previous pre-main sequence calculations shows rather satisfactory agreement, considering the accuracy of our calculations.

8.3 Radiation Transfer in the Infalling Cloud

During the initial stages of the formation of the stellar core, the infalling material outside the shock front is still optically thick out to about the position of the first shock front, and the radiation diffusion equation (6.10) correctly describes the radiation transfer in this region. The outer part of the infalling cloud of course remains optically thin, and the diffusion equation is inapplicable in this region; however, as was mentioned in section 6, its use does not at this stage lead to serious errors in the temperature of the infalling cloud.

As the collapse proceeds, the density and optical depths in the infalling cloud decrease. Before long the density just outside the stellar core drops to the point where the luminosity emitted from the shock front is no longer completely absorbed in the material just outside the shock front, but is transported outward through the whole infalling cloud. This radiation then heats up the infalling material, and in fact becomes the dominant heating effect determining the temperature throughout the infalling cloud. The temperature at any point depends on a detailed solution of the radiation transfer problem, but it must be at least as high as the local effective temperature defined by the luminosity and radius at that point. This is not properly taken into account by the diffusion equation, which produces temperatures which are much too low under these circumstances.

It turns out rather fortunately that this error has little effect on the dynamics of the collapse, at least as far as the inner part of the collapsing cloud and the stellar core are concerned. The material in the inner part of the cloud soon comes very nearly into free fall anyway, even if the temperature is correctly calculated, so that the error in temperature caused by the use of the diffusion equation can have little effect on the dynamics of the infall in this region. Also, during the later stages of the collapse the thermal energy and pressure of the material falling into the shock front become negligible compared with the kinetic energy and pressure; consequently the temperature of the infalling material is of negligible importance for the properties of the shock front and stellar core, and the error in the temperature makes no significant difference to the results. For these reasons we have continued to use the diffusion equation (6.10) throughout the calculations, even though its application eventually becomes rather meaningless.

It was thought when the calculations were made that the error in the dynamics caused by not properly calculating the temperature would be negligible throughout the whole collapsing cloud. On re-examining the results it appears that this is not true in the outermost part of the cloud, where at the time of peak core luminosity the outward pressure gradient force in reality becomes comparable with or possibly greater than the inward gravitational force if the temperature is correctly calculated. Whether the effect would be sufficient to stop or reverse the collapse in the outermost part of the cloud is not clear, but the collapse in this region would at least be significantly retarded. This would have the effect of reducing the mass inflow rate during the later stages of the collapse and hence of reducing the surface temperature, luminosity, and radius of the stellar core, as explained in section 9.4. The main results can hardly be seriously invalidated, at least qualitatively, and the error may perhaps be no greater than the effects of some of the other uncertainties in the problem. Nevertheless, this appears to be one respect in which an improved treatment would probably have been desirable.

Of course the procedure which we have used does not allow us to say anything about the actual temperature distribution or the spectrum of the radiation emitted from the infalling cloud. This however may be treated as a separate problem (at least within the approximation which we have employed, in which the radiation transfer problem is ignored in calculating the dynamics), and we shall consider it separately in Part III.

Radiation pressure has been neglected throughout the calculations, mainly because it was expected that it would be unimportant, at least for one solar mass. In any case, the radiation pressure would have been difficult to calculate with any accuracy since this would have required a solution of the radiation transfer problem and a good knowledge of the optical properties of the dust grains. Examination of the results indicates that radiation pressure is negligible at all times in Cases 1, 4, and 5 but possibly of some importance in the other cases, particularly Case 7.

9. RESULTS FOR THE LATER STAGES OF THE COLLAPSE

9.1 Explanation of the Calculations

The calculations to be described in this section are continuations of the calculations for the seven cases already described in section 7. The defining characteristics of these cases are listed in Table 2 (p. 41). In Case 6 we have made one change in assumptions from those listed in Table 2: the later stages of the collapse have been calculated with the boundary condition $u = 0$, as in all the other cases, rather than the boundary condition $P = \text{const.}$ which was used for the early stages of the collapse. Thus in Case 6 the outer boundary of the cloud contracts during the early stages of the collapse by about a factor of 2 in radius, but is held fixed during the later stages of the collapse at a radius of 8.6×10^{16} cm.

The numerical method used for calculating the later stages of the collapse is described in detail in Appendix B. In each case the changeover in numerical method from that used for the early stages of the collapse was made at a time shortly after the formation of the stellar core; thus the "later stages of the collapse" to be described in this section include virtually the whole evolution of the stellar core. The change in numerical method introduced some perturbations in the structure of the stellar core during the first few time steps, but these perturbations soon died out and caused no significant errors in the further evolution of the core. It is believed that the hoped for level of accuracy of about 20% or so was maintained throughout the calculations for the later stages of the collapse.

9.2 The Initial Adiabatic Phase of the Accretion Process

When the stellar core first forms, the density and opacity in the stellar core and in the surrounding material are so high that radiative energy transfer is completely negligible on the relevant time scale, and the flow is therefore adiabatic. The shock front bounding the stellar core is initially also adiabatic, since the radiative energy transport across the shock jump is initially negligible compared with the mechanical energy flux. In some cases the shock front remains effectively adiabatic even after the radiative energy flux across the shock front does become significant, because the radiation is immediately totally reabsorbed in the infalling material just outside the shock front and the energy is carried back into the shock front in the form of thermal energy.

The initial values of the flow variables just inside the shock front are given approximately by $u_1 \simeq 3 \times 10^5$ cm/sec, $\rho_1 \approx 10^{-4}$ gm/cm^3, and $T_1 \simeq 10^4$ °K, whereas the values of these variables just outside the shock front are approximately $u_2 \simeq 2 \times 10^6$ gm/sec, $\rho_2 \approx 10^{-5}$ gm/cm^3, and $T_2 \simeq 4 \times 10^3$ °K. Under these conditions the kinetic energy per unit mass $\frac{1}{2} u_1^{\,2}$ just inside the shock front is negligible compared with the specific enthalpy H_1, so that the shock energy equation (8.5) becomes, for an adiabatic shock front,

$$H_1 = H_2 + \tfrac{1}{2} u_2^{\,2} \; . \tag{9.1}$$

The specific enthalpy H_2 outside the shock front is initially about half as large as the kinetic energy per unit mass $\frac{1}{2} u_2^{\,2}$, but it decreases in importance as the collapse proceeds, eventually becoming negligible in comparison with the kinetic energy of the infalling material.

As the collapse proceeds and the material in the inner part of the collapsing cloud falls into the stellar core, the density ρ_2 of the infalling material just outside the shock front drops rapidly, decreasing by about 2 or 3 orders of magnitude during the adiabatic phase of the accretion process. As a consequence mainly of the shock momentum equation (8.10), the density ρ_1 inside the shock front also drops rapidly, remaining about one order of magnitude higher than ρ_2. At the same time the temperature and enthalpy of the incoming material also decrease, whereas it turns out in most cases that the infall velocity u_2 just outside the shock front remains approximately constant (see below). Consequently the specific enthalpy and temperature inside the shock front also decrease in accordance with equation (9.1), but only by a relatively moderate amount since only H_2 decreases while the dominant term $\frac{1}{2}u_2^2$ remains nearly constant; thus the temperature T_1 inside the shock front decreases by only a factor of 2 or 3 during the adiabatic phase of the collapse, compared with a decrease of 2 or 3 orders of magnitude in ρ_1. As a result of the large decrease in density in the outer part of the stellar core coupled with a relatively small change in temperature, the core radius increases substantially during the adiabatic phase of the collapse.

For purposes of discussing and understanding the structure and evolution of the stellar core, particularly the way in which the radius varies with time, it is convenient to make use of the specific entropy (entropy per unit mass) of the core material. It is a simple consequence of the equations of stellar structure, although one not usually mentioned, that the radius of a stellar hydrostatic equilibrium configuration of given mass is uniquely determined by the specific entropy of the material; the radius increases with increasing specific entropy, being particularly sensitive to the entropy in the outer layers of the object. If the entropy per unit mass is fixed, the radius of the object depends inversely on the mass. In the case of our stellar core, the specific entropy of each mass element added to the core is determined when the mass element passes through the shock front; thereafter the entropy remains constant, because all heat transfer processes are initially negligible in the interior of the core. Thus the radius of the core is determined essentially by the specific entropy of the material entering the core just inside the shock front; the higher the specific entropy just inside the shock front, the larger the radius of the core. We can thus understand the rapid increase in the core radius during the adiabatic phase of the collapse as being due to the rapid increase in specific entropy inside the shock front, caused by the large decrease in ρ_1 coupled with a relatively small change in T_1.

The reason why the infall velocity u_2 just outside the shock front remains approximately constant at about 2×10^6 cm/sec during the adiabatic phase of the collapse may be understood as follows. The increase in specific enthalpy of the material as it passes through the shock front is accounted for mainly by the dissociation of hydrogen molecules, with only a relatively small contribution from the increase in the thermal energy of the particles. Consequently, once all the hydrogen molecules are dissociated, the specific enthalpy H_1 inside the shock front increases relatively slowly with increasing temperature, remaining almost constant at about 2×10^{12} ergs/gm for temperatures in the range $4 \times 10^3 \lesssim T_1 \lesssim 10^4$ °K. Suppose now for example that the infall velocity u_2 should increase slightly; the specific enthalpy H_1 would then also increase slightly in accordance with eqn. (9.1), and therefore, according to the above discussion, there would be a relatively large increase in the temperature T_1. The resulting increase in the specific entropy just inside the shock front would then cause an increase in the core radius R. However, since the infalling material just outside the shock front is nearly in free fall, we have

$$\tfrac{1}{2} u_2^{\,2} \approx \frac{GM}{R} \qquad (9.2)$$

where M is the core mass; thus an increase in the core radius R would tend to reduce u_2 again and bring it back to its former value. Consequently u_2 and also the ratio M/R tend to remain approximately constant as the collapse proceeds and the core grows in mass. The values of u_2 and M/R during the adiabatic phase of the collapse are determined approximately by

$$\frac{GM}{R} \approx \tfrac{1}{2}u_2{}^2 \approx H_1 \approx 2 \times 10^{12} \text{ ergs/gm.} \tag{9.3}$$

This gives $u_2 \approx 2 \times 10^6$ cm/sec, in agreement with the results of the calculations. This argument is valid only if T_1 is in the range $4 \times 10^3 \lesssim T_1 \lesssim 10^4$ °K, but this is in fact usually the case.

As was seen just above, the ratio M/R tends to remain approximately constant during the adiabatic phase of the collapse, so that the radius of the core increases roughly proportionally with its mass. During the adiabatic phase of the accretion process, the core mass increases by about one order of magnitude from an initial value of about 10^{-3} $M_{\odot}$ (see Table 4, p. 60) to a value of the order of 10^{-2} $M_{\odot}$, and the core radius likewise increases by about one order of magnitude from an initial value of the order of 1 $R_{\odot}$ to a maximum value of the order of 10 $R_{\odot}$. At this point, which occurs about one year after the time of formation of the stellar core, radiative energy losses from the shock front start to become important, the entropy of the material inside the shock front begins to decrease, and the core stops expanding and begins to contract. Some properties of the core at the time of maximum radius are listed in Table 6 (p. 92); this table gives the time elapsed since the formation of the stellar core, as well as the mass, radius, and surface temperature of the core at this time. The density ρ_1 just inside the shock front is in all cases of the order of 10^{-7} gm/cm^3 at this time, and the density ρ_2 outside the shock front is of the order of 10^{-8} gm/cm^3. Some of the data in Table 6 are rather uncertain for various reasons (see the following

TABLE 6

PROPERTIES OF THE CORE AT THE TIME OF MAXIMUM RADIUS

Case No.	t (yrs)	$M/M_\odot$	$R/R_\odot$	T_1 ($^\circ$K)
1	0.9	.010	12	3300
2	1.9	.026	19	7700
3	1.3	.013	14	3700
4	0.5	.003	6	2600
5	~0.1	.034	~20	~2500
6	1.1	.016	17	4700
7	2.2	.027	21	7400

section), and they are presented here mainly for illustrative purposes.

At the end of the adiabatic phase of the collapse, i.e. at the time of maximum core radius, most of the mass which originally constituted the first core (section 7.3) has fallen into the second (stellar) core, and the density in the region originally occupied by the first core has dropped by a large factor. The first shock front, i.e. the one bounding the first core, is still in existence and has not changed much in position or other properties since the formation of the stellar core, but the density just inside the first shock front is beginning to drop significantly as material falls away from it. The time elapsed is still too short for any appreciable changes to have taken place outside the first shock front.

In Case 5 the situation during the adiabatic phase of the collapse is again somewhat different from the other cases. In Case 5 the second shock front (of three) disappears during the adiabatic phase, leaving only 2 shock fronts as in all the other cases. The adiabatic phase of the collapse is in this case relatively short lived, and the core mass increases only slightly while the radius increases by roughly a factor of 3. At the end of this time, however, as we see in Table 6, the properties of the stellar core in Case 5 are not very different from those in the other cases. From this point onward the evolution of the stellar core in Case 5 is qualitatively similar to the other cases.

The evolution of the stellar core in an HR diagram is plotted for each of the seven cases in Figs. 5 - 11 (pp. 126 - 138). The adiabatic phase of the evolution is represented in each case by the initial dashed section of the curve. During the adiabatic phase this curve has significance only as a plot of the radius vs. the surface temperature of the core as it evolves; the luminosity indicated by the curve has no observational significance, since the radiation emitted from the surface of the core is totally reabsorbed in the infalling material just outside the shock front and therefore never escapes from the protostellar cloud.

9.3 Early Non-Adiabatic Phases of the Evolution of the Core

When the density ρ_2 outside the shock front gets down to about 10^{-8} gm/cm^3, a significant amount of energy begins to be lost from the shock front in the form of radiation. In Case 1 the situation for the transition from an adiabatic to a non-adiabatic shock front is relatively simple. For values of ρ_2 greater than about 10^{-8} gm/cm^3 the rate of mechanical energy inflow to the shock front is greater than the maximum possible outward radiative energy flux σT_1^4, so that radiation must be of negligible importance regardless of any considerations of radiation transfer in the vicinity of the shock front. For values of ρ_2 less than about 10^{-8} gm/cm^3, however, σT_1^4 becomes comparable with the mechanical energy inflow and at the same time the opacity outside the shock front becomes low enough that the radiative energy flux σT_1^4 can be transported away from the shock front and eventually escape entirely from the protostellar cloud, even though the cloud remains optically thick.

In some of the other cases, particularly Cases 2 and 7, the situation is less simple. In these cases σT_1^4 becomes comparable with the mechanical energy flux at an earlier stage in the collapse when ρ_2 is of the order of 10^{-7} gm/cm^3 or higher and the opacity outside the shock front is still quite high. In this case the incoming material immediately outside the shock front is heated up to almost the same temperature as the material inside the shock front, so that the net radiative flux across the shock front is considerably reduced from σT_1^4. Even this reduced energy flux however is completely absorbed in the incoming material just outside the shock front, and no significant radiative energy flux escapes entirely from the vicinity of the shock jump. Thus the shock front remains effectively adiabatic until the density ρ_2 drops to some critical value such that it is no longer possible for the radiation flux to be completely absorbed just outside the shock front. The situation is complicated by the fact that the opacity of the incoming material increases very rapidly with increasing temperature. The computational method which we have used (sections 8.1 and B.2) does not take all of these effects properly into account, and it is difficult to tell just what kind of error may have been made, although hopefully it is not too serious.

In any case, after the density ρ_2 gets much below 10^{-8} gm/cm^3 the shock front can no longer remain adiabatic, and a radiative energy flux essentially equal to σT_1^4 (see section 8.1) is radiated away from the shock front and transported outward through the protostellar cloud, eventually escaping from the cloud altogether.

As a result, when the shock front becomes non-adiabatic the luminosity leaving the protostellar cloud rapidly increases by a large factor, becoming essentially equal to the luminosity emitted from the shock front. In the HR diagrams for the evolution of the stellar core plotted in Figs. 5 - 11 (pp. 126 - 138) this is indicated by the transition from a dashed curve to a solid curve; in each case the beginning of the solid curve represents the point where approximately 90% of the luminosity emitted from the shock front escapes entirely from the protostellar cloud. Because of the very large optical depth still produced by the dust grains in the infalling cloud, this luminosity eventually leaves the cloud in the far infrared as thermal emission from the dust grains. We shall consider in Part III the radiation transfer problem in the infalling cloud and the spectrum of the emitted radiation.

Another consequence of the radiative energy loss from the shock front, as mentioned earlier, is that the specific entropy of the material just inside the shock front stops increasing and begins to decrease, with the result that the core radius also stops increasing and begins to decrease. At the same time, because of the decreasing entropy of the material entering the core, the entropy gradient in the outer part of the core becomes negative; this means that the material in this region becomes unstable against convection, and convection begins. At this stage the existence of a convection zone in the outer part of the core makes no essential difference to the evolution of the of the core; its main effect is to transfer heat energy from the inner to the outer part of the core, thus preventing the entropy in the outer part of the core and hence the core radius from decreasing as fast as would otherwise be the case.

After the shock front becomes non-adiabatic and the core radius begins to decrease, the details of the evolution are somewhat different in the various cases. As an example we shall describe Case 1 in some detail, since it combines all of the features found in the other cases. In Case 1 the density outside the shock front continues to drop rapidly, while the mass and radius of the core and the velocity of infall change relatively slowly. Consequently the temperature and density just inside the shock front continue to decrease. Because of the decreasing opacity of the surface layers of the core, due mainly to the decreasing temperature, radiative transfer starts to become important near the surface of the core, and a significant amount of energy is lost by radiation from the surface layers. This energy loss is replenished by convective heat transport from the interior of the core, so that we have a net energy outflow from the interior of the core which eventually is radiated away at the surface. Meanwhile the rate of kinetic energy inflow to the shock front decreases rapidly due to the decreasing density of the infalling material, and a point is soon reached where the energy input to the shock region comes mainly from the interior of the core and not from the kinetic energy inflow. The shock region then becomes essentially a stellar atmosphere, as was discussed in section 8.1. The mass and radius of the core at this point are approximately $.011\ M_\odot$ and $9\ R_\odot$

respectively (Case 1), and the surface temperature T_1 reaches a minimum value of about 2600 °K. The core luminosity is about $3L_\odot$, about 80% of which comes from the interior of the core and 20% from the kinetic energy inflow. The convective zone at this time occupies approximately the outer 30% of the mass and the outer 75% of the radius. The time elapsed since the formation of the stellar core is approximately 7 years.

Subsequently, as the core loses energy by radiation it contracts and decreases in luminosity, while the surface temperature increases slightly. This phase of the evolution of the core is quite analogous to the pre-main sequence contraction of a star along the convective "Hayashi track," as studied for example by Hayashi et al. (1962). In the HR diagram plotted in Fig. 5 (p. 126), this phase of the evolution is represented by the section of the curve between approximately 10 and 100 years after the formation of the core. During this phase the core mass increases only slightly to about $.013\ M_\odot$, while the radius decreases by about a factor of 2 to about $5\ R_\odot$. Because of the increasing mass and decreasing radius of the core, the infall velocity u_2 finally begins to rise significantly above its initial value of about 2×10^6 cm/sec, with the result that the rate of kinetic energy inflow to the shock front stops decreasing and begins to increase. Since the energy outflow from the interior of the core is at the same time decreasing as the core contracts, the kinetic energy inflow becomes more and more important and soon becomes once again the dominant energy input to the shock front. For this reason the surface temperature during this contracting phase of the evolution rises somewhat faster than would otherwise be the case.

Eventually, because of the increasing temperature and opacity and the decreasing importance of radiative energy losses inside the shock front, the specific entropy of the material entering the core stops decreasing and begins to increase again. One consequence of this is that the core stops contracting; also, the entropy gradient in the outer part of the core becomes positive and convection ceases. At this point, which occurs about 130 years after the formation of the core, the surface temperature of the core is about 3000 °K and the luminosity reaches a minimum value of about 1.5 $L_\odot$. During the subsequent evolution of the core it turns out that the core radius remains nearly constant while the mass, surface temperature, and luminosity of the core all increase greatly. We shall continue in section 9.4 the description of these later stages of the evolution of the core.

In Cases 3, 4, and 6 the early evolution of the core after the shock front becomes non-adiabatic is similar to Case 1, except that in none of these cases does the energy loss from the interior of the core ever become as important as in Case 1. Consequently the decrease in core radius arising from this energy loss is less in these cases than in Case 1, amounting to only about 20 - 30% instead of a factor of 2. In the HR diagrams in Figs. 7, 8, and 10 (pp. 130 - 136) this brief contracting phase is represented in each case by the section of the curve nearest the point of minimum core surface temperature.

In Case 5 the stellar core is already essentially in the convective contracting phase of evolution when the shock front becomes non-adiabatic; thereafter the evolution is qualitatively similar to Case 1, although the numerical details are of course different. In Cases 2 and 7 the situation is qualitatively different from the other cases: because of the higher density of the protostellar cloud and the shorter collapse time, the mechanical energy inflow to the shock front is always dominant and energy losses from the interior of the core never become important at all. The surface temperature reaches a minimum value of about 4000 °K and then begins to rise again because of the increasing kinetic energy inflow rate. However, in these cases the specific entropy of the material entering the core continues to decrease slightly, so the core radius continues to decrease slowly as the surface temperature rises (see Figs. 6 and 11, pp. 128 and 138).

In all cases, by the end of the contracting phase of evolution described above, all traces of the first core and of the shock front bounding it have disappeared. Essentially all of the mass in the inner part of the collapsing cloud has by this time fallen into the stellar core, so that practically all of the protostellar mass is now either in the stellar core or some distance out in the collapsing cloud where the material has not yet had time to fall inward significantly since the formation of the stellar core. Under these circumstances the form of the density distribution in the inner part of the collapsing cloud may be derived from the following simple argument: We start with the Eulerian continuity equation (6.6), which we write in the form

$$\frac{\partial m}{\partial t} = - 4\pi r^2 \rho u \quad . \tag{9.4}$$

Since there is negligible mass in the innermost part of the collapsing cloud, the mass variable m is essentially constant (independent of r) in this region, and $\partial m/\partial t$ must therefore also be independent of r in this region; consequently, from eqn. (9.4) we have $r^2\rho u$ = const. Since the material in this region is essentially in free fall, we have

$$\tfrac{1}{2} u^2 = \frac{Gm}{r} \tag{9.5}$$

and consequently, since m is constant, we have $u \propto r^{-\frac{1}{2}}$. Substituting this in $r^2\rho u$ = const. we obtain $r^{3/2}\rho$ = const., i.e.

$$\rho \propto r^{-3/2} \; . \tag{9.6}$$

This form for the density distribution in the innermost part of the collapsing cloud is well verified in all cases by the results of the calculations.

The above considerations are of course valid only for the innermost part of the protostellar cloud where the mass has been substantially depleted. In the outer part of the cloud the time elapsed is still too short for any significant changes to have taken place since the formation of the stellar core, and the density distribution is still approximately of the form $\rho \propto r^{-2}$. In Case 1 at the end of the con-

contracting phase of the evolution of the core described above, i.e. slightly over 100 years after the formation of the stellar core, the change from the density law $\rho \propto r^{3/2}$ to the law $\rho \propto r^{-2}$ occurs at a radius of approximately 10^{15} cm.

Since there is negligible mass in the innermost part of the collapsing cloud, the time scale for growth in mass of the core is no longer the time scale for collapse of the innermost part of the cloud but the time scale for collapse of that part of the cloud farther out from the core where most of the mass is coming from. As the collapse proceeds, the mass becomes substantially depleted farther and farther out in the cloud, and the region in which $m = \text{const.}$ and $\rho \propto r^{-3/2}$ expands outward. Consequently the region from which most of the mass falling into the core originates moves farther and farther out in the cloud, and the time scale for growth and evolution of the stellar core correspondingly becomes longer and longer.

9.4 Later Stages of the Evolution of the Core

As we have seen, whatever the details of the earlier evolution of the core, a point is always reached, still early in the history of the core, when energy losses from the interior of the core become unimportant and the conditions in the shock front and in the outer layers of the core become determined entirely by the properties of the infalling material. The important properties of the incoming material are the density ρ_2 and the velocity u_2 just outside the shock front; the temperature T_2 is unimportant since the thermal energy and pressure of the incoming material are by this time negligible compared with the kinetic energy and pressure. Since the material entering the shock front has been in free fall from an effectively infinite distance, its velocity u_2 is determined only by the mass and radius of the core through the relation

$$\tfrac{1}{2} u_2^2 = \frac{GM}{R} \ . \qquad (9.7)$$

Thus it is really only through the density ρ_2 and its variation with time that the evolution of the core depends on the structure and evolution of the infalling cloud.

The surface temperature and luminosity of the core are determined by the shock energy equation (8.5), in which the dominant terms are the kinetic energy inflow rate $\rho_2 |u_2| (\tfrac{1}{2} u_2^2)$ and the radiative energy loss term σT_1^4 (the factor $e^{-\tau}$ in eqn. (8.5) is by this time essentially equal to 1); these two terms increase greatly during the later stages of the evolution, and all the other terms in eqn. (8.5) soon become negligible by comparison. Thus for the later stages of the evolution of the core, eqn. (8.5) becomes

$$\sigma T_1^4 = \tfrac{1}{2} \rho_2 |u_2|^3 \ . \qquad (9.8)$$

What this equation means physically is simply that the radiative energy flux emitted from the shock front is equal to the rate of inflow of kinetic energy to the shock front. Thus the core surface temperature T_1 and the core luminosity $L = 4\pi R^2 \sigma T_1^4$ are determined entirely by the rate of inflow of kinetic energy, essentially all of which becomes converted into radiation in the shock front.

During the later stages of the evolution of the core, the core mass increases by a large factor, and consequently the infall velocity u_2 also increases by a large factor in accordance with eqn. (9.7). Meanwhile the density ρ_2 of the incoming material decreases as the material of the infalling cloud is depleted. Initially, however, the increase in $|u_2|^3$ in eqn. (9.8) overbalances the decrease in ρ_2, with the result that the kinetic energy inflow rate and the core surface temperature T_1 increase substantially, in accordance with eqn. (9.8). It turns out that the density ρ_1 just inside the shock front remains approximately constant as T_1 increases, and therefore the specific entropy of the material entering the core just inside the shock front continually increases during this phase of the evolution. As a result of the opposing effects of increasing specific entropy and increasing core mass, the radius of the core does not change much during this phase, decreasing by only a small or moderate factor while the core mass increases by a large factor. Consequently the core luminosity $L = 4\pi R^2 \sigma T_1{}^4$ increases by a large amount as the surface temperature T_1 rises. This phase of the evolution is represented in the HR diagrams in Figs. 5 - 11 (pp. 126 - 138) by the section of the curve where the surface temperature and luminosity increase substantially with relatively little change in radius; in Case 1 (Fig. 5), for example, this is the section of the curve between approximately 10^2 and 10^5 years after the formation of the core.

It should be noted that the HR diagrams in Figs. 5 - 11 do not represent what would be observed for the evolution of a protostar, since throughout the collapse the stellar core remains heavily obscured by the dust in the infalling cloud. The luminosity leaving the protostellar cloud is the same as the luminosity emitted from the surface of the stellar core, but the radiation comes out in the infrared as thermal emission from the dust grains (see Part III).

During these later stages of the accretion process the core radius is dependent mainly on the specific entropy of the material in the outer part of the core which has only recently been accreted with a relatively high specific entropy, and not so much on the material near the center of the core which was accreted at an earlier stage of the collapse with relatively low specific entropy. The original core material, for example, eventually becomes only a very small fraction of the core mass at the center, and the fact that its specific entropy is very low compared to that of the material in the outer part of the core has little effect on the radius or the structure of the outer part of the core. Thus the radius of the core is determined mainly by the recent history of the accretion process, and the influence of the earlier stages of the collapse is progressively damped out as the collapse proceeds. This is a fortunate situation, since it means that uncertainties or errors arising in the calculation of the earlier stages of the evolution of the core become unimportant for the later stages.

An illustration of the above discussion is provided by a comparison of the results in Cases 1 and 4, which differ in the assumed dust opacity but are the same in other respects. The initial properties and the early evolution of the core are significantly different in the two cases, and throughout the collapse the central specific entropy remains lower in Case 4 than in Case 1; nevertheless, during the later stages of the collapse the evolution of the core becomes practically identical in the two cases as far as the radius and the structure of the outer part of the core are concerned. This is evident in comparing Figs. 5 and 8, in which the curves become very nearly identical for the later stages of the evolution. A somewhat similar situation is seen in comparing the results in Cases 2 and 3 (Figs. 6 and 7), which differ in the assumed initial temperature of the protostellar cloud. Again there are substantial differences in the early evolution of the core, but during the later stages the two cases converge to very similar paths in the HR diagram. The remaining small differences between Cases 2 and 3 are attributable to differences in the density distribution in the outer part of the collapsing cloud. In fact, as will be explained in more detail below, all of the differences between Cases 1 - 5 in the later stages of the evolution are attributable almost entirely to differences in the density distribution of the infalling cloud and in its variation with time. This is an illustration of the fact mentioned earlier that it is really only the density of the infalling material that determines the properties of the shock front and hence the whole course of evolution of the stellar core.

We note in Figs. 5 - 11 that in cases where the surface temperature never gets up to 10^4 °K the core radius continues to decrease slowly as the point of maximum surface temperature is passed, whereas in cases where the surface temperature rises above 10^4 °K the radius stops decreasing and increases slightly before the point of maximum surface temperature is reached. The reason for this is that at temperatures of about 10^4 °K or higher the specific entropy inside the shock front rises particularly rapidly with increasing temperature because of the ionization of hydrogen at these temperatures. This effect is sufficient to enable the effect of increasing specific entropy to overcome the effect of increasing core mass and cause the core to expand somewhat.

The surface temperature and luminosity of the core continue to increase until approximately half of the total protostellar mass has fallen into the core. At this time the rate of increase of the infall velocity u_2 becomes insufficient to keep the kinetic energy inflow rate $\frac{1}{2}\rho_2|u_2|^3$ increasing despite the steadily decreasing infall density ρ_2; the decrease in ρ_2 then begins to predominate over the increase in $|u_2|^3$, and the kinetic energy inflow rate begins to decrease. Consequently the surface temperature and luminosity of the core also begin to decrease. Some of the important properties of the stellar core and of the infalling material at the time of maximum surface temperature and luminosity are listed for each case in Table 7 (p. 108). The times given in this table are the times elapsed since the formation of the stellar core.

In examining the data in Table 7, the near identity of the results in Cases 1 and 4 and the similarity of the results in Cases 2

TABLE 7

PROPERTIES OF THE CORE AT THE TIME OF MAXIMUM LUMINOSITY AND SURFACE TEMPERATURE

Case No.	t (yrs)	$M/M_\odot$	$R/R_\odot$	$L/L_\odot$	T_1 (^oK)	ρ_1 (gm/cm^3)	u_2 (cm/sec)	ρ_2 (gm/cm^3)
1	7.7 + 4	0.56	2.6	30	8300	3.4 - 8	3.3 + 7	1.6 - 11
2	1.2 + 3	0.37	6.2	430	10600	1.2 - 7	1.7 + 7	2.9 - 10
3	2.1 + 3	0.49	6.7	600	11100	1.2 - 7	1.9 + 7	2.5 - 10
4	7.7 + 4	0.57	2.7	29	8200	3.3 - 8	3.2 + 7	1.5 - 11
5	2.9 + 4	0.55	3.4	56	8600	4.2 - 8	2.8 + 7	2.7 - 11
6	7.6 + 3	0.83	6.1	430	10700	7.8 - 8	2.6 + 7	8.6 - 11
7	4.9 + 3	1.70	9.4	1430	11600	7.9 - 8	3.0 + 7	7.9 - 11

and 3 are evident. Comparing the various data listed for Cases 1 - 5 (total mass = 1 $M_{\odot}$), it is apparent that the core radius R is closely correlated with the surface temperature T_1, which in turn is correlated with the infall density ρ_2. Comparison with the initial conditions listed in Table 2 (p. 41) shows, as might be expected, that the infall density ρ_2 is closely related to the initial density, or equivalently to the radius of the protostellar cloud. Thus it appears that the radius and surface temperature of the core at the time of maximum surface temperature and luminosity are determined primarily by the initial density or radius of the protostellar cloud and that other effects such as differences in the initial temperature, composition, or opacity are relatively unimportant.

This situation may be understood as follows: first of all, by the time that approximately half of the total protostellar mass has fallen into the stellar core, the form of the density distribution in the infalling cloud has become almost the same in all cases, namely $\rho \propto r^{-3/2}$ throughout almost the whole infalling cloud. Since the mass remaining in the infalling cloud at this time is approximately the same in all cases (Cases 1 - 5), the density at any point in the cloud will be inversely related to the radius of the cloud. Other things being equal, the rate of kinetic energy inflow to the shock front is proportional to the density of the infalling material, and therefore we expect the surface temperature of the core to increase with increasing density of the protostellar cloud. A higher surface temperature means a higher specific entropy for the material entering the core and consequently a larger core radius, particularly when, as is the case here, the surface temperature is near 10^4 °K; the specific entropy inside the shock front is then particularly sensitive to the temperature because of the ionization of hydrogen. The increase in radius resulting from a higher surface temperature however has the effect of reducing the infall velocity u_2 and also the infall density ρ_2 (since $\rho \propto r^{-3/2}$), and this tends to moderate the increase in surface temperature resulting from an increase in the density of the infalling cloud. In fact, as we see in Table 7, the surface temperature T_1 is confined by this effect to a relatively small range of variation near 10^4 °K.

Thus we see that the radius, surface temperature, and luminosity of the core as listed in Table 7 can be understood as being determined primarily by the density of the infalling protostellar cloud; all of these quantitites generally increase with increasing density of the cloud. The most important result at this stage is the core radius, since it turns out that the radius of the star finally resulting at the end of the collapse is not very different from the radius of the stellar core at the time of maximum surface temperature and luminosity as listed in Table 7. Consequently it is of some interest to see if a simple argument can be found to predict approximately the core radius, given the initial density or equivalently the radius of the protostellar cloud.

If we assume that the core radius R always adjusts itself so as to maintain the surface temperature T_1 at exactly 10^4 °K, we can roughly reproduce the values of $R/R_\odot$ in Table 7 from the following simple calculation. We assume that at this late stage in the collapse the density distribution throughout the whole infalling cloud has approximately the form

$$\rho = ar^{-3/2} \quad . \tag{9.9}$$

The constant a can be related to the mass M_p and the radius R_p of the protostellar cloud by integrating eqn. (9.9) over the volume of the cloud to get the mass; the resulting expression for a is

$$a = \frac{3M_p}{8\pi R_p^{3/2}} \quad . \tag{9.10}$$

If we now put $\rho_2 = aR^{-3/2}$ and combine this with equations (9.7) and (9.8), we can derive the following expression for the core radius R:

$$R = \left[\frac{3M_p(2\,GM)^{3/2}}{16\pi R_p^{3/2}\sigma T_1^{\,4}}\right]^{1/3} \quad . \tag{9.11}$$

If we assume $M_p = M = 0.5\ M_\odot$ and $T_1 = 10^4\ {}^oK$, this gives

$$R \simeq 5.5 \times 10^{19} R_p^{-1/2} \quad (R,\ R_p \text{ in cm}) \ . \tag{9.12}$$

Substituting the values of R_p tabulated in Table 2, we obtain the following comparison with the results in Table 7:

Case No.	R_p (cm)	$R/R_\odot$ (eqn. 9.12)	$R/R_\odot$ (Table 7)
1	1.63×10^{17}	2.0	2.6
2	1.63×10^{16}	6.2	6.2
3	1.63×10^{16}	6.2	6.7
4	1.63×10^{17}	2.0	2.7
5	9.06×10^{16}	2.6	3.4

9.5 Final Stages of the Collapse

After the stage of evolution represented by Table 7, the evolution of the core in Case 7 ($M = 5M_\odot$) begins to differ substantially from the other cases. We shall therefore describe first Cases 1 - 6, in which the final stages of the evolution are qualitatively essentially the same, and we shall leave the description of Case 7 to section 9.7.

As the point of maximum surface temperature is passed, the specific entropy of the material entering the core just inside the shock front stops increasing and begins to decrease. Consequently, in those cases where the core radius was increasing prior to the point of maximum surface temperature, the radius stops increasing and begins to decrease; in the other cases, including Case 1, the radius simply continues to decrease slowly. At the same time, because of the decreasing entropy of the incoming material, the entropy gradient in the outer part of the core becomes negative, and a convective zone arises near the surface and grows inward as the evolution proceeds. As was the case at an earlier stage of the collapse, the convection zone transports energy from the inner to the outer part of the core and thus prevents the core radius from decreasing as rapidly as would otherwise be the case. In fact it turns out that the radius decreases only slightly during the final phase of the collapse; this is evident in the HR diagrams in Figs. 5 - 10 (pp. 126 - 136), where in each case after the point of maximum surface temperature and luminosity is passed the surface temperature and luminosity of the core decrease substantially while the radius remains nearly constant. In Case 1, for example (Fig. 5), this phase is represented by the section of the curve between about 10^5 and 10^6 years after the formation of the core.

As the core surface temperature decreases, due to the decreasing kinetic energy inflow rate, the opacity in the surface layers of the core also decreases and radiative energy transfer becomes more and more important. Consequently there develops outside the convection zone a thin radiative surface region, in which the temperature is nearly isothermal. (In a few cases, including Case 1, a thin nearly isothermal surface layer has in fact been in existence since a much earlier stage in the evolution.) The radiative flux in this thin radiative surface layer is still small compared with the total luminosity emitted from the shock front, which still is supplied mainly from the kinetic energy inflow, but it is larger than the mechanical energy flux just inside the shock front, so this region is essentially in radiative equilibrium.

As the collapse proceeds, the kinetic energy inflow to the shock front continues to decrease because of the decreasing density of the infalling material, while at the same time the convective plus radiative energy outflow from the interior of the core increases because of the decreasing opacity in the surface layers of the core. Eventually, after practically all of the protostellar mass has fallen into the core, a point is reached where the rate of energy outflow from the interior of the core becomes greater than the rate of kinetic energy inflow to the shock front; thereafter the luminosity radiated from the surface of the core comes mainly from the interior of the core and no longer primarily from the kinetic energy inflow. Finally, when all of the protostellar mass has fallen into the stellar core, all effects of the infall of material become negligible, the stellar core becomes essentially an ordinary star, and the surface layer of the core becomes essentially an ordinary stellar atmosphere. The shock front remains in existence, but the mass flow through it becomes negligible and it no longer has any important effect on any of the properties of the star or its atmosphere.

At this time the convection zone occupies in all cases approximately the outer half of the mass and the outer half of the radius of the core. As was mentioned earlier, the structure of the outer convective part of the core and the core radius are not greatly affected by the central region of lower specific entropy which remains nonconvective; thus at least as far as the outer part of the core is concerned, the structure is not very different from that of a completely convective star. Thus the star finally resulting at the end of the collapse is essentially not very different from a conventional completely convective Hayashi pre-main sequence model, and its position in the HR diagram falls quite close to the conventional "Hayashi track" for the convective phase of pre-main sequence contraction (Hayashi et al., 1962). In the HR diagrams plotted in Figs. 5 - 10 the Hayashi phase is represented by the section of the evolutionary path where the curve turns downward and becomes almost vertical near $\log T_e \simeq 3.64$; in Case 1 (Fig. 5), for example, this is the final section of the curve between 10^6 and 3×10^6 years. In most cases the calculations were stopped soon after the star came onto the Hayashi track because of numerical difficulties encountered at this point and also because this phase of the pre-main sequence evolution has already been studied in more detail by previous authors (see for example Ezer and Cameron 1963, 1965; Iben 1965; Bodenheimer 1965, 1966a, 1966b). It is gratifying to note that despite our relatively very crude numerical treatment, our results for the Hayashi track are in good agreement with the results of these previous authors, the differences being no greater than the effects of possible uncertainties in the conventional mixing length theory of convection.

Some of the important properties of the resulting star at the time when infall effects become negligible and the star first appears on the Hayashi track are listed for the various cases in Table 8 (p. 116); at the time represented by this table the kinetic energy inflow accounts for only about 1 or 2% of the total luminosity radiated from the surface of the star. We note in Table 8 that the time required after the formation of the stellar core for all of the protostellar

TABLE 8

PROPERTIES OF THE CORE WHEN INFALL EFFECTS HAVE BECOME NEGLIGIBLE

Case No.	t (yrs)	$M/M_\odot$	$R/R_\odot$	$L/L_\odot$	T_1 (^oK)	ρ_1 (gm/cm^3)	u_2 (cm/sec)	ρ_2 (gm/cm^3)
1	1.1 + 6	1.00	2.0	1.3	4400	3.1 - 7	5.0 + 7	3. - 15
2	3.3 + 4	1.00	5.1	7.7	4300	1.1 - 7	3.1 + 7	4. - 14
3	2.8 + 4	1.00	5.7	9.2	4200	1.0 - 7	3.0 + 7	3. - 14
4	1.1 + 6	1.00	2.0	1.3	4400	3.1 - 7	5.0 + 7	3. - 15
5	4.5 + 5	1.00	2.5	2.0	4400	2.5 - 7	4.5 + 7	6. - 15
6	2.0 + 5	2.00	5.0	13.	4900	9.8 - 8	4.4 + 7	1. - 14
7	1.1 + 5	5.00	7.0	1300	13000	5.5 - 10	5.9 + 7	2. - 13

material to fall into the core and for infall effects to become negligible is approximately 5 times the initial free fall time of the cloud as listed in Table 5 (p. 63). The final surface temperature as listed in Table 8 for Cases 1 - 5 is about 4400 ^{o}K, in good agreement with previous determinations of the Hayashi track for one solar mass. The final radius is almost the same as the radius of the core at the time of maximum surface temperature and luminosity as listed in Table 7 (p. 108), being typically only about 20% smaller; thus the radius of the resulting star when it first comes onto the Hayashi track is determined by essentially the same considerations which determine the radius of the stellar core at the time of maximum surface temperature and luminosity, as discussed in section 9.4. We conclude that, at least within the various assumptions and approximations which we have employed, the radius and luminosity of the resulting star when it first appears on the Hayashi track are determined primarily by the assumed initial density or equivalently by the radius of the protostellar cloud; other factors, such as the initial temperature, opacity, or composition of the cloud are relatively unimportant (except insofar as they may affect the initial density of the cloud).

It is of some interest to note in Table 8 that a star of one solar mass first appears rather low on the Hayashi track, with a radius and luminosity which are much smaller than has previously been thought to be the case for the early stages of pre-main sequence contraction. For example, the calculations of Ezer and Cameron (1965) indicate a maximum possible radius for a contracting star of one solar mass of about 60 $R_\odot$, and a corresponding maximum luminosity of about 600 $L_\odot$; in contrast, our results for the "standard" Case 1 show that a star of one solar mass first appears on the Hayashi track with a radius of only 2 $R_\odot$ and a luminosity of only 1.3 $L_\odot$. The radius and luminosity are larger in Cases 2 and 3, but not very much so, being still only about 5 $R_\odot$ and 8 $L_\odot$ respectively; in any case, Cases 2 and 3 are thought to be less realistic than Case 1, so these latter values may perhaps be considered as upper limits. We conclude that a star of one solar mass first appears on the Hayashi track with a radius of only a few solar radii and a luminosity of only a few solar luminosities. This result is not very much affected even by rather large changes in the assumed conditions for the collapse of a protostar.

Of course, it must be kept in mind that all of our conclusions are subject to the rather restrictive set of assumptions discussed in Part I and summarized on page 31. The most important of these assumptions is the assumption of strict spherical symmetry throughout the collapse, since this excludes the probably important effects of rotation. What the effect of rotation would be in detail one cannot say without actually doing the calculations. However, it would seem likely that rotation would tend to reduce the infall velocity u_2, at least in a direction perpendicular to the axis of rotation; the resulting reduction in the mass inflow rate would tend to reduce the surface temperature, luminosity, and radius of the stellar core, so that the resulting star would appear even lower on the Hayashi track than was found in our calculations. Because the infall velocity along the axis of rotation is not reduced, and because as we have found the radius of the resulting star is not very sensitive to large changes in the conditions of the collapse, there is a possibility that our results might not be drastically altered by the existence of rotation; however this is merely speculation and further calculations would be required to decide the matter.

9.6 Contraction Toward the Main Sequence

Although the star resulting at the end of the collapse is outwardly and for most practical purposes very much like a conventional convective pre-main sequence model, the conditions in a small region near the center are actually quite different. In all cases except No. 5 the specific entropy is very low right at the center and increases rapidly moving outward from the center, this situation having been preserved from the early stages of the formation of the stellar core because of the unimportance of heat transfer processes in this region. The very low central entropy means that the density right at the center is much higher and the temperature much lower than would be the case with a more normal entropy distribution; as a result, there is a small region near the center in which the density decreases quite rapidly and the temperature actually increases moving outward from the center. This is illustrated for Case 1 in Fig. 12 (p. 140), which shows the variation of log T with log ρ in the star at the time when it first comes onto the Hayashi track. The peak temperature in this model occurs at about 5% of the mass and 15% of the radius outward from the center.

Because of the very low central entropy and the large positive entropy gradient near the center, in no case does the outer convection zone ever extend all the way to the center of the star as the star contracts toward the main sequence. In some cases, including Case 1, the star in any case comes onto the Hayashi track with such a small radius and such high interior temperatures that radiative energy transfer is already becoming important in the region of high temperature near the center, producing a region in radiative equilibrium which grows outward as the evolution proceeds. Thus in Case 1 for example the outer convective region reaches its maximum extent of about the outer 57% of the mass and the outer 56% of the radius just when the star comes onto the Hayashi track, and it subsequently retreats again toward the surface. In Cases 2 and 3 radiative energy transfer is not yet important when the star first appears on the Hayashi track, and the convection zone continues to expand inward as the star evolves down the Hayashi track, reaching a maximum extent of approximately the outer 97 - 98% of the mass and 85 - 90% of the radius before radiative transfer becomes important. In these cases the convection zone never reaches all the way to the center because of the very low specific entropy at the center. The persisting small low entropy region at the center however has negligible effect on the structure of the outer part of the star or on the position of the Hayashi track, as is verified by comparison of the results in different cases in which this central low entropy region is of different extent.

The small central region of low specific entropy and inverted temperature gradient finally disappears when the temperature becomes high enough for inward radiative energy transfer to heat up the material right at the center and eradicate the temperature minimum at the center, thus establishing radiative equilibrium throughout the central part of the star. This is expected to happen in all cases before the star gets near the main sequence and nuclear energy generation starts to become important. In Cases 1 - 5 the calculations were not followed through this phase because of numerical difficulties encountered in connection with our method of treating convection; however, in Case 6 ($M = 2\ M_{\odot}$) these difficulties were less severe and it was possible to follow the evolution through almost to the main sequence (see Fig. 10, p. 136). We briefly describe below the results of these calculations.

In Case 6 the star comes in almost at the bottom of the Hayashi track, and at its maximum extent the outer convection zone covers only about 32% of the mass and 45% of the radius; thereafter the convection zone retreats toward the surface again. Shortly after the star comes onto the Hayashi track a minimum luminosity of about $9\ L_{\odot}$ is reached; the luminosity then begins to increase again and the convection zone shrinks and becomes unimportant for the overall structure of the star. At the same time radiative energy transfer begins to heat up the low entropy material at the center, and the central region of low entropy and inverted temperature gradient shrinks. By the time the surface temperature has reached about 6000 °K, which is well before the main sequence is reached, the temperature minimum at the center has disappeared entirely and radiative equilibrium has been established throughout almost the whole star. The outer convection zone is by this time insignificant in extent, occupying only about 1% of the radius near the surface. The subsequent evolution of the star consists of slow radiative cooling and contraction with increasing luminosity, as has been well studied previously.

The shape of the evolutionary path in Fig. 10 differs somewhat from a calculation for the same mass by Bodenheimer (1966b), but this should probably not be taken seriously because of our relatively very crude treatment of convection. Also, our luminosity is higher than Bodenheimer's, but this is probably attributable to the higher helium content used in our calculations. In all, there appears to be no reason to suppose that the existence of the small central region of low entropy and inverted temperature gradient has made any significant difference to the evolution of the star after its arrival on the Hayashi track.

9.7 Final Stages in Case 7 ($M = 5\ M_{\odot}$)

In Case 7 the core mass is higher than in the other cases, and consequently the interior temperatures in the core are also higher; as a result, radiative energy transport in the interior of the core becomes important at a much earlier stage in the collapse than in the other cases. In fact, radiative energy transfer is already becoming important near the center of the core at the time of maximum surface temperature and luminosity as listed in Table 7. After this point is passed, the core radius does not decrease as in the other cases but continues to increase because of the outward transport of energy by radiation in the core, which increases the entropy of the outer part of the core at the expense of the inner part. As in the other cases, a convective zone appears near the surface of the core, but it never becomes as extensive as in the other cases, reaching a maximum extent of only about 5% of the mass and 25% of the radius at a surface temperature slightly below 10^4 °K. Subsequently the convective region retreats again toward the surface as the inner radiative region grows and the outer layers of the core heat up and begin to come into radiative equilibrium.

Because of the small mass in the outer layers of the core, the time scale for radiative relaxation becomes shorter and shorter as layers closer and closer to the surface come into radiative equilibrium. Thus the surface layers come into radiative equilibrium almost instantaneously at about 2.3×10^4 years after the formation of the core, at which time the surface temperature reaches a minimum value of about 6900 °K (see Fig. 11, p. 138). At this point the mass of the core is $3.7\ M_\odot$ and the radius is $17.4\ R_\odot$. The outer convection zone is no longer important, and occupies only about 1% of the radius near the surface.

The radius of the core reaches a maximum value of $21\ R_\odot$ when the mass is $4.0\ M_\odot$. At this time the fraction of the total core luminosity contributed by the kinetic energy inflow drops to less than 50%, and the properties of the outer layers of the core become determined primarily by the radiative energy outflow from the interior and no longer by the kinetic energy inflow. Thus the infall of material no longer has any important effect on the structure or evolution of the core, even though only 4/5 of the total mass has as yet fallen into the core. The subsequent evolution of the core consists of a slow radiative cooling and contraction which is essentially the same as the radiative phase of pre-main sequence contraction, as has previously been well studied. The effects of the infalling material finally become completely negligible when all of the mass has fallen into the core; the properties of the core at this time are as listed in Table 8. At this time the central region of low entropy and inverted temperature gradient has not yet disappeared completely, but it has shrunk to a negligible extent of about 0.2% of the mass and 2% of the radius.

It is noteworthy that in Case 7 there is no convective "Hayashi" phase of pre-main sequence evolution at all; by the time that the effects of the infall of material have become unimportant, the star is already closer to the main sequence than the bottom of the Hayashi track. We note that in Case 6 ($M = 2M_{\odot}$) the star came in almost at the bottom of the Hayashi track; in fact, if this case had been calculated with the same assumptions as Case 1 the radius of the resulting star would have been smaller due to the lower density of the protostellar cloud, and the Hayashi phase would have been even shorter and might not even have existed at all. Thus it appears that the convective Hayashi phase of pre-main sequence evolution does not exist at all for masses much greater than about 2 $M_\odot$. For higher masses, the radius of the stellar core never becomes large enough for a convective phase to be important, and the core comes into radiative equilibrium and begins to follow the radiative pre-main sequence contraction track before the infall of material has completely stopped.

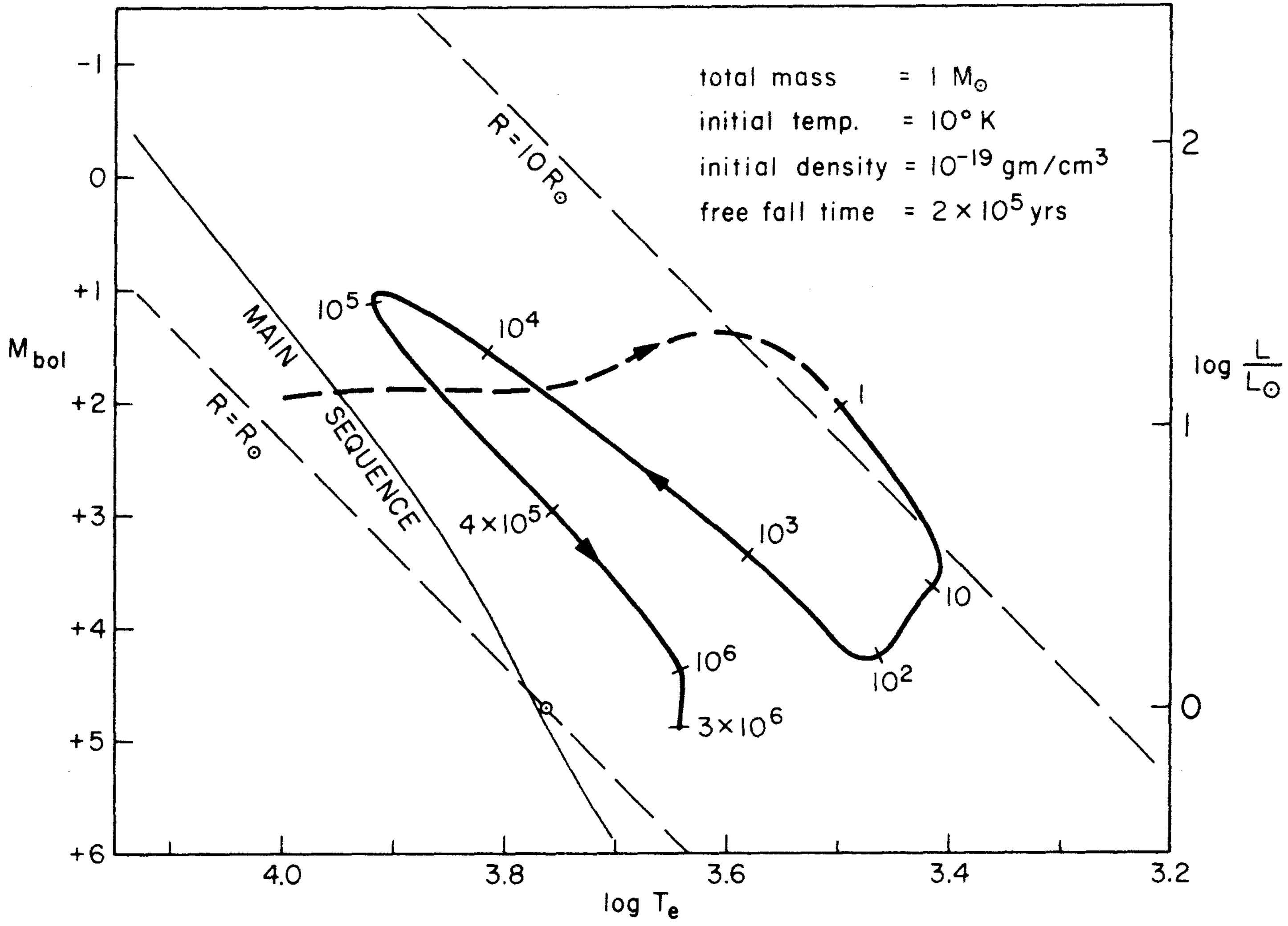
total mass = 1 $M_\odot$
initial temp. = 10° K
initial density = 10^{-19} gm/cm^3
free fall time = 2×10^5 yrs
R=10$R_\odot$
R=$R_\odot$
MAIN SEQUENCE
M_{bol}
-1
0
+1
+2
+3
+4
+5
+6
log $\frac{L}{L_\odot}$
2
1
0
log T_e
4.0
3.8
3.6
3.4
3.2
1
10
10^2
10^3
10^4
10^5
4×10^5
10^6
3×10^6

FIGURE 5

Fig. 5 (p. 126): The evolution of the stellar core in an HR diagram for the "standard" Case 1. The times in years after the formation of the stellar core are marked along the evolutionary path. The dashed section of the curve represents the initial adiabatic phase (section 9.2) when the luminosity emitted from the surface of the core is totally reabsorbed in the infalling material and never escapes from the protostellar cloud. The initial point of this dashed curve is somewhat uncertain. The beginning of the solid curve represents the point where about 90% of the luminosity emitted from the core is transmitted outward through the whole protostellar cloud. See text, sections 9.3 - 9.5, for explanation of the solid curve.

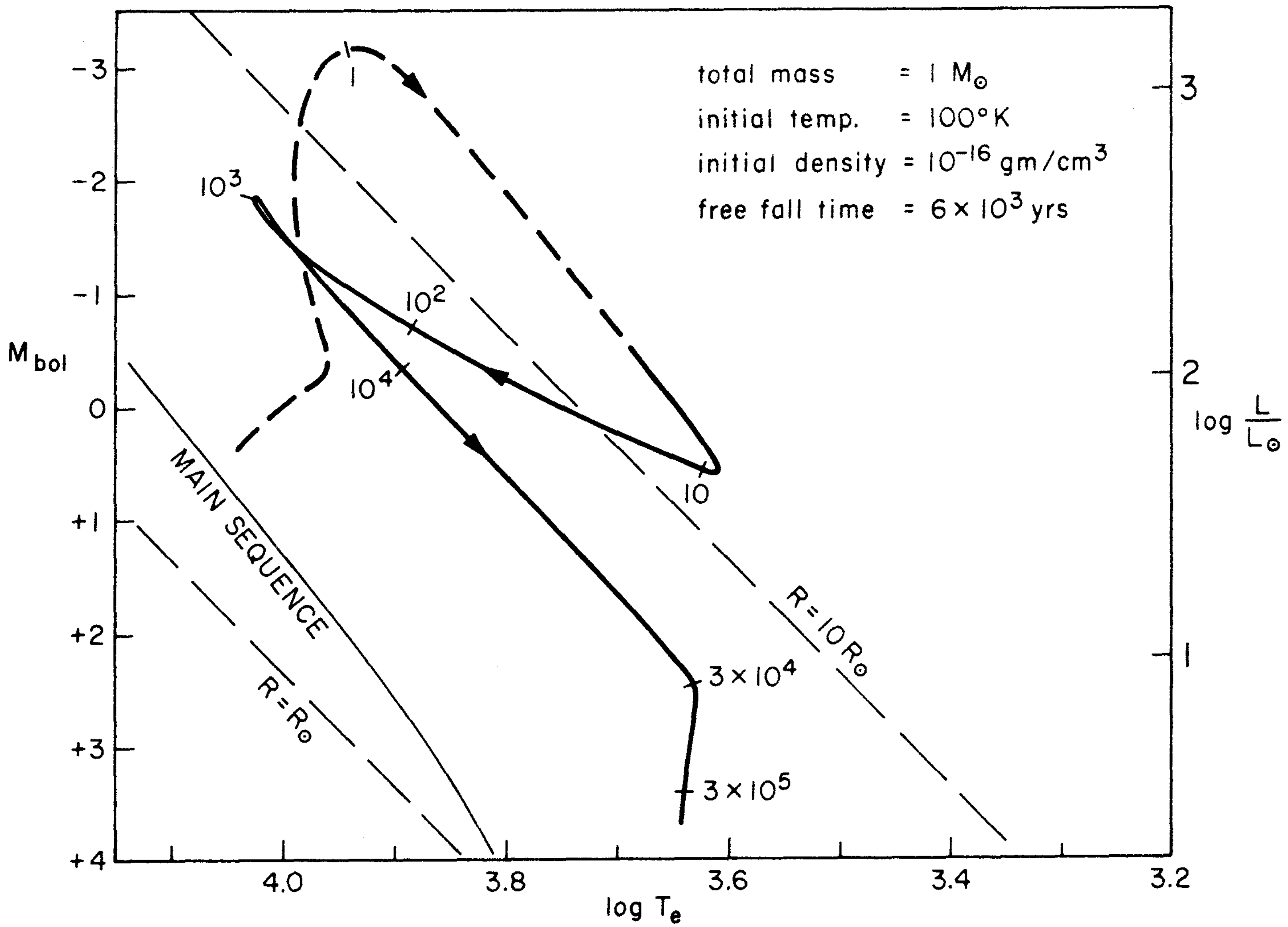
total mass = 1 $M_\odot$
initial temp. = 100°K
initial density = 10^{-16} gm/cm^3
free fall time = 6×10^3 yrs
M_{bol}
−3
−2
−1
0
+1
+2
+3
+4
log $\frac{L}{L_\odot}$
3
2
1
log T_e
4.0
3.8
3.6
3.4
3.2
1
10
10^2
10^3
10^4
3×10^4
3×10^5
R = 10 $R_\odot$
R = $R_\odot$
MAIN SEQUENCE

FIGURE 6

Fig. 6 (p. 128): The evolution of the stellar core in an HR diagram for Case 2. Explanation is the same as for Fig. 5 (see p. 127).

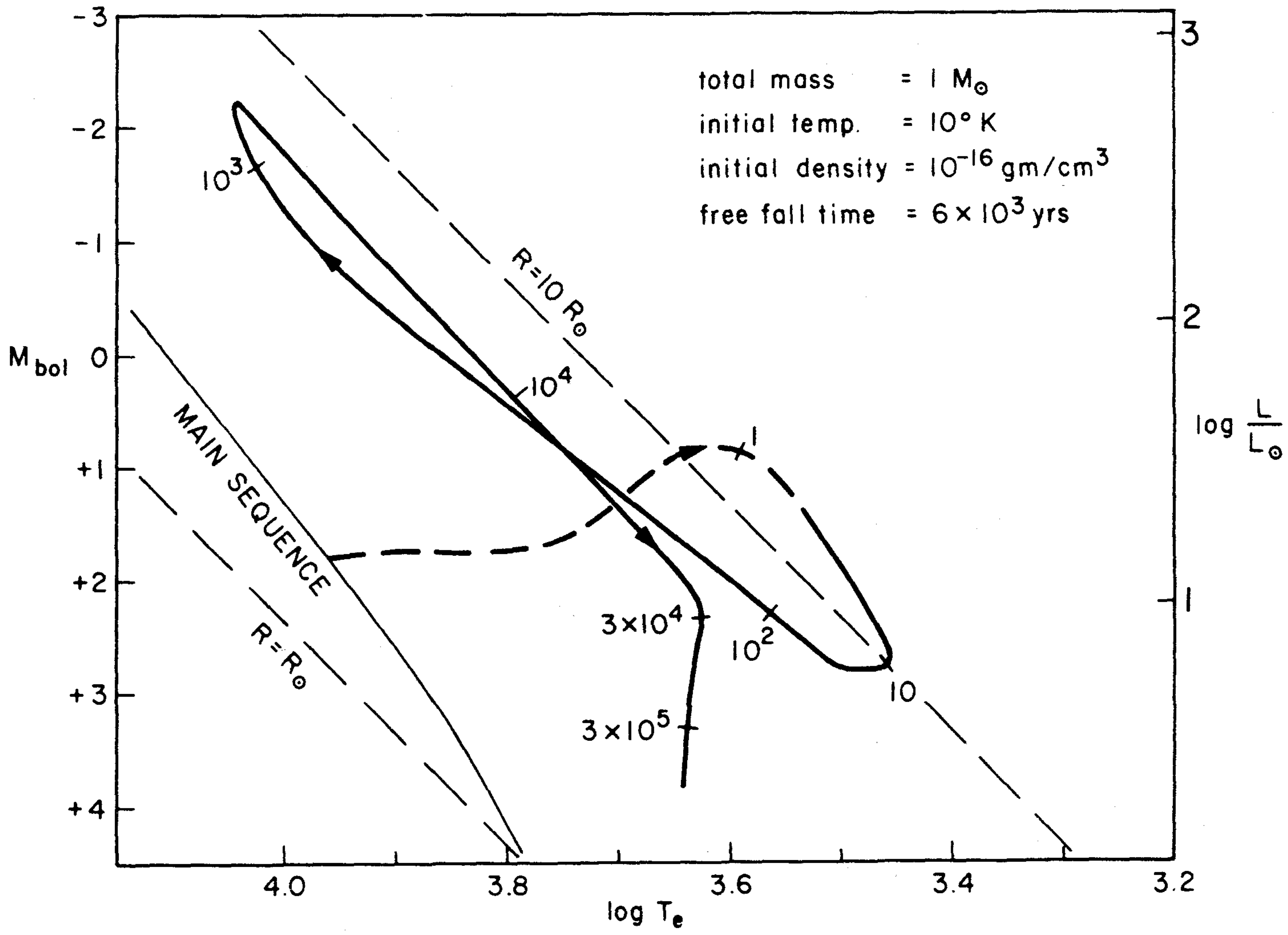
total mass = 1 $M_\odot$
initial temp. = 10° K
initial density = 10^{-16} gm/cm^3
free fall time = 6×10^3 yrs
M_{bol}
-3
-2
-1
0
+1
+2
+3
+4
log $\frac{L}{L_\odot}$
3
2
1
4.0
3.8
3.6
3.4
3.2
log T_e
$R=10 R_\odot$
$R=R_\odot$
MAIN SEQUENCE
10^3
10^4
1
10
10^2
3×10^4
3×10^5

FIGURE 7

Fig. 7 (p. 130): The evolution of the stellar core in an HR diagram for Case 3. Explanation is the same as for Fig. 5 (see p. 127).

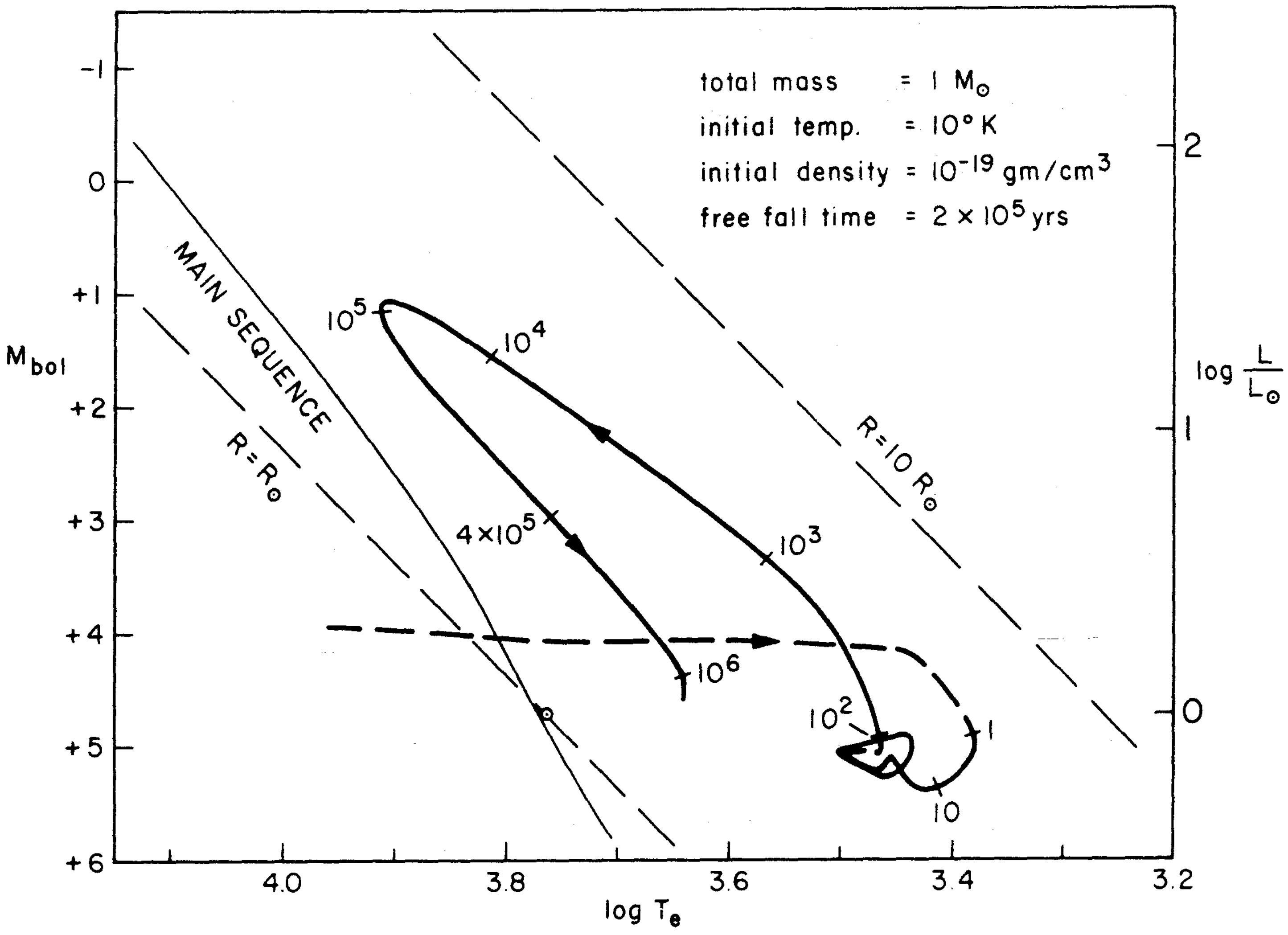
total mass = 1 $M_\odot$
initial temp. = 10° K
initial density = 10^{-19} gm/cm^3
free fall time = 2×10^5 yrs
M_{bol}
-1
0
+1
+2
+3
+4
+5
+6
$\log \frac{L}{L_\odot}$
2
1
0
4.0
3.8
3.6
3.4
3.2
$\log T_e$
MAIN SEQUENCE
$R = R_\odot$
$R = 10\ R_\odot$
10^5
10^4
10^3
10^2
10
1
4×10^5
10^6

FIGURE 8

Fig. 8 (p. 132): The evolution of the stellar core in an HR diagram for Case 4. Explanation is the same as for Fig. 5 (see p. 127). The strange phenomenon near $M_{bol} = +5$, $\log T_e = 3.45$ is the result of a brief dynamical collapse at the center of the stellar core which occurred in the calculations when pressure ionization reduced γ below 4/3 at the center. The resulting complicated dynamical motions in the core were not of very large amplitude and were artificially suppressed in order to be able to continue the calculations on the accretion time scale, which is many orders of magnitude longer than the dynamical time scale. This phenomenon was not mentioned in the text because (a) it does not appear to be of any importance for the subsequent evolution of the core and (b) our equation of state is incorrect at high densitites, as mentioned in Appendix C, and it is uncertain whether pressure ionization would in reality produce such an effect.

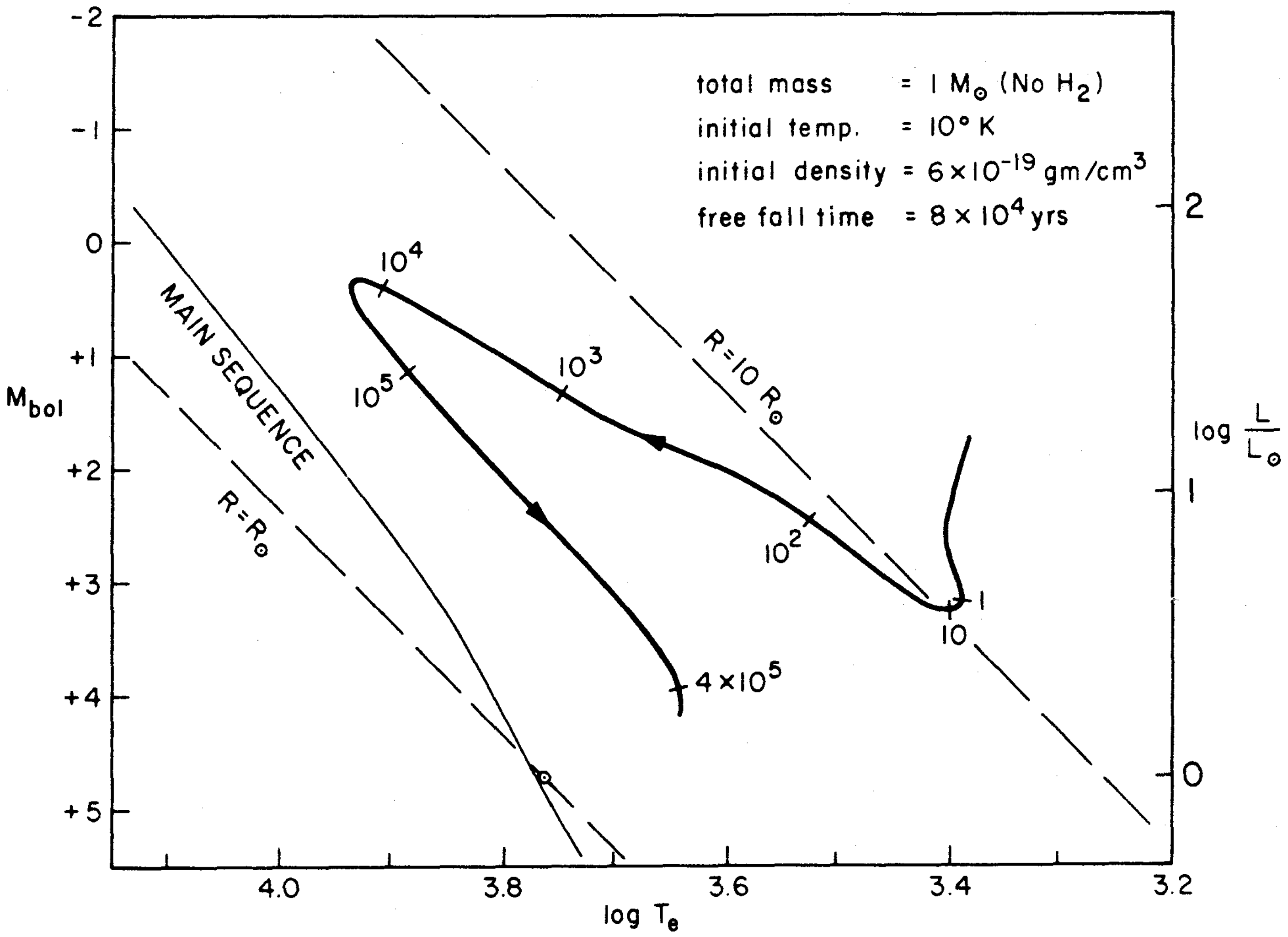
total mass = 1 $M_\odot$ (No H_2)
initial temp. = 10° K
initial density = 6×10^{-19} gm/cm^3
free fall time = 8×10^4 yrs
M_{bol}
-2
-1
0
+1
+2
+3
+4
+5
log $\frac{L}{L_\odot}$
2
1
0
4.0
3.8
3.6
3.4
3.2
log T_e
MAIN SEQUENCE
$R = R_\odot$
$R = 10\ R_\odot$
1
10
10^2
10^3
10^4
10^5
4×10^5
$\odot$

FIGURE 9

Fig. 9 (p. 134): The evolution of the stellar core in an HR diagram for Case 5 (no H_2). In this case the initial adiabatic phase has not been plotted because it is quite short and because the method of calculation used for this phase (sections A.4 and A.5) does not allow accurate positioning of the core in an HR diagram.

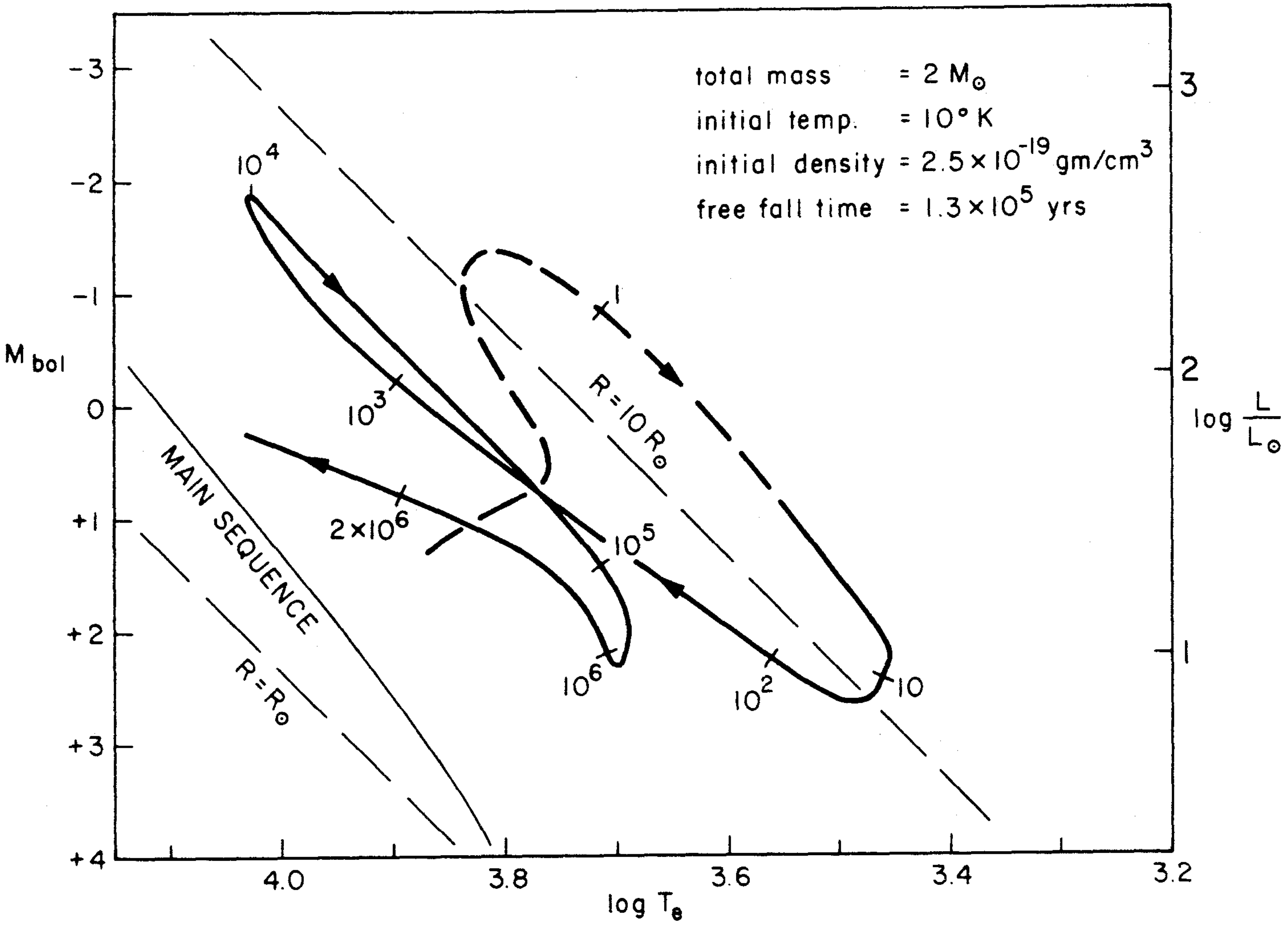
total mass = 2 M⊙
initial temp. = 10° K
initial density = 2.5 × 10⁻¹⁹ gm/cm³
free fall time = 1.3 × 10⁵ yrs
M bol
-3
-2
-1
0
+1
+2
+3
+4
log L/L⊙
3
2
1
log Te
4.0
3.8
3.6
3.4
3.2
10⁴
10³
2×10⁶
10⁵
10⁶
10²
10
1
R=10R⊙
MAIN SEQUENCE
R=R⊙

FIGURE 10

Fig. 10 (p. 136): The evolution of the stellar core in an HR diagram for Case 6 ($M = 2M_{\odot}$). Explanation is the same as for Fig. 5 (see p. 127). See section 9.6 for the explanation of the final section of the evolutionary parth from about 10^6 years onward.

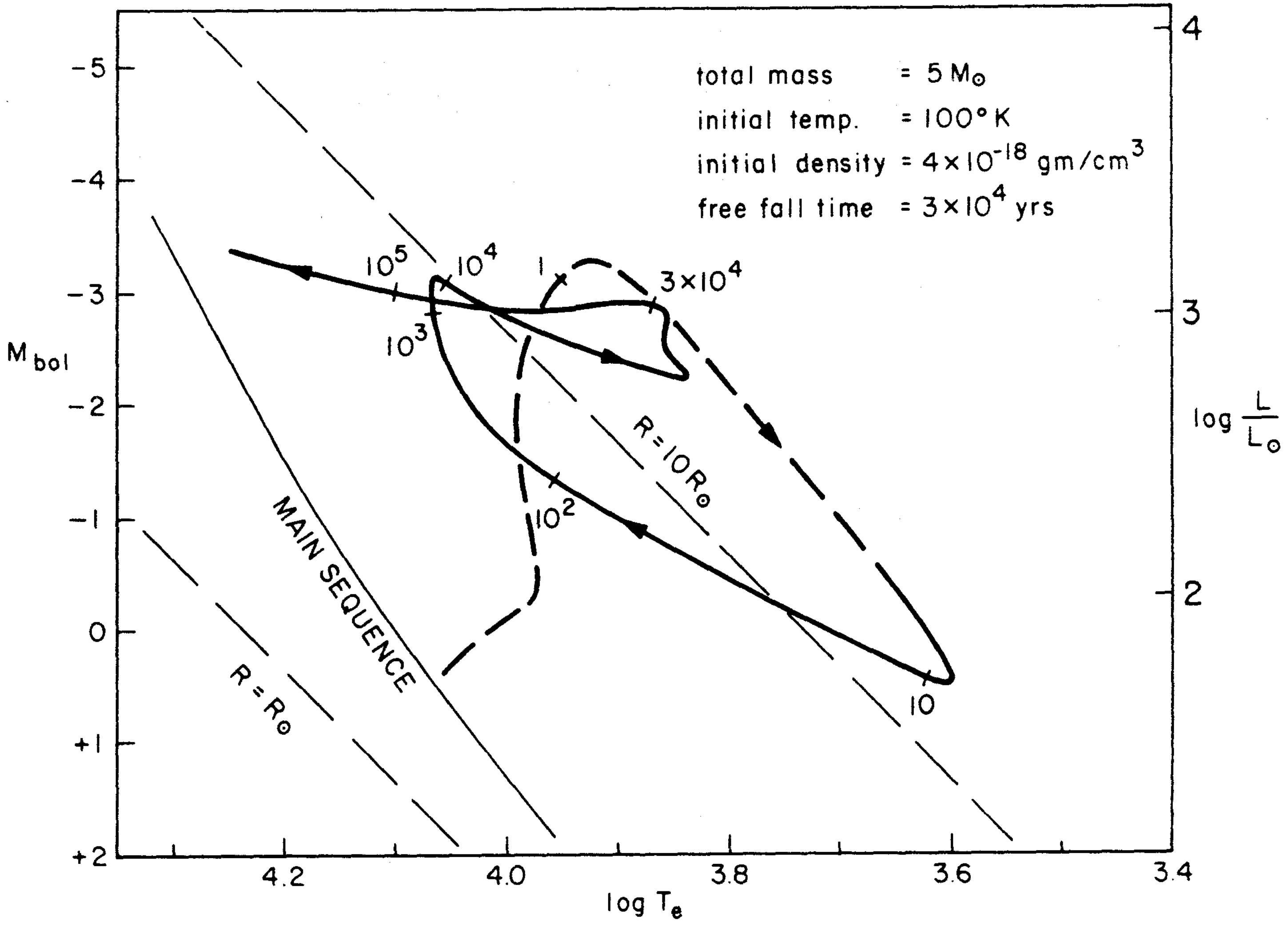
total mass = 5 $M_\odot$
initial temp. = 100° K
initial density = 4×10^{-18} gm/cm^3
free fall time = 3×10^4 yrs
10^5
10^4
1
3×10^4
10^3
10^2
10
R = 10 $R_\odot$
MAIN SEQUENCE
R = $R_\odot$
M_{bol}
-5
-4
-3
-2
-1
0
+1
+2
4.2
4.0
3.8
3.6
3.4
log T_e
4
3
2
log $\frac{L}{L_\odot}$

FIGURE 11

Fig. 11 (p. 138): The evolution of the stellar core in an HR diagram for Case 7 ($M = 7M_{\odot}$). Explanation of the curve up to about 10^3 years is the same as for Fig. 5 (see p. 127). Note that this section of the curve is very similar to Case 2 (Fig. 6, p. 128), for essentially the reason explained at the end of section 7.3 (p. 53). See section 9.7 for explanation of the later phases of the evolution.

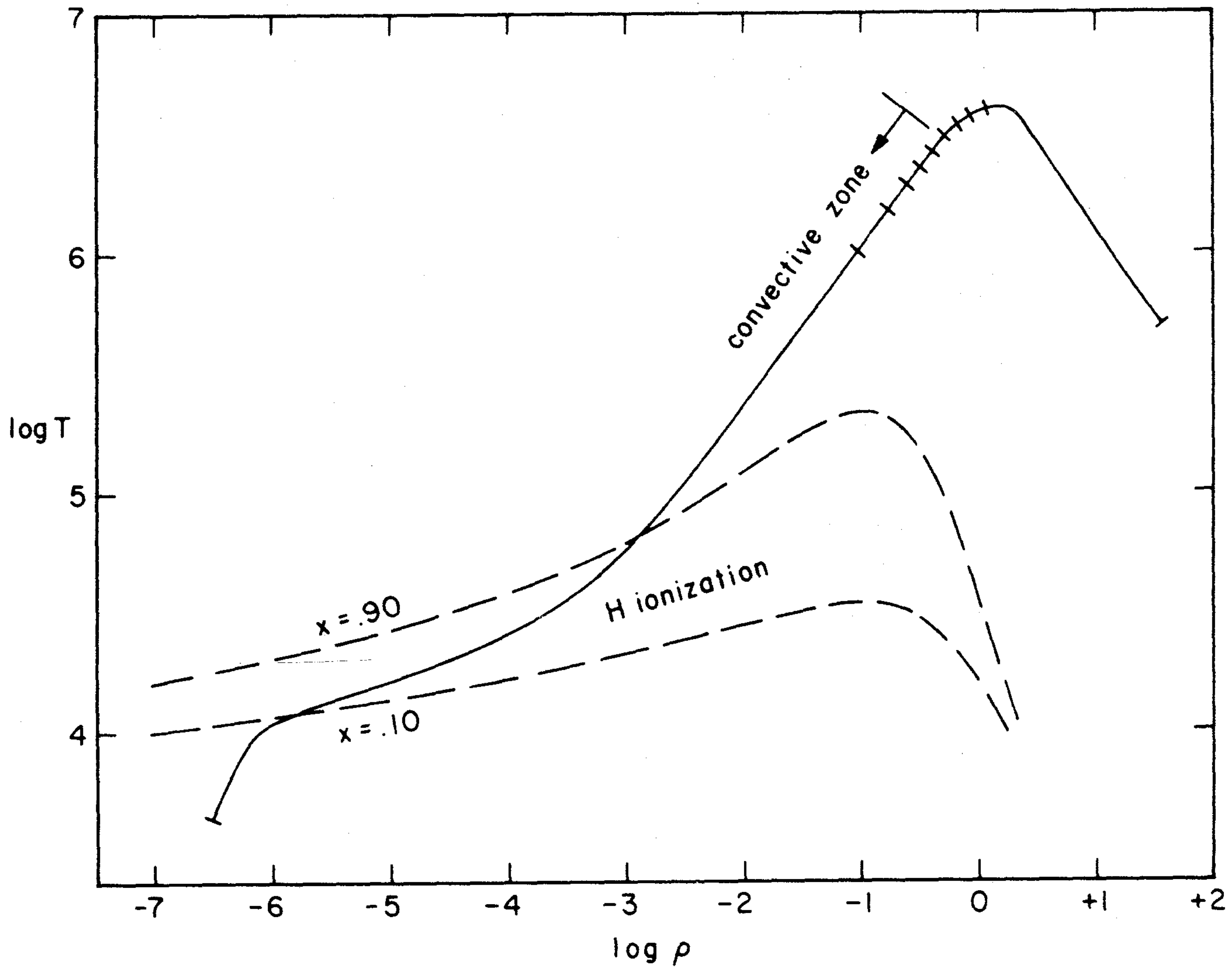

log T
7
6
5
4
log ρ
-7
-6
-5
-4
-3
-2
-1
0
+1
+2
convective zone
H ionization
x = .90
x = .10

FIGURE 12

Fig. 12 (p. 140): The variation of log T vs. log ρ for the interior of the resulting star in Case 1 at the time represented by Table 8 (p. 116), i.e. at the time when it first appears on the Hayashi track. The ticks along the curve divide the star into ten zones of equal mass. The dashed curves are lines of constant degree of ionization x and are explained in Appendix C. See section 9.6 for further explanation of this diagram.

PART III. OBSERVATIONAL APPEARANCE OF A COLLAPSING PROTOSTAR

10. THE EMITTED SPECTRUM OF A COLLAPSING PROTOSTAR

10.1 General Considerations

It was mentioned in section 9 that until practically all of the protostellar mass has fallen into the stellar core, the core remains heavily obscured by the dust in the infalling cloud. The radiation emitted from the core is completely absorbed by the dust grains, and the energy is re-emitted thermally at the infrared wavelengths corresponding to the temperature of the grains. The luminosity emitted from the core is transported outward through the protostellar cloud with negligible diminution, since the energy lost in heating the infalling material is negligible compared with the total radiative energy flux; thus the total bolometric luminosity emitted from the cloud is the same as the luminosity of the core, and can be considered as known from the results for the evolution of the core described in section 9. The wavelength distribution of the radiation however becomes shifted to longer and longer wavelengths as the radiation is transported outward through the cloud, since the temperature of the dust grains decreases with increasing distance from the core. Thus the calculation of the emitted spectrum involves a consideration of the radiation transfer problem and the temperature distribution in the infalling cloud.

Before describing the simple approximations which we have used for the radiation transfer problem, we point out that it is easy to see qualitatively what kind of results may be expected. The emitted spectrum may be expected to be qualitatively something like a blackbody spectrum corresponding approximately to the temperature of the dust grains at the point in the cloud where the optical depth at the relevant infrared wavelengths is equal to unity. Initially the density of the infalling material is so high that optical depth unity occurs far out in the cloud where the temperature is quite low (less than 100 ^{o}K); thus most of the radiation is emitted at far infrared wavelengths. As the collapse proceeds, the density of the infalling material decreases, and the point of optical depth unity moves inward to smaller radii and higher temperatures; consequently the emitted spectrum is shifted to shorter and shorter wavelengths. This continues until the density of the infalling material becomes so low that the cloud is no longer completely optically thick, and the spectrum of the central stellar object begins to show through.

10.2 Calculation of the Emitted Spectrum

During most of the collapse, the total optical depth of the infalling protostellar cloud is so large that for purposes of calculating the emitted spectrum the cloud can be considered as extending inward to zero radius and infinite optical depth. Also, the cloud extends outward to such large radii and small optical depths that it can for the present purposes be considered as extending to infinite radius and zero optical depth. We assume for the moment that the temperature distribution in the cloud is known, and we assume that the dust grains radiate isotropically in accordance with Kirchhoff's law. (This of course neglects the possibility of scattering, which is a good approximation at far infrared wavelengths but may not be so good at visual or near infrared wavelengths.) We then have the problem of calculating the total emergent radiation at each wavelength by integrating up the contributions from all parts of the cloud, with an attenuation factor of the form $e^{-\tau}$ for each volume element and each line of sight.

In the case of a normal plane-parallel stellar atmosphere this calculation is a simple one and the result can be written

$$L_\lambda = 8\pi^2 R^2 \int_0^\infty E_2(\tau_\lambda) B_\lambda(\tau_\lambda)\, d\tau_\lambda \qquad (10.1)$$

where L_λ is the total luminosity emitted per unit wavelength interval, R is the radius of the star, τ_λ is the radial optical depth at wavelength λ, $E_2(\tau_\lambda)$ is the second exponential integral, and $B_\lambda(\tau_\lambda)$ is the blackbody function (see for example Aller 1963, p. 202). In our case the plane-parallel assumption cannot be used since our "atmosphere" extends over a very large factor in radius, and it is essential to take the spherical geometry into account. The derivation of an expression for L_λ in the spherical case is more involved than in the plane-parallel case, but it is essentially straightforward, and we shall not reproduce it here. After some manipulation of integrals the result can be written in the following form, analogous to equation (10.1):

$$L_\lambda = 16\pi^2 \int_0^\infty r^2(\tau_\lambda) G(\tau_\lambda) B_\lambda(\tau_\lambda)\, d\tau_\lambda \qquad (10.2)$$

where

$$\tau_\lambda = \int_r^\infty \kappa_\lambda \rho \, dr \qquad (10.3)$$

and the function $G(\tau_\lambda)$ is defined by

$$G(\tau_\lambda) \equiv \frac{1}{2r} \int_0^r \frac{s\,ds}{\sqrt{r^2 - s^2}} \left[\exp\left\{ - \int_s^\infty \kappa_\lambda \rho \frac{r\,dr}{\sqrt{r^2 - s^2}} - \int_s^r \kappa_\lambda \rho \frac{r\,dr}{\sqrt{r^2 - s^2}} \right\} + \exp\left\{ - \int_r^\infty \kappa_\lambda \rho \frac{r\,dr}{\sqrt{r^2 - s^2}} \right\} \right] . \qquad (10.4)$$

Clearly the function $G(\tau_\lambda)$ depends on the variation of $\kappa_\lambda \rho$ with r, so that $G(\tau_\lambda)$ is not a "universal function" like $E_2(\tau_\lambda)$.

What little work has been done on radiation transfer in an infinite spherical atmosphere (see for example Chapman 1966) has usually assumed the dependence of $\kappa_\lambda \rho$ on r to be given by an inverse power law of the form

$$\kappa_\lambda \rho(r) = K_\lambda r^{-n} . \qquad (10.5)$$

It happens that a law of this form is applicable amost exactly in our problem. As was explained in section 9.3, the density distribution in the innermost part of the collapsing cloud has the form

$$\rho(r) = \rho_o r^{-n} \qquad (10.6)$$

where $n = 3/2$. It turns out that this law holds with good accuracy over almost the whole region important for the radiation transfer problem. Since the mass absorption coefficient κ_λ for dust grains is independent of ρ, equation (10.5) is applicable to our problem with $n = 3/2$ and $K_\lambda = \kappa_\lambda \rho_o$.

We have defined a new class of functions $G_n(\tau_\lambda)$ as the functions obtained when equation (10.5) is substituted into equation (10.4). These functions have been calculated numerically and tabulated for $n = 3/2$ and $n = 2$ (see Appendix F), and they can for the present purposes be considered as known exactly in numerical form. If equation (10.5) is assumed, the relation between τ_λ and r is readily obtained from equation (10.3); the result is

$$\tau_\lambda = \frac{K_\lambda}{n-1} r^{-n+1} . \tag{10.7}$$

The most interesting case for the present purposes is of course $n = 3/2$, but we shall in the following give the formulas for general n. If we make use of equation (10.7), the luminosity L_λ at wavelength λ as given by equation (10.2) can now be written

$$L_\lambda = 16\pi^2 \left(\frac{K_\lambda}{n-1}\right)^{\left(\frac{2}{n-1}\right)} \int_o^\infty \tau_\lambda^{-\left(\frac{2}{n-1}\right)} G_n(\tau_\lambda) B_\lambda(\tau_\lambda)\, d\tau_\lambda \tag{10.8}$$

where the function $G_n(\tau_\lambda)$ is known. In using equation (10.8) to calculate L_λ by numerical quadrature we have evaluated $G_n(\tau_\lambda)$ either by interpolation or by using the approximate formulas given in Appendix F.

10.3 The Absorption Coefficient of the Dust Grains

In deriving the temperature distribution and in calculating the emitted spectrum of the protostellar cloud, it is necessary to know the wavelength dependence of the absorption coefficient κ_λ of the material. Unfortunately the infrared absorption properties of the dust grains are known very poorly if at all, as was mentioned in section 2.2. In the present circumstances the temperatures of interest are mostly above 150 $^\circ$K, so that according to Gaustad (1963) the grains would consist mainly of $MgSiO_4$. Even if such "mineral grains" of the kind imagined by Gaustad actually exist, however, which is by no means certain, their infrared absorption properties are unknown except for some data of dubious applicability for pure $MgSiO_4$ at wavelengths near 10 μ.

If we assume instead the graphite core-ice mantle model of the dust grains (see Krishna Swamy and O'Dell 1967), then at the higher temperatures the ices would evaporate and the grains would presumably consist mainly of graphite. For graphite the situation is somewhat better, since it is known (Hoyle and Wickramasinghe 1962) that for wavelengths greater than about 1 μ the absorption coefficient of graphite grains varies with wavelength approximately according to $\kappa_\lambda \propto \lambda^{-2}$.

Observationally, there are some data available for the wavelength dependence of the interstellar extinction at near infrared wavelengths (see for example Johnson and Borgmann 1963, Johnson 1965a). For the less pathological cases the variation of absorption coefficient with wavelength implied by these data, while somewhat uncertain and variable from case to case, is roughly approximated by the law $\kappa_\lambda \propto \lambda^{-3/2}$. However, the observational data are not necessarily of any relevance in the present situation, particularly at the higher temperatures, since the main constituents of the interstellar grains may have evaporated at these higher temperatures. In any case, there is no observational information on the interstellar extinction at the longer infrared wavelengths.

In view of this situation we have not attempted any accurate representation of the absorption coefficient κ_λ as a function of wavelength, but have simply adopted a power law of the form

$$\kappa_\lambda = \kappa_0 \lambda^{-p} \tag{10.9}$$

where κ_0 and p are for the moment regarded as arbitrary parameters for which various values may be inserted. By trying different values of κ_0 and p we can at least obtain an idea of how the emitted spectrum depends on the absorption coefficient κ_λ and its variation with wavelength.

10.4 The Temperature Distribution

Before we can use equation (10.8) to calculate the emitted spectrum, we must specify the function $B_\lambda(\tau_\lambda)$, or equivalently the temperature distribution $T(\tau_\lambda)$. Calculating this function accurately would be an involved problem of radiative transfer with spherical symmetry, and would require a detailed solution for the radiation field at each point in the cloud. This problem does not appear to have been solved previously except in very special cases, and we have not attempted to solve it here. Instead we have derived the limiting forms of the temperature distribution $T(\tau_\lambda)$ at small and large optical depths, and we have used these to construct a simple but arbitrary formula for $T(\tau_\lambda)$ which has the correct asymptotic forms in these two limits and provides a smooth transition in between.

We consider first the form of the temperature distribution at very small optical depths, i.e. at very large radii in the collapsing cloud. We suppose for the moment that the radiation field at radius r far out in the cloud can be represented as diluted blackbody radiation of temperature T^* emitted from a surface of radius r^* in the cloud ($r^* << r$). Of course this assumption is not really correct, but it will give the correct form for the dependence of T on τ_λ or r. The undetermined constant in this relation may then be adjusted arbitrarily (as will be explained later) to properly normalize the resulting spectrum. Assuming the dust grains to absorb and re-emit radiation in accordance with Kirchhoff's law, the temperature T at radius r is then determined by the energy balance relation

$$W\int_0^\infty \kappa_\lambda B_\lambda(T^*)\,d\lambda = \int_0^\infty \kappa_\lambda B_\lambda(T)\,d\lambda \tag{10.10}$$

where W is the dilution factor, given by

$$W = \frac{r^{*2}}{4r^2} . \tag{10.11}$$

Substituting $\kappa_\lambda \propto \lambda^{-p}$ into equation (10.10), we obtain

$$T^4 = W^{\frac{4}{4+p}} T^{*4} \qquad (10.12)$$

which, together with equation (10.11), gives the temperature in the outer part of the cloud.

We consider now the inner part of the collapsing cloud where the optical depths are large and the material is quite opaque. In these circumstances the radiative transfer problem simplifies greatly, and we can use the radiation diffusion equation as used in the theory of stellar interiors. This equation can be written

$$L = -\frac{64\pi\sigma r^2 T^3}{3\kappa_R \rho} \frac{dT}{dr} \qquad (10.13)$$

where κ_R is the Rosseland mean opacity. In the present situation the luminosity L is known and is constant throughout the whole cloud. Thus if the dependence of $\kappa_R\rho$ on T and r is specified, equation (10.13) becomes a simple differential equation for T as a function of r, which can be solved with the boundary condition $T = 0$ at $r = \infty$ to give the temperature distribution in the optically thick part of the cloud.

Assuming $\kappa_\lambda = \kappa_o \lambda^{-p}$ and using the definition of Rosseland mean opacity it is possible to derive, after some manipulation of integrals,

$$\kappa_R = \frac{24\zeta(4)}{\Gamma(5-p)\zeta(4-p)} \left(\frac{T}{c_2}\right)^p \kappa_o \qquad (10.14)$$

where ζ is the Riemann zeta function and $c_2 = hc/k$. Since $\kappa_R \propto T^p$

and $\rho \propto r^{-n}$, it is convenient to set

$$\kappa_R \rho = K T^p r^{-n} \tag{10.15}$$

where, from equations (10.14) and (10.6),

$$K = \frac{24\,\zeta(4)}{\Gamma(5-p)\zeta(4-p)c_2^{\,p}} \kappa_o \rho_o \,. \tag{10.16}$$

If we substitute equation (10.15) into equation (10.13), we can now solve the differential equation (10.13) analytically to obtain the temperature distribution in the optically thick part of the cloud. The result can conveniently be written in the form

$$T^4 = \frac{3(n + p/2 - 1)}{(n+1)} \tau_R T_f^{\,4} \tag{10.17}$$

where

$$T_f^{\,4} \equiv \frac{L}{16\,\pi\sigma r^2} \tag{10.18}$$

and

$$\tau_R \equiv \int_r^{\infty} \kappa_R \rho \, dr \tag{10.19}$$

$$= \frac{\alpha K}{2} \left[\frac{3(4-p)KL}{64\pi\sigma(n+1)} \right]^{\left(\frac{p}{4-p}\right)} r^{-2/\alpha} \tag{10.20}$$

where α is defined in equation (10.25) (p. 153).

We now have the form of the temperature distribution in the limits of small and large optical depths, as given by equations (10.12) and (10.17) respectively. We wish to use these results to construct a simple approximate formula for the temperature distribution at all optical depths, which has the correct limiting forms at small and large optical depths and provides a smooth transition in between. The simplest way to construct such a formula is just to add together the expressions for T^4 given in equations (10.12) and (10.17); the result is

$$T^4 = W^{\frac{4}{4+p}} T^{*4} + \frac{3(n + p/2 - 1)}{(n+1)} \tau_R T_f^{\,4} \, . \tag{10.21}$$

It is easily verified that at small optical depths the first term on the right-hand side of this equation becomes much larger than the second term, whereas at large optical depths the second term dominates. Thus equation (10.21) has the correct limiting forms, as required. In using this equation in the calculations it is convenient to express T as a function of τ_R, τ_R being here defined by equation (10.20) throughout the whole cloud. After some algebra, the result can be written in the form

$$T = T_o f(\tau_R) \tag{10.22}$$

where

$$T_o^{\,4} = \left[\alpha^{-4} \beta^{-p} \left(\frac{2}{K} \right)^4 \left(\frac{L}{16\,\pi\sigma} \right)^{2n-2} \right]^{\frac{\alpha}{4-p}} \tag{10.23}$$

and

$$f(\tau_R)^4 = \beta \left[A \tau_R^{\,-\left(\frac{p}{4+p}\right)\alpha} + \tau_R \right] \tau_R^{\,\alpha} \, , \tag{10.24}$$

where

$$\alpha = \frac{4 - p}{2n + p - 2} \quad , \qquad \beta = \frac{3(n + p/2 - 1)}{n + 1} \; . \tag{10.25}$$

In equation (10.24) A is an undetermined constant related to T^* and r^*. τ_R is related to τ_λ by

$$\tau_R = \left[C(\lambda T_o)^p \tau_\lambda \right]^{\gamma/\alpha} \tag{10.26}$$

where

$$C = \frac{\alpha}{\gamma} \beta^{p/4} \left[\frac{24\zeta(4)}{\Gamma(5-p)\zeta(4-p)c_2^{\,p}} \right] \tag{10.27}$$

and

$$\gamma = \frac{2}{n-1} \; . \tag{10.28}$$

In our formulas for the temperature distribution we still have one undetermined parameter A. We have arbitrarily chosen this parameter such as to satisfy the condition that the resulting spectrum calculated from equation (10.8) must be properly normalized, i.e. when integrated over all wavelengths must give the correct total luminosity L. Some values of A determined in this way are listed below:

n	p	A
3/2	1	0.831
3/2	3/2	0.645
3/2	2	0.354
2	3/2	0.965

These numbers have been determined simply by integrating the spectrum numerically over all wavelengths and adjusting A until the result is properly normalized.

In the grey case $(p = 0, \tau_\lambda = \tau_R = \tau)$, the formulas simplify considerably. When the above procedure for constructing a simple approximation to the temperature distribution is applied in the grey case, the result is

$$T^4 = \left[1 + \frac{3(n-1)}{(n+1)} \tau\right] T_f^4 \tag{10.29}$$

with in this case no undetermined parameter A. This form for the temperature distribution in the grey case is supported by the work of Chapman (1966) who studied the special case $n = 3$. For $n = 3$ our approximation becomes

$$T^4 = (1 + \frac{3}{2} \tau) T_f^4$$

whereas Chapman's approximation, based on some detailed calculations of the radiation field, is equivalent to

$$T^4 = (1.154 + \frac{3}{2} \tau) T_f^4 .$$

Our approximation may perhaps even be better than Chapman's, since (a) it is correct at very small optical depths, whereas Chapman's is not, and (b) the normalization error in the emitted spectrum as calculated from equation (10.8) is smaller for our approximation than for Chapman's.

In the grey case we have eliminated the normalization error by means of the following slight modification of equation (10.29), which still retains the correct limiting forms at small and large optical depths:

$$T^4 = \left[1 + \left(\frac{3(n-1)}{(n+1)} \tau \right)^{\delta} \right]^{1/\delta} T_f^{\,4}. \tag{10.30}$$

For $n = 3/2$ the appropriate value of δ is about 1.14, and for $n = 2$ it is about 1.11.

In the non-grey case our approximation for the temperature distribution is probably not as good as in the grey case. It was attempted to derive an improved approximation to the temperature distribution in the non-grey case by calculating a "first order correction" to the radiation field at small optical depths. This introduces a correction factor of the form $(1 + a_\lambda \tau_\lambda)$ into the value of T^4 at small optical depths, where a_λ has not been precisely determined but is approximately unity at the peak wavelength of the emitted spectrum. If a correction factor of this form is inserted into the first term in square brackets in equation (10.24) and the emitted spectrum is re-normalized, the resulting differences in the temperature distribution are of the order of 10 - 15%. The effect on the resulting spectrum, while not entirely negligible, is smaller than the effect of variations in the parameter p; consequently our original approximation appears to be adequate for the present purposes, and we have not given further attention to possible improved approximations.

10.5 Results for the Emitted Spectrum

Assuming the temperature distribution given by equations (10.22) - (10.24) (or equation (10.30) for the grey case), we can now use equation (10.8) to calculate the emitted spectrum of the protostellar cloud. We write the blackbody function in the form

$$B_\lambda(T) = \frac{c_1}{\pi} \frac{1}{\lambda^5} \frac{1}{e^{c_2/\lambda T} - 1} \tag{10.31}$$

where $c_1 = 2\pi hc^2$ and $c_2 = hc/k$. If we substitute this into equation (10.8), substitute $K_\lambda = \kappa_\lambda \rho_o = \kappa_o \rho_o \lambda^{-p}$, and make use of equations (10.16) and (10.23), the resulting expression for L_λ can be written in the form

$$L_\lambda = C^{-\gamma} \frac{c_1}{\sigma} \frac{T_o L}{(\lambda T_o)^{5+\gamma p}} \int_o^\infty \frac{\tau_\lambda^{-\gamma} G_n(\tau_\lambda)\, d\tau_\lambda}{e^{c_2/\lambda T_o f(\tau_R)} - 1} \tag{10.32}$$

where C and γ are defined by equations (10.27) and (10.28), and τ_R is given as a function of τ_λ by equation (10.26). From equations (10.32) and (10.26) it is evident that L_λ depends on λ only in combination with T_o in the factor (λT_o); therefore it is convenient to consider λT_o as the independent variable and calculate L_λ as a function of λT_o. Also, it is convenient to calculate not L_λ itself but $L_\lambda/T_o L$; this quantity is normalized to unity when integrated over the independent variable λT_o. Clearly the shape of the resulting spectrum is independent of the parameters L and T_o, which only determine the absolute luminosity and wavelength scales respectively.

We have integrated equation (10.32) numerically to obtain the emitted spectrum for several choices of n and p. The results are plotted in Figs. 13 - 15 (pp. 158 - 163). Fig. 13 shows the spectrum for $n = 3/2$ and $p = 0$ (grey case), with a blackbody spectrum also plotted for comparison. It is rather remarkable that the spectrum in the grey case is very much broader than a blackbody spectrum (note that the scales are logarithmic). This result is not entirely unexpected, however, since the grey spectrum contains contributions from a wide range of temperatures.

Fig. 14 (p. 160) shows the results of some further calculations for $n = 3/2$, with $p = 1$, $p = 3/2$, and $p = 2$. It is evident from the diagram that these spectra are much narrower and closer to a blackbody spectrum than the grey spectrum, and that the resulting spectrum becomes narrower and narrower with increasing p. The reason for this is that the radiation at shorter wavelengths, which comes mainly from the hotter inner parts of the cloud, is selectively absorbed to a greater and greater extent with increasing p because of the increase in κ_λ at shorter wavelengths. At the same time, there is less long wavelength radiation from the cooler outer parts of the cloud because of the reduced opacity and hence the reduced emission at the longer wavelengths. Consequently the emitted spectrum in the non-grey case with $p > 0$ contains less radiation at both short and long wavelengths than the spectrum in the grey case. It is evident from Figs. 13 and 14 that the effect is quite large, so it appears that the grey case is inadequate even as a rough approximation for the present problem.

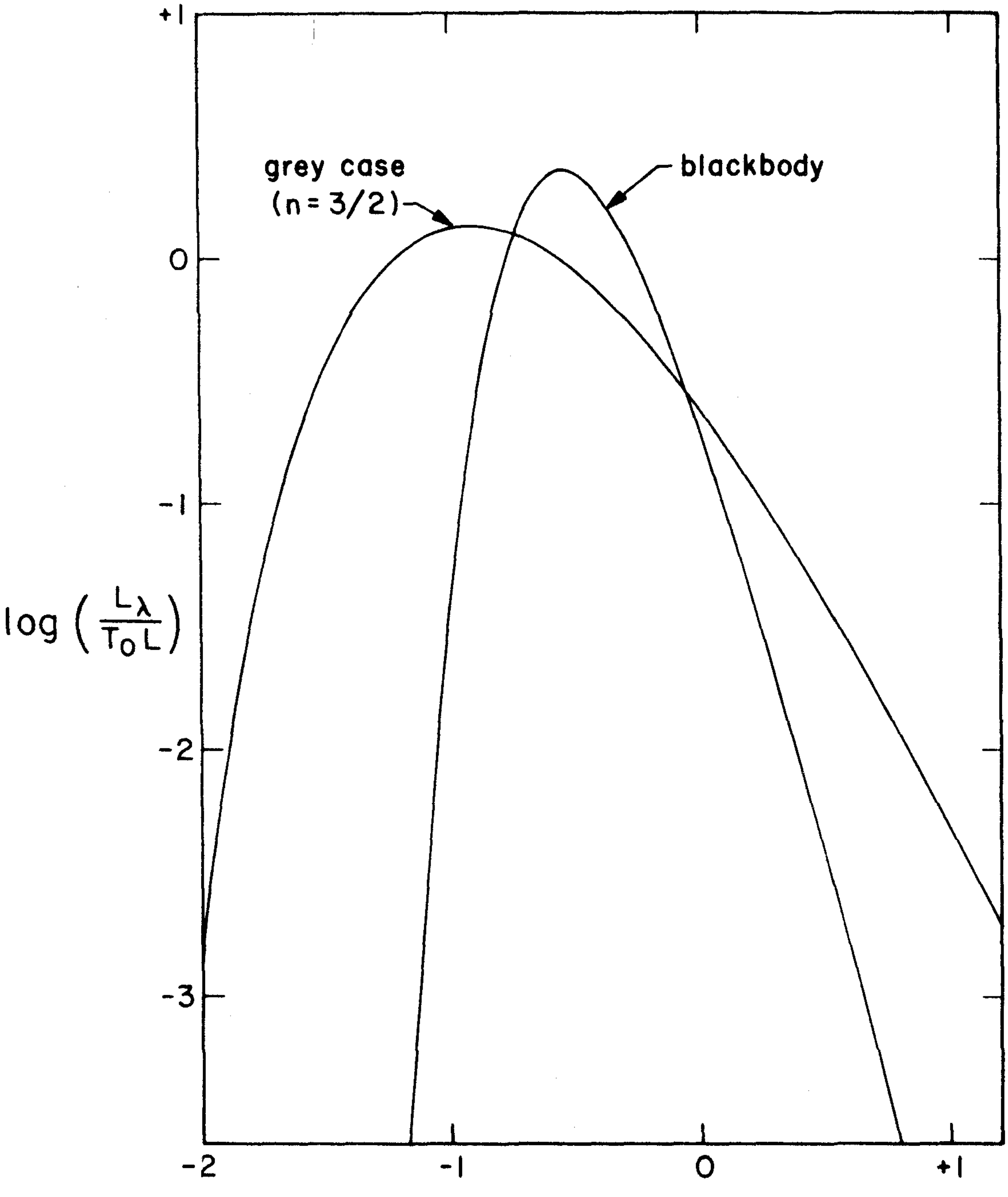
grey case
(n = 3/2)
blackbody
+1
0
-1
-2
-3
$\log\left(\frac{L_\lambda}{T_0 L}\right)$
-2
-1
0
+1
$\log(\lambda T_0)$

FIG. 13

FIG. 13 (p. 158): The calculated emitted spectrum of an infinite spherical cloud with $n = 3/2$ and $p = 0$ (grey case). A blackbody spectrum of temperature T_o is also plotted for comparison. Both curves are normalized to unity when integrated over the independent variable λT_o. All units are CGS units.

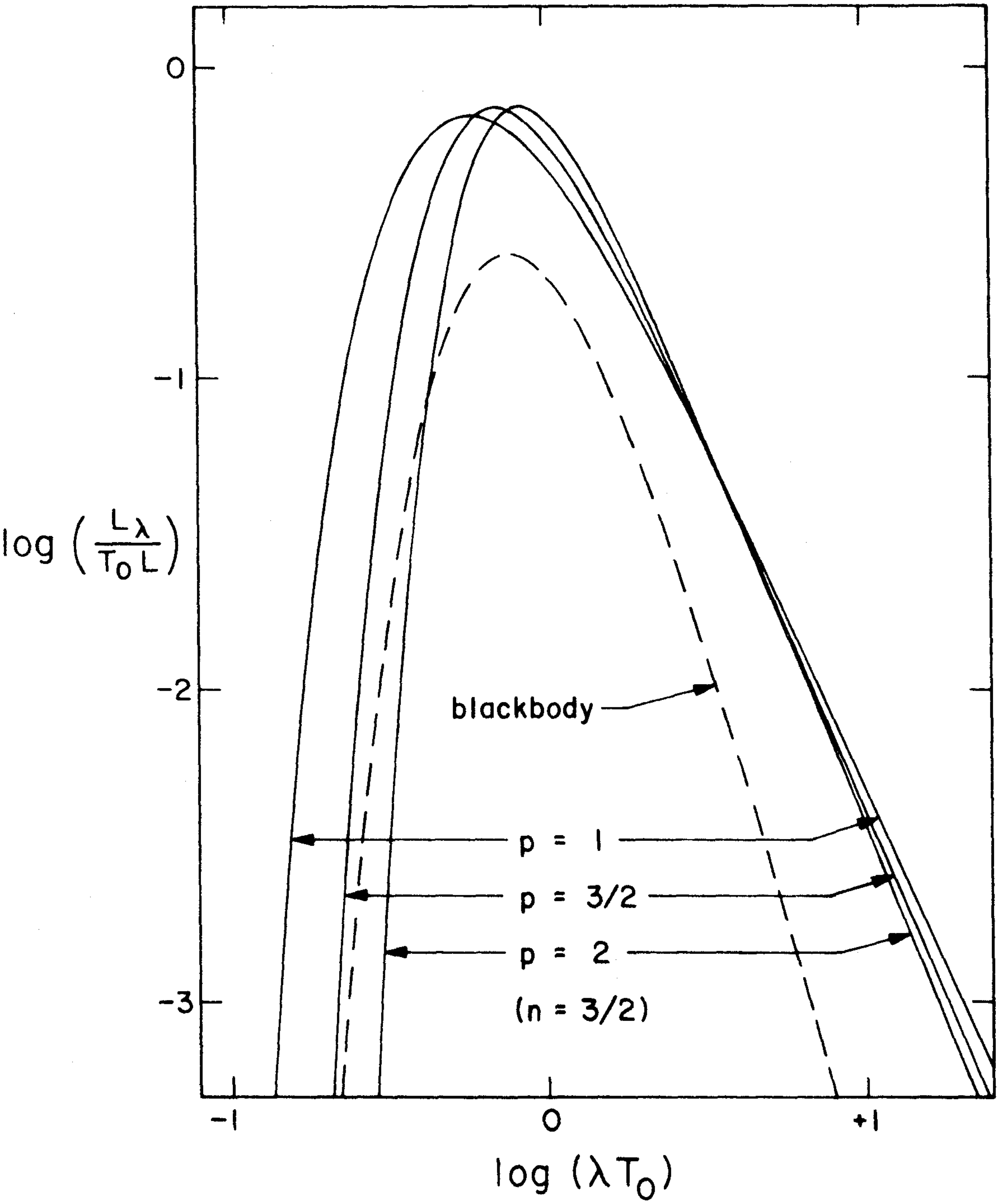
0
-1
-2
-3
$\log\left(\frac{L_\lambda}{T_0 L}\right)$
blackbody
p = 1
p = 3/2
p = 2
(n = 3/2)
-1
0
+1
$\log(\lambda T_0)$

FIG. 14

FIG. 14 (p. 160): The emitted spectrum of an infinite spherical cloud with $n = 3/2$ for the 3 cases $p = 1$, $p = 3/2$, and $p = 2$. Again the curves are normalized when integrated with respect to λT_o. The blackbody spectrum (dashed curve) has been arbitrarily positioned on the diagram for purposes of comparison.

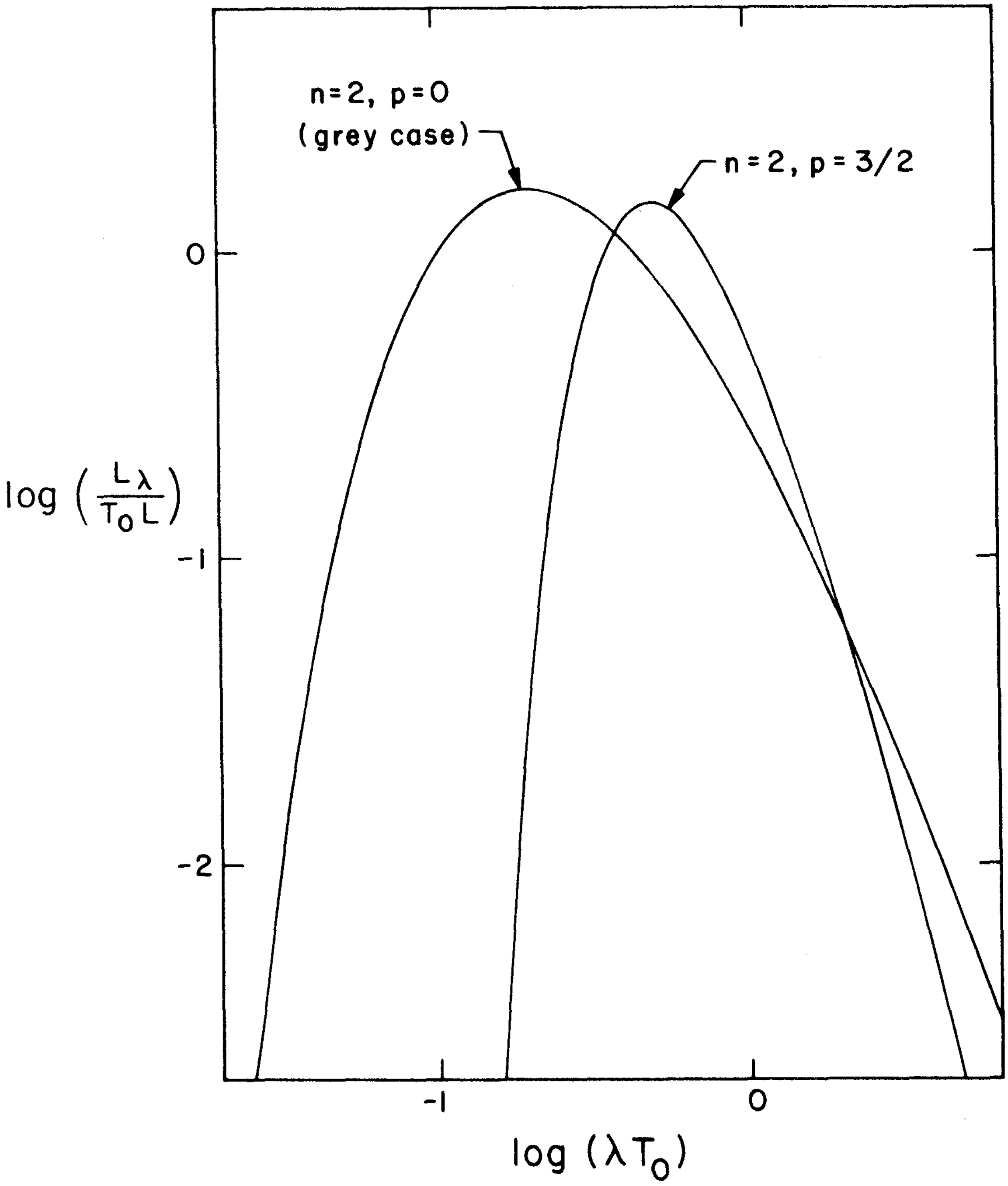
n=2, p=0
(grey case)
n=2, p=3/2
0
-1
-2
$\log\left(\frac{L_\lambda}{T_0 L}\right)$
-1
0
$\log(\lambda T_0)$

FIG. 15

FIG. 15 (p. 162): The emitted spectrum of an infinite spherical cloud with n = 2 for the 2 cases p = 0 and p = 3/2. The curves are normalized as in Figs. 13 and 14.

In Fig. 15 (p. 162) we have plotted for comparison the results of two calculations for $n = 2$, with $p = 0$ and $p = 3/2$. Again we notice that the spectrum becomes much narrower as p is increased from 0 to $3/2$, although the effect is not quite as large as for $n = 3/2$. Comparison with Figs. 13 and 14 shows that for both $p = 0$ and $p = 3/2$ the spectrum is narrower for $n = 2$ than for $n = 3/2$. This is easily understood, since for larger n the optical depth varies more rapidly with r, and therefore a smaller range of r and a smaller range of temperatures is important.

We are now in a position to predict the spectrum of a spherical protostar and its variation with time, assuming that the opacity of the dust grains can be represented by a formula of the form $\kappa_\lambda = \kappa_o \lambda^{-p}$ and that reasonable values for κ_o and p can be estimated. Unfortunately, as we have noted, the infrared absorption properties of the dust grains are highly uncertain, particularly at the higher temperatures relevant here, and therefore we can hope only to obtain results which are qualitatively valid at best. For qualitative purposes we have adopted $p = 3/2$, and we have determined κ_o by fitting to Van de Hulst's (1949) theoretical curve #15 in the near infrared, using Gaustad's (1963) grain parameters. The resulting opacity law is

$$\kappa_\lambda = 7 \times 10^{-5} \lambda\,(\mathrm{cm})^{-3/2}\ \mathrm{cm}^2/\mathrm{gm} \quad . \qquad (10.33)$$

This choice of κ_o corresponds to a grain absorption efficiency Q_λ of 0.3 at $\lambda = 1\,\mu$. It should be noted that the data on which the opacity law (10.33) is based are valid for ice grains at low temperature but may not be relevant at all at the higher temperatures encountered here, since the major constituents of the grains may have evaporated at these higher temperatures.

As we have noted, the shape of the emitted spectrum depends just on the parameters n and p, and therefore remains constant as the protostar evolves. Consequently the variation in spectral appearance of the protostellar object is due only to the variation of the two parameters L and T_o, which determine the absolute luminosity and wavelength scales respectively. The total luminosity L is known from the results described in section 9 for the evolution of the stellar core, and the parameter T_o may be obtained at any time from equations (10.23) and (10.16), given κ_o as above and ρ_o which we obtain from the results of the dynamical calculations described in section 9. The parameter T_o here plays the same role as the temperature T for a blackbody spectrum; as T_o increases, the wavelength λ_{max} at which L_λ has its peak value decreases, the product $\lambda_{max}T_o$ remaining constant. Thus we can conveniently present the results for the variation in spectral appearance of the protostar in a diagram analogous to the HR diagram, in which we plot L vs. λ_{max} for the protostar as it evolves. This has been done for several of our cases in Figs. 16 - 18 (pp. 167 - 172). In these diagrams we have added a scale giving the "apparent blackbody temperature" T_b defined by $\lambda_{max}T_b = 0.29$ cm ^oK. (It happens fortuitously that for $n = 3/2$ and $p = 3/2$ the emitted spectrum is not very different from a blackbody spectrum, except that it falls off less rapidly at long wavelengths.)

The results for our "standard" Case 1 are shown in Fig. 16 (p. 167), which corresponds to Fig. 5 (p. 126) for the evolution of the stellar core. We note that λ_{max} continually decreases and T_b increases during the evolution, while the luminosity first increases and then decreases again. The reason for the decrease in λ_{max} is that as the collapse proceeds the density of the infalling material decreases, and the point of optical depth unity in the collapsing cloud moves inward to smaller radii and higher temperatures. It is seen in Fig. 16 that during the course of the evolution λ_{max} decreases from more than 50 μ to roughly 1.5 μ, the maximum luminosity being achieved when $\lambda_{max} \sim 10\ \mu$. Actually λ_{max} is not well determined, since it is sensitive to the poorly known opacity of the infalling material. Since it is quite possible that the opacity may be considerably less than we have assumed, due to evaporation of some of the grain constituents, we have also shown in Fig. 16 the result of reducing κ_o by a factor of 10; this shifts the whole curve to the left (smaller λ_{max}) by 0.4 in $\log \lambda_{max}$. This occurs because when the opacity of the material is reduced, optical depth unity in the infalling cloud is shifted to a smaller radius and a higher temperature.

In the innermost part of the cloud the temperature becomes higher than the temperature at which the dust grains evaporate completely; consequently, supposing the dust grains to evaporate instantaneously (which may not be a good assumption), the opacity drops essentially to zero in this central region where the grains have

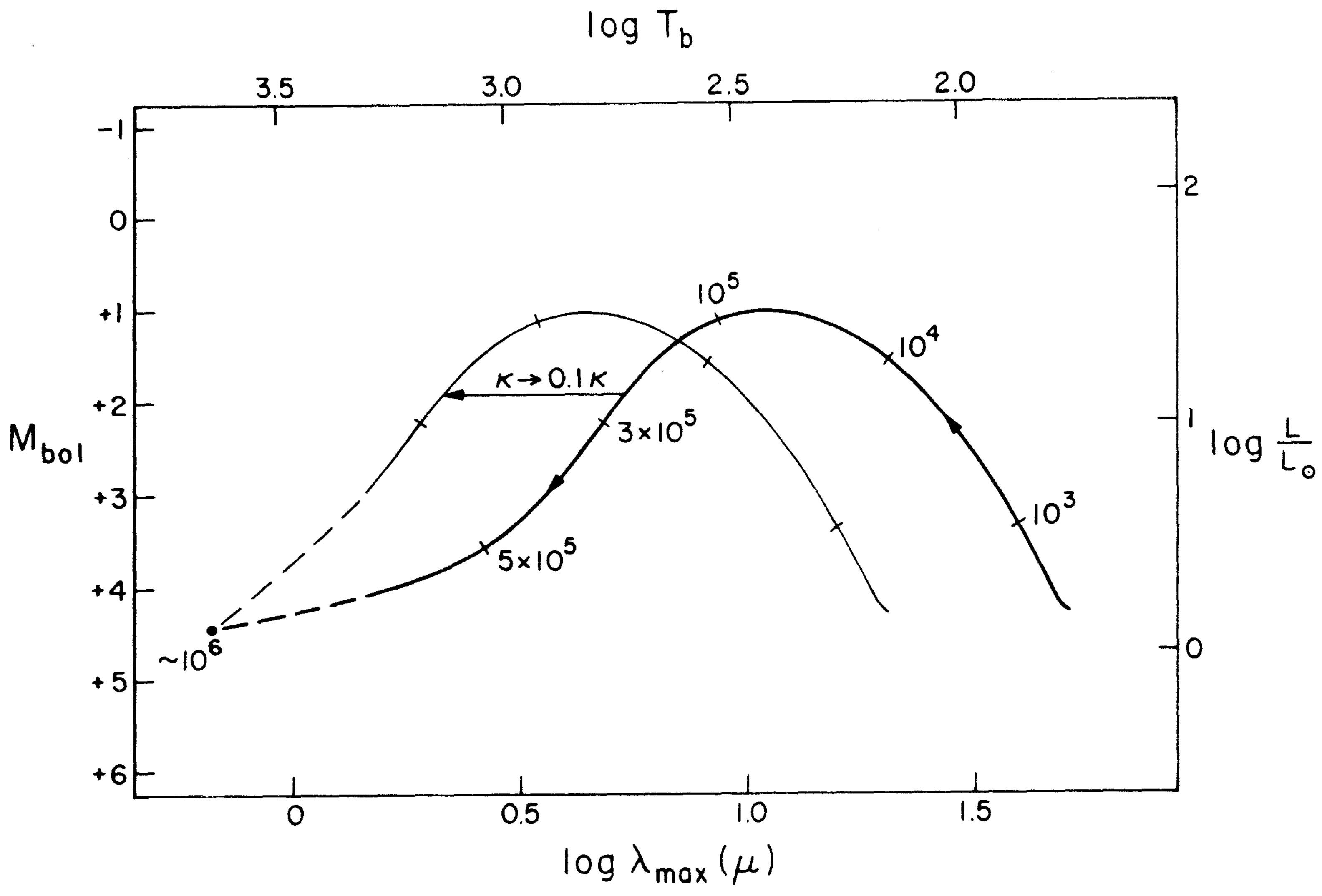
log T_b
3.5
3.0
2.5
2.0
M_{bol}
-1
0
+1
+2
+3
+4
+5
+6
log $\frac{L}{L_\odot}$
2
1
0
10^5
10^4
10^3
$\kappa \to 0.1\kappa$
3×10^5
5×10^5
$\sim10^6$
0
0.5
1.0
1.5
log λ_{max} (μ)

FIG. 16

FIG. 16 (p. 167): The evolution in spectral appearance of the protostellar cloud in the "standard" Case 1 (heavy curve), corresponding to Fig. 5 (p. 126) for the evolution of the stellar core. The times are marked along the curve in years after the formation of the stellar core, as in Fig. 5. The lighter curve and the arrow marked "$\kappa \rightarrow 0.1\ \kappa$" show the effect of reducing the dust opacity by a factor of 10. See section 10.5 for further explanation of the diagram.

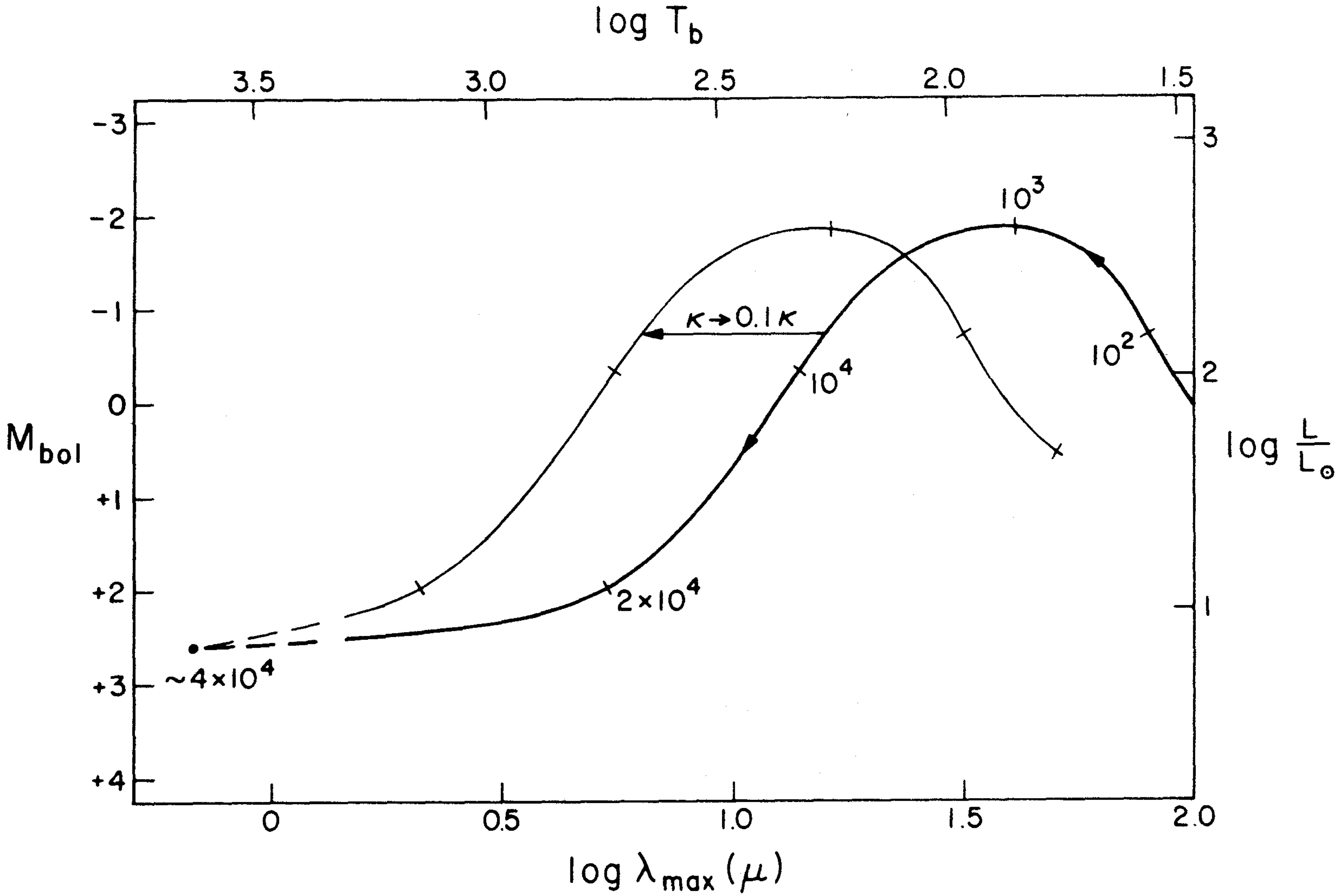
log T_b
3.5
3.0
2.5
2.0
1.5
M_{bol}
-3
-2
-1
0
+1
+2
+3
+4
log $\frac{L}{L_\odot}$
3
2
1
10^3
10^2
$\kappa \rightarrow 0.1\kappa$
10^4
2×10^4
$\sim4\times10^4$
0
0.5
1.0
1.5
2.0
log λ_{max} (μ)

FIG. 17

FIG. 17 (p. 169): The evolution in spectral appearance of the protostellar cloud in Case 2, corresponding to Fig. 6 (p. 128) for the evolution of the stellar core. The explanation is the same as for Case 1 (see p. 168).

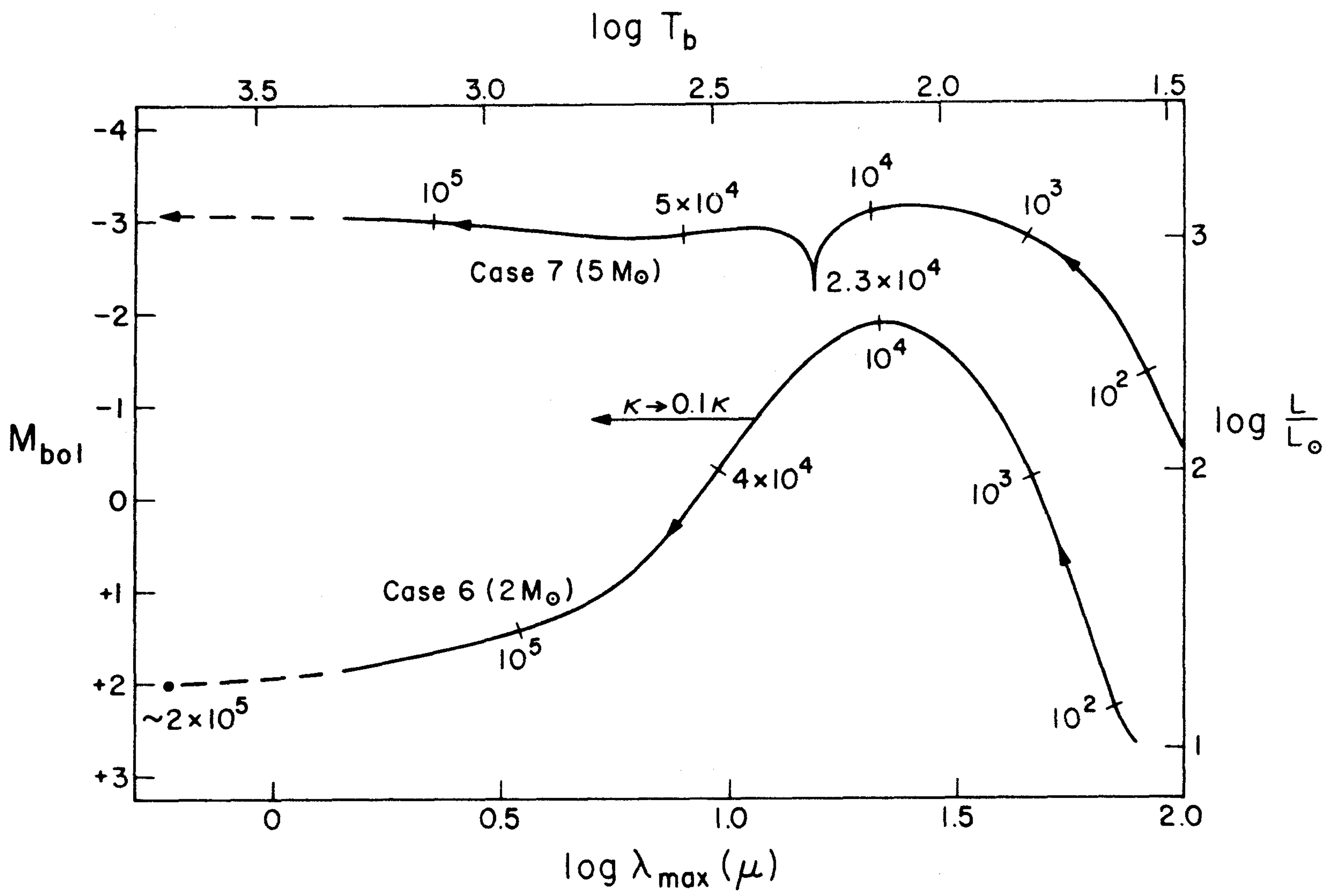
log T_b
3.5
3.0
2.5
2.0
1.5
M_{bol}
-4
-3
-2
-1
0
+1
+2
+3
log $\frac{L}{L_\odot}$
3
2
1
10^5
5×10^4
10^4
10^3
10^2
2.3×10^4
Case 7 (5 $M_\odot$)
10^4
$\kappa \to 0.1\kappa$
4×10^4
10^3
10^2
Case 6 (2 $M_\odot$)
10^5
$\sim2\times10^5$
0
0.5
1.0
1.5
2.0
log λ_{max} (μ)

FIG. 18

FIG. 18 (p. 171): The evolution in spectral appearance of the protostellar cloud in Cases 6 ($M = 2\ M_{\odot}$) and 7 ($M = 5M_{\odot}$), corresponding to Figs. 10 (p. 136) and 11 (p. 138) respectively for the evolution of the stellar core. See section 10.5 for explanation of the curves.

evaporated. Thus when the optical depth at the point where the grains evaporate gets down to a value of the order of unity or less, it is no longer valid to consider the cloud as completely optically thick, and the emitted spectrum no longer has the shape which we have calculated. If we suppose the grains to evaporate at 2000 °K, for example, this happens when $\lambda_{max} \sim 1.5\ \mu$ and $T_b \sim 2000$ °K. This point is indicated in Fig. 16 by the transition from a solid to a dashed line. After this point the observed spectrum will consist of two distinct components: (1) radiation from the central stellar object, still attenuated by the surrounding dust, and (2) infrared emission from the dust cloud at a maximum temperature of the order of 2000 °K. This phase is indicated in Fig. 16 (p. 167) by the dashed line, which is not an evolutionary path in the diagram but merely connects the end of the solid curve with the position of the star finally resulting at the end of the collapse, represented in the diagram by the filled circle. The spectrum during this phase of the evolution will be discussed in more detail in section 10.6.

Fig. 17 (p. 169) shows the results for the evolution in spectral appearance of the protostar in Case 2. We note that the shape of the curve in this case is much the same as in Case 1. Quantitatively it differs in being shifted to higher luminosities (because of the higher core luminosity) and larger values of λ_{max}. The reason for the shift to longer wavelengths is that the density of the protostellar cloud is higher at corresponding stages in Case 2 than in Case 1, and therefore optical depth unity occurs farther out in the cloud where the temperature is lower.

Cases 3, 4, and 5 have not been plotted because Case 3 is quite similar to Case 2, and Cases 4 and 5 are quite similar to Case 1. The results for Cases 6 ($M = 2\ M_\odot$) and Case 7 ($M = 5\ M_\odot$) are shown in Fig. 18 (p. 171). Case 6 and the early stages of Case 7 are again qualitatively similar to Cases 1 and 2, whereas the later stages of Case 7 are qualitatively different due to the differences in the evolution of the stellar core. The sharp dip in luminosity in Case 7 arises because of the rapid increase in radius and the consequent decrease in luminosity of the core when the outer layers of the core come into radiative equilibrium. The luminosity does not decrease again as in the other cases but remains approximately constant because it comes mainly from the radiative cooling of the stellar core and no longer primarily from the kinetic energy inflow.

For the more massive protostars, such as in Case 7, the luminosity during the later stages of the collapse is probably better determined than in the lower mass cases, because the luminosity is essentially that of a star in the radiative phase of pre-main sequence contraction and is not strongly dependent on the dynamics of the collapse, as for the lower masses. If we extrapolate to still higher masses, it appears that the central stellar object may even reach the main sequence before all of the surrounding material has been either accreted or dissipated; observationally, we would then have an infrared dust cloud such as we have described, whose luminosity is supplied by what is essentially an ordinary main sequence star at the center.

10.6 The Emitted Spectrum for a Non-Optically Thick Cloud

We now consider the case where the infalling cloud is no longer completely optically thick and the spectrum contains a component due to the central stellar object. Again, because of the uncertainties in the properties of the dust grains and because of the highly idealized nature of our model for the dust cloud, we can hope only to obtain results which are qualitatively valid at best. Therefore we have not attempted any accurate solution of the problem, but have only considered some simple approximations in order to see what might be expected qualitatively. In any case, the present situation presents an even more difficult problem in radiative transfer theory than the optically thick case, and deriving an accurate solution would be impracticable in the present project.

First, we consider the spectrum emitted from the dust cloud alone. In the present situation the function $G_n(\tau_\lambda)$ in the integral expression for the emitted luminosity L_λ (equation 10.32) is no longer strictly applicable, since the function $G_n(\tau_\lambda)$ includes the effects of absorption in the central part of the cloud where in the present situation there is no dust and therefore no absorption. Thus the corresponding function valid in the present situation would actually be somewhat larger than $G_n(\tau_\lambda)$. The difference is however expected to be unimportant, and we have neglected it.

Another difference from the optically thick case is that the radiation field in the dust cloud is altered by the absence of dust in the central part of the cloud, and consequently the temperature distribution is also different from the optically thick case. Again this effect is not expected to be very important for qualitative purposes, and we have neglected it and continued to use equations (10.22) - (10.24) for the temperature distribution in the non-optically thick case.

In using equation (10.32) to calculate the emitted spectrum in the non-optically thick case, the upper limit on the integral must be taken not as ∞ but as the value of τ_λ at the point where the dust grains evaporate. As the density of the infalling material decreases, so does the optical depth at the point where the dust grains evaporate; correspondingly, the spectrum emitted from the dust cloud varies through a one-parameter sequence of curves. It turns out (somewhat fortuitously) that for $n = 3/2$ and $p = 3/2$ the shape of the emitted spectrum changes very little as the optical depth of the cloud decreases, the spectrum becoming slightly broader and less like a blackbody spectrum with decreasing optical depth. For $p = 2$ the variation is somewhat greater, but in the optically thin limit the shape of the spectrum for $p = 2$ becomes almost identical with that for $p = 3/2$. The various differences seem unimportant for the present purposes, so we have not plotted these curves separately.

Since there is a maximum temperature for the dust grains, namely the dust evaporation temperature T_d, the wavelength λ_{max} of maximum emission from the dust cloud approaches a minimum value when the optical depths become very small. From the calculated spectra we find that for both $p = 3/2$ and $p = 2$ the value of

λ_{max} in the optically thin limit is related to T_d by $\lambda_{max} T_d \simeq 0.30$, which compares closely with the relation $\lambda_{max} T_d = 0.29$ which would hold for a blackbody spectrum of temperature T_d. Thus the spectrum of the dust cloud in the optically thin limit is qualitatively like a blackbody spectrum of temperature equal to the dust evaporation temperature, the main difference being that the dust cloud spectrum falls off less rapidly at long wavelengths than a blackbody spectrum.

We now consider the total spectrum resulting from the superposition of the dust cloud spectrum on the dimmed and reddened spectrum of the central star. For qualitative purposes we have represented the stellar spectrum by a blackbody spectrum, and instead of using the proper interstellar extinction law at visual wavelengths (which in any case is not necessarily applicable here), we have simply assumed the opacity law $\kappa_\lambda = \kappa_o \lambda^{-p}$ to hold at all wavelengths. The resultant spectrum has been calculated in approximately normalized form from the equation

$$\frac{L_\lambda}{L} = e^{-\tau_\lambda} \frac{B_\lambda(T_s)}{B(T_s)} + \frac{L_\lambda(\tau_\lambda)}{L} , \qquad (10.34)$$

where $\tau_\lambda = \tau_\lambda(T_d)$ is the optical depth at the point where the dust grains evaporate, and T_s is the temperature of the (blackbody) stellar spectrum. In equation (10.34) the first term on the right-hand side represents the contribution from the central stellar object, and the second term represents the contribution from the surrounding dust cloud. The dust spectrum $L_\lambda(\tau_\lambda)/L$ has been calculated numerically from equation (10.32) in the same way as in the optically thick case, the only difference being that the integral has been cut off at the finite optical depth $\tau_\lambda(T_d)$.

As the cloud density and the optical depth $\tau_\lambda(T_d)$ decrease, the stellar contribution to the resultant spectrum becomes larger and larger, while the dust cloud contribution becomes smaller. Thus the resultant spectrum varies through a whole one-parameter family of curves with varying relative strengths of the stellar and dust components. To illustrate the possibilities, we have made calculations for $p = 3/2$, assuming $T_s = 5000\ ^\circ K$ and three different values for T_d, namely 1500, 1000, and 500 $^\circ K$. The resulting 3 familes of curves are illustrated in Figs. 19, 20, and 21 respectively (pp. 180 - 185). We note that the corresponding curves for higher values of T_s or T_d are the same as the ones we have plotted if all temperatures are scaled up and all wavelengths are scaled down by the same factor.

The curves in Figs. 19 - 21 have been labeled with the value of the optical depth $\tau_\lambda(T_d)$ at a wavelength of 1 μ. In all cases the emergence of the stellar component and the decrease of the dust cloud component with decreasing optical depth is evident. The time scale for variation of the spectrum is of course related to the time scale for the change in density of the infalling material. In Case 1, for example, the time scale is such that the time interval between adjacent curves in Fig. 19 is about 3×10^4 years, while for Figs. 20 and 21 it is about 4×10^4 years.

It should be remembered that the curves plotted in Figs. 19 - 21 are based on a very simple model of the dust cloud, which will probably not be applicable in a real situation; thus for example the infalling cloud is assumed to be spherically symmetric, whereas in reality there is no reason to expect the infalling cloud to be spherically symmetric. If the cloud has inhomogeneities or deviations from spherical symmetry, these could produce more or less absorption of the stellar radiation along a particular line of sight than a spherically symmetric cloud, and this would alter both the shape of the spectrum and the apparent total luminosity of the object. For example, if there are "holes" in the infalling cloud it is possible that the central stellar object may become visible at an earlier stage of the collapse than indicated by our results. Thus the results presented in this section should be taken as only indicative in qualitative fashion of the possibilities, and not as a prediction of what a protostellar object or young star would actually look like.

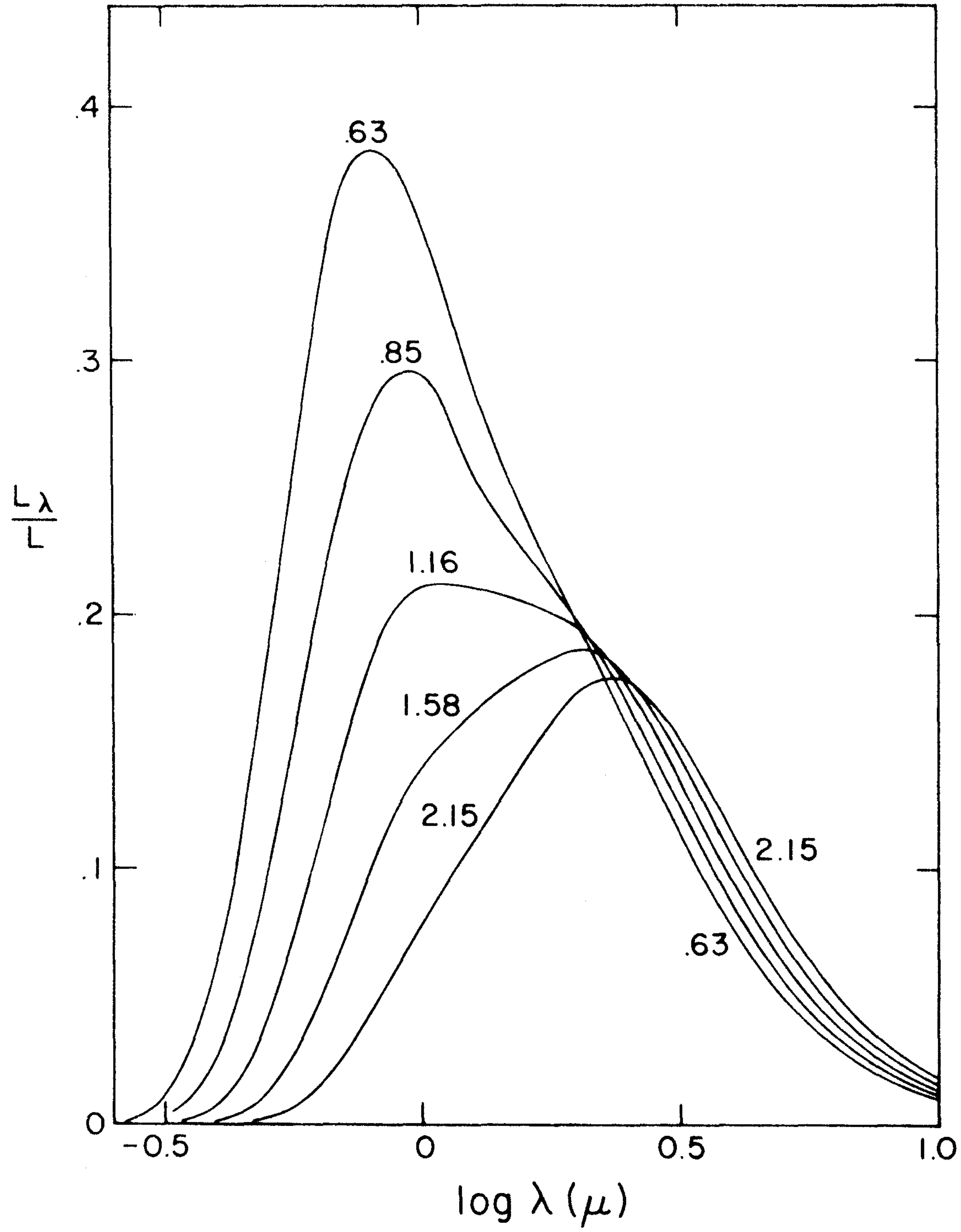

FIG. 19

FIG. 19 (p. 180): The spectrum of the protostellar object when the infalling cloud is no longer optically thick. These curves have been calculated for $p = 3/2$, $T_s = 5000\ ^{\circ}K$, and $T_d = 1500\ ^{\circ}K$, and are approximately normalized when integrated over λ if the unit of λ is taken as $1\ \mu$. The curves are labeled with the optical depth of the cloud at a wavelength of $1\ \mu$.

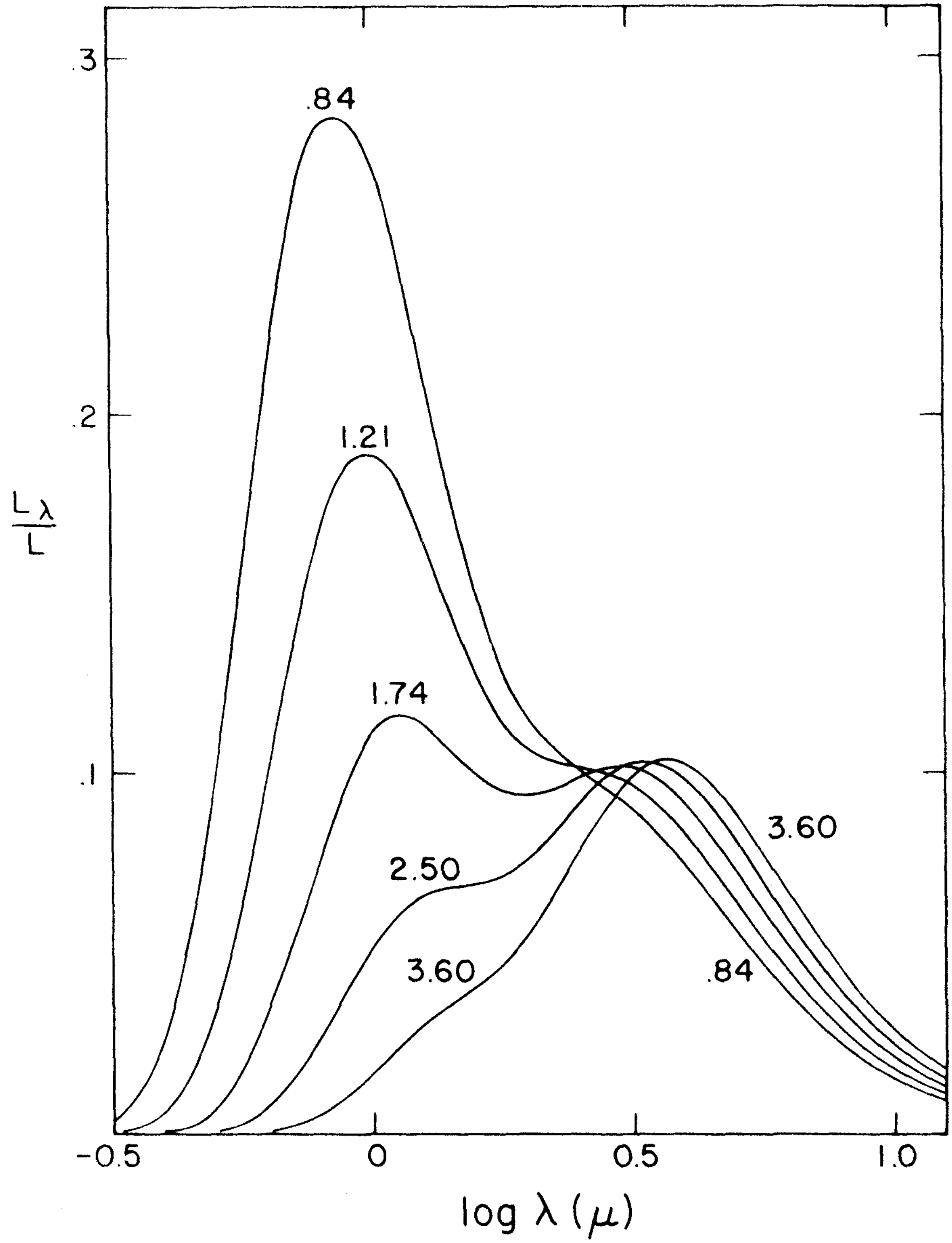

FIG. 20

FIG. 20 (p. 182): Same as Fig. 19 (p. 180), but with $T_d = 1000\ ^{\circ}K$.

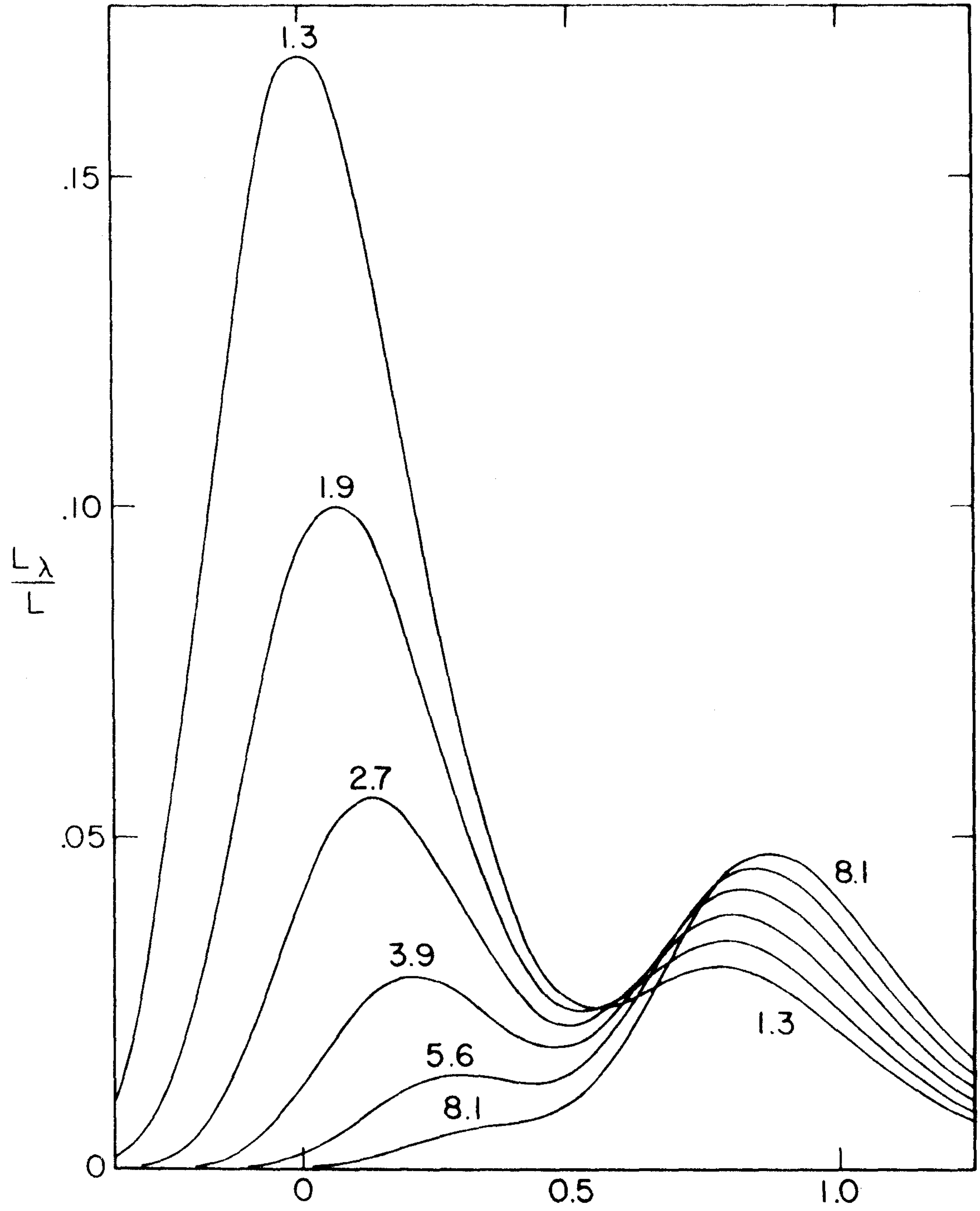

FIG. 21

FIG. 21 (p. 184): Same as Fig. 19 (p. 180), but with $T_d = 500\ ^{\circ}K$.

11. COMPARISON WITH OBSERVATIONS

11.1 Introduction

When the present project was begun, it was not realized that there would be any observations with which our results might bear any comparison, and therefore our calculations have for the most part not been made with comparison with observations in mind. As it has turned out, however, the past few years have seen a remarkable development in various kinds of new observational results which are currently thought to relate to star formation and young stars. In this final section we shall briefly describe some of the observations which may be relevant, and indicate how they could possibly be explained by our theoretical results. We shall not attempt a complete review of all of the observations which may be relevant for star formation or newly formed stars. Since the various observational data are still rather sparse and preliminary, and the interpretations are still uncertain, many of the statements in this section must be taken as only quite provisional.

11.2 Infrared Observations in Orion

Becklin and Neugebauer (1967) have reported observations of an infrared point source in the Orion nebula which they think may be a protostar. The infrared flux measurements for this object are plotted in Fig. 22 (p. 187). It is not known to what extent the observations may be affected by interstellar extinction, but qualitatively the appearance of this object is much the same as would be predicted

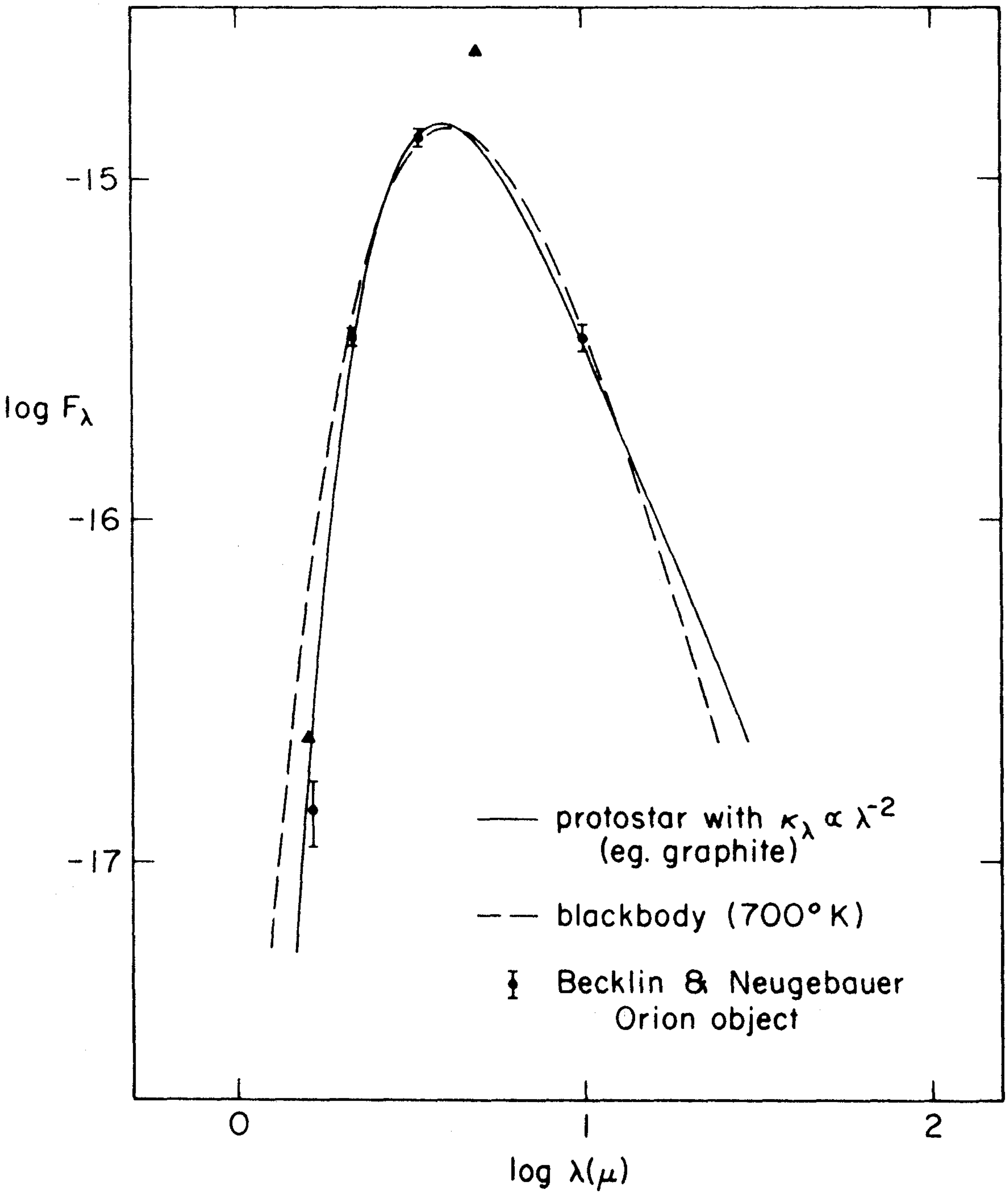
log F_λ
-15
-16
-17
0
1
2
log $\lambda(\mu)$
protostar with $\kappa_\lambda \propto \lambda^{-2}$ (eg. graphite)
blackbody (700° K)
Becklin & Neugebauer Orion object

FIG. 22

FIG. 22 (p. 187): Infrared flux measurements of the Becklin-Neugebauer object in Orion. The filled circles with error bars are the observations reported by Becklin and Neugebauer (1967), and the triangles are observations by Kleinmann and Low (1967). See text, section 11.2, for explanation of the curves fitted to the observations. The unit of F_λ is watts/cm^2/μ.

from our calculations for a protostar during the phase when the infalling cloud is still optically thick. The bolometric magnitude (~ -2) and the apparent blackbody temperature (~ 700 ^{o}K) inferred for this object are within the range of our calculations for evolving protostars (see for example Fig. 18, p. 171). If the Becklin-Neugebauer object is interpreted as a protostar, it appears that the mass of the object must be more than 1 $M_\odot$, perhaps more like 5 $M_\odot$. As was mentioned earlier, however, our calculation for 5 $M_\odot$ is not necessarily realistic, so any comparison with the calculated results in this case is subject to uncertainty on both observational and theoretical accounts.

In Fig. 22 the filled circles with error bars are the observations reported by Becklin and Neugebauer (1967), and they have been fitted as well as possible with a blackbody spectrum (dashed curve) and with the best fitting curve from among our calculations for the spectrum of a protostar (solid curve; see section 10.5). The best fitting curve is the one for $p = 2$, as would be appropriate for example for graphite dust grains. The triangles in Fig. 22 are observations reported by Kleinmann and Low (1967), for which however no errors are quoted. It is evident that when the 5 μ observation of Kleinmann and Low is included, the points no longer fit any of our simply calculated curves. However, because of the unknown dust absorption properties and the idealized nature of our model, it may be premature to attach much significance to a comparison of this kind.

Kleinmann and Low (1967) have reported observation of an extended infrared nebula near the Becklin-Neugebauer point source in Orion. This extended nebula apparently radiates most of its energy at much longer wavelengths than the Becklin-Neugebauer object, and is inferred with considerable uncertainty to have a linear diameter of $\sim 2 \times 10^{17}$ cm, a luminosity of $\approx 10^5 \, L_\odot$, and an "effective temperature" of $\approx 70\,^\circ$K. Hartmann (1967) has interpreted this object as an opaque dust cloud whose luminosity is supplied by a group of massive newly formed stars imbedded in it. A similar idea has also been proposed by Davidson and Harwit (1967). This is qualitatively the same kind of situation as is predicted by our calculations for star formation. Our calculations are probably not directly applicable to this object, however, since it appears that the formation of a multiple system or at least a single very massive star may be involved.

It is interesting that the source of OH radio emission in the Orion nebula has recently been found to coincide very closely in position with the Becklin-Neugebauer object (Raimond and Eliasson 1967). Thus there is a possibility that the OH sources are in fact protostars. We shall not speculate on the possible origin of the OH emission, but we note that in the inner part of a collapsing protostellar cloud there is a possibility of achieving highly excited conditions in a very small volume of space. If the OH sources are in fact protostars, the radio observations may provide a means of observing the inner part of a collapsing protostellar cloud which is heavily obscured by the dust in the surrounding material.

11.3 Gross Spectral and Luminosity Characteristics of T Tauri Stars

It is generally believed that the T Tauri stars are newly formed stars which are still contracting toward the main sequence. Therefore it is of interest to see if our results for the final stages of star formation bear any relation to the observed properties of T Tauri stars. The properties of T Tauri stars have been reviewed with reference to their evolutionary significance by Kuhi (1966) and Herbig (1962, 1967).

First, as regards position in the HR diagram, the T Tauri stars are somewhat scattered, but they tend to lie a few magnitudes above the main sequence, and they are mostly in the temperature range 3500 - 6000 $^{\circ}$K. The corresponding radii are mostly in the range of a few solar radii. This is the same region of the HR diagram where the lower part of the Hayashi track for stars of moderate or low mass is located. This situation is consistent with what our calculations would predict for newly formed stars, since we have found that a newly formed star of mass near one solar mass first appears toward the lower end of the Hayashi track. It is interesting to note in an HR diagram given by Herbig (1967) that there appears to be a concentration of T Tauri stars with surface temperatures between 4000 and 5000 $^{\circ}$K and radii near 2 $R_{\odot}$; this coincides with the position in the HR diagram where a star of 1 $M_{\odot}$ first appears on the Hayashi track, according to our calculations for the "standard" Case 1. This coincidence is almost certainly fortuitous, but it at least is not inconsistent with our results, and may perhaps even be taken as in some degree confirming our predictions.

Mendoza (1966) has made wide-band photometric measurements of some T Tauri stars in the UBVRIJKL system, covering a wavelength range from 0.36 μ to 5 μ. Using the absolute flux calibration for this magnitude system (Johnson 1965b), one can derive rough spectral energy distributions for these stars. We have done this, and the resulting spectra as plotted on an arbitrary flux scale are shown in Fig. 23 (p. 193). As is pointed out by Mendoza, all of these objects show infrared excesses relative to a normal stellar spectrum. It is evident in Fig. 23 that in some cases the infrared excess is very large; in the case of R Mon, in fact, the infrared emission is completely dominant over the visual radiation, i.e. nearly all of the energy is emitted in the infrared.

Qualitatively, these observations are just what our calculations would predict for the final stages of star formation, when a stellar object has appeared but it is still surrounded by some of the original protostellar material which has not yet been accreted or dissipated. The dust grains in this surrounding material absorb some of the stellar radiation and re-radiate it in the infrared, as was discussed in section 10. Figs. 19 - 21 (pp. 180-184) show some possible spectral energy curves for the final stages of a protostar, as calculated from our simple model (section 10.6). These curves may be compared with the observed spectra of T Tauri stars as shown in Fig. 23. Qualitatively, the calculated and observed curves look quite similar in many cases, although it does not seem possible to achieve a good quantitative fit. This should probably not be expected, however,

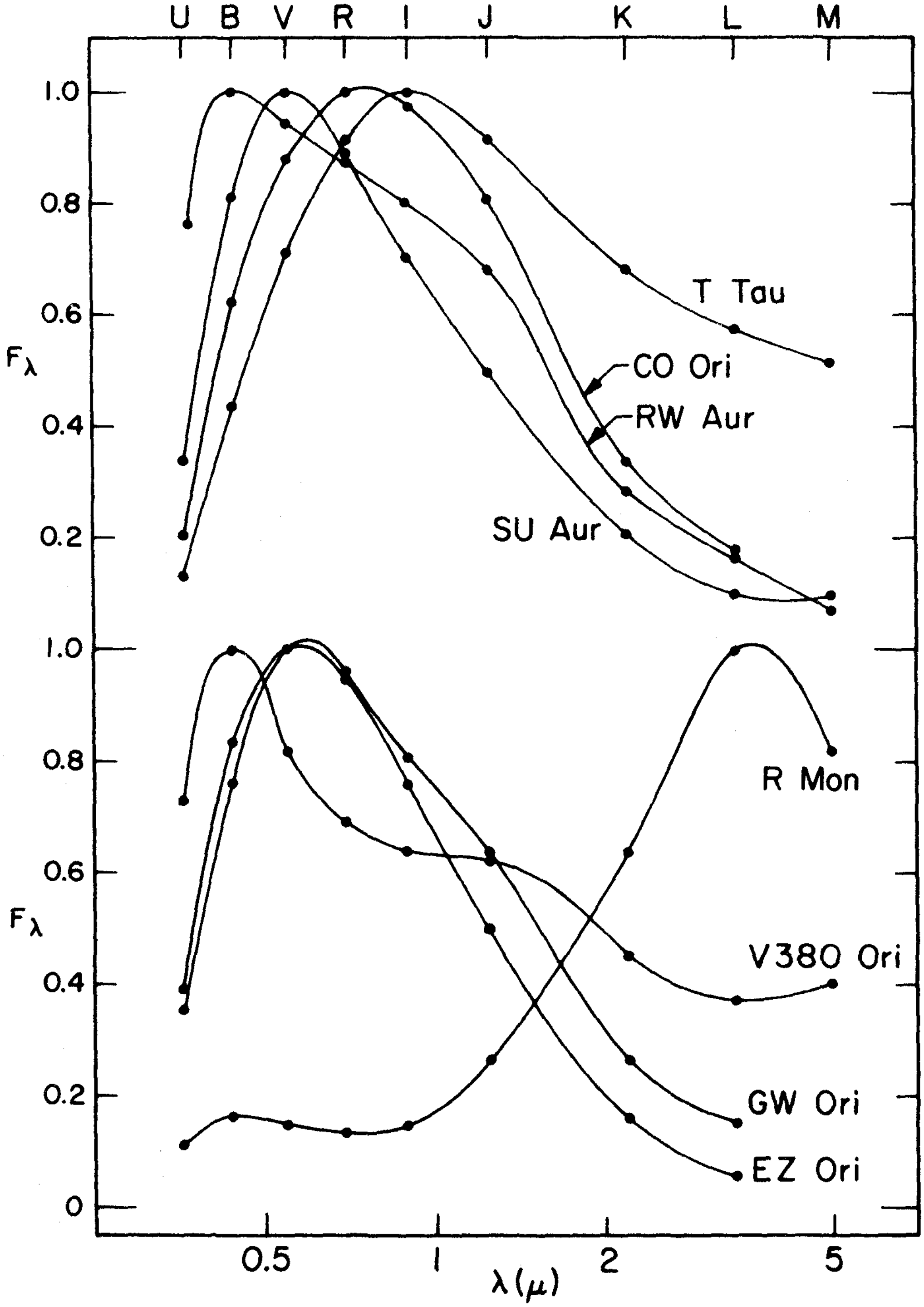
U
B
V
R
I
J
K
L
M
1.0
0.8
0.6
0.4
0.2
0
F_λ
T Tau
CO Ori
RW Aur
SU Aur
R Mon
V380 Ori
GW Ori
EZ Ori
0.5
1
2
5
$\lambda(\mu)$

FIG. 23

FIG. 23 (p. 193): The spectra of some T Tauri stars as observed by Mendoza (1966) and plotted with arbitrarily normalized flux scales.

since our model is probably too simple to provide a good representation, as was mentioned in section 10.6.

If we identify the observed spectra with our calculated results, it is possible to draw some inferences about the temperature of the grains responsible for the infrared emission. For example, we notice in some of the observed spectra a hump approximately at the position of the J band. If we try to match these observed spectra with calculated spectra similar to those shown in Figs. 19 - 21, we find that this hump could be produced by emission from dust grains whose evaporation temperature is in the range 2100 - 2500 $^{\circ}$K. It is interesting to note that at the relevant densities the evaporation temperature of graphite is in this same temperature range. Most of the observed spectra however show more radiation at the longer wavelengths than would be predicted by our simple model, assuming a dust evaporation temperature of the order of 2000 $^{\circ}$K. This could be interpreted either by supposing that the infalling cloud is not spherically symmetric but contains "blobs" at different temperatures, or by supposing that some of the grains or grain constituents evaporate at lower temperatures than 2000 $^{\circ}$K.

It is interesting also to note that the infrared peak in the spectrum of R Mon is similar in many respects to the Becklin-Neugebauer object in Orion. R Mon however shows a stellar spectrum, whereas the Orion object does not. Thus if R Mon and the Orion object are both to be interpreted as protostars, R Mon may be an example of a protostar in which the dust cloud has a hole through which the spectrum of the central stellar object is seen.

11.4 Other Properties of T Tauri Stars

In the spectra of some of the fainter T Tauri or T Tauri-like stars Walker (1961, 1963, 1964) has observed absorption lines shifted redward by 150 to 300 km/sec. Positive radial velocities of this magnitude can only be attributed to gravitational infall of material into the star. In our calculations for a star of 1 $M_\odot$, the infalling material is essentially in free fall and has a maximum velocity at the stellar surface ranging from 260 km/sec (Case 3) to 440 km/sec (Case 1) at the time when the star first comes onto the Hayashi track. The masses and radii of Walker's stars are unknown, but the velocities observed by Walker are at least in order-of-magnitude agreement with the expected free fall velocity at the stellar surface. Thus it appears that the infall of material found in our calculations is actually observed in at least some newly formed stars. The fact that only relatively few T Tauri stars seem to show the effect could conceivably be interpreted in several ways; one possible interpretation is that the time during which infall is observable is relatively short, and that most of the T Tauri characteristics persist after the effects of infall have become negligible.

In at least one instance Walker observed rapid variations in the appearance of the red-shifted absorption lines. This suggests that the infall of material is not smooth and spherically symmetric as in our calculations, but may in fact involve inhomogeneities and turbulent or non-radial motions. In fact there is no reason why in reality the flow should be smooth and spherically symmetric as we have assumed.

Another effect observed in some of the fainter T Tauri-like stars is strong continuous emission in the ultraviolet region of the spectrum, which appears to increase strongly toward shorter wavelengths. In fact, all of the stars in which Walker observed the red-shifted absorption lines also show this ultraviolet emission, and according to Walker the two effects seem to be closely related. Walker suggests that the ultraviolet emission may in fact be caused by the effects of the infall of material to the stellar surface. In our theoretical model, the infalling material strikes a shock front in which it becomes heated to extremely high temperatures (up to 10^7 °K), and it then cools again by the emission of radiation. We have not studied the physics of this radiation process, but it seems that the radiation may be mostly continuous free-free emission, for which j_λ increases as λ^{-2} toward shorter wavelengths. Of course our spherically symmetric shock front is too idealized to accurately represent the real situation, but it may be that something of this sort is being observed.

The fact that both the red-shifted absorption lines and the strong ultraviolet emission tend to occur in the fainter T Tauri stars suggests that the stars showing these effects may be at an earlier stage of evolution than most T Tauri stars, still strongly obscured by surrounding material and still experiencing the effects of infall of material.

More conspicuous in most T Tauri stars than the effects mentioned above are spectral features which seem to be related to highly active conditions on the surface of these stars. All T Tauri stars (by definition) show strong chromospheric-type emission lines, and many at times show continuous emission across the spectrum which tends to veil the stellar absorption lines. Some of these effects could be due to the infall of material and the associated shock front, as mentioned above, but it seems more likely that they have their origin in violent chromospheric-type activity associated with the outer convection zone of these stars. In addition, many T Tauri stars show violet-shifted emission lines indicating ejection of material from the star; this again is probably related to activity in the convection zone, coupled with the effects of magnetic fields. It is possible that the erratic fluctuations in brightness of the T Tauri stars are also related to the violent convective activity which seems to be indicated, being caused perhaps by the irregular transport of energy to the surface by the convective motions.

APPENDIX A

NUMERICAL METHODS FOR THE EARLY STAGES OF THE COLLAPSE

A.1 General Features of the Methods

Since the present project represents a venture into a rather novel and complicated problem to which numerical techniques have (as far as I have been aware) not previously been applied, or have at least not been carried very far, a major part of the effort has gone into the development and computer programming of numerical methods for carrying out the calculations. The most useful reference has been the book by Richtmyer (1957), which describes the methods which have become fairly standard for fluid dynamical problems with spherical symmetry. The application of these methods to an astrophysical problem similar in some respects to the present one has been described by Christy (1964, 1967). The methods used in the present project are similar in fundamental respects to those described by Richtmyer and Christy, but it has been found necessary, particularly for the later stages of the collapse, to modify the standard techniques and even to develop some new ones. As Christy remarks, the development of numerical methods for such problems is still something of an art, and it was sometimes only after some experience that a satisfactory approach was found. In the following we shall describe only the methods which were finally adopted as consistent and reasonably satisfactory.

The basic feature of the numerical methods is that the whole protostar is imagined to be divided into a set of concentric shells, the shell boundaries being defined by a specified set of values of the independent space variable. In the Lagrangian formulation the shell boundaries are surfaces of constant m and they move with the flow, so that each shell always contains the same material. In the Eulerian case the shell boundaries are surfaces of constant r and remain fixed in space as material flows across them. In both cases, the variables r, m, u, and L are assigned values on the shell boundaries; values of these variables will be denoted by r_i, m_i, u_i, and L_i, where $i = 1 \ldots N$, $i = 1$ representing the center and $i = N$ the outer boundary. The remaining variables, namely the density and temperature and functions thereof, are specified at a second set of points mid-way between the shell boundaries; values of these variables are denoted $V_{i-\frac{1}{2}}$, $T_{i-\frac{1}{2}}$, $P_{i-\frac{1}{2}}$, $E_{i-\frac{1}{2}}$, etc., where $i = 2 \ldots N$.

The advantage of this scheme is that it corresponds to a simple physical model in which the continuous flow field is approximated by a series of discrete shells, each of which is assigned a particular mass, density, temperature, etc. This allows the difference equations to be written in a simple and physically significant way; for example, the specific volume $V_{i-\frac{1}{2}}$ assigned to a particular shell is expressed simply as the ratio of the volume of the shell to its mass. Experience suggests that for an exploratory project like the present one, it is safest to use a numerical method which adheres fairly closely to a simple physical interpretation; then one is less likely to encounter unphysical numerical difficulties of purely mathematical origin.

We suppose all quantities to be known at a particular instant t^n; the basic problem in the calculations is then to calculate new values for all variables at a later time $t^{n+1} = t^n + \Delta t$. The differential equations as given in section 6 relate the time derivatives of certain variables to expressions containing spatial derivatives. The first necessity is therefore to construct difference approximations to these spatial derivatives. The method of doing this is somewhat different in the Lagrangian and Eulerian cases, and we shall describe the two cases separately in the following sections. Suitable difference equations must then be constructed relating the changes in the variables between times t^n and t^{n+1} to the approximate expressions for the time derivatives at these two times.

To illustrate the possible time differencing procedures, consider as a simple example the differential equation $\partial r/\partial t = u$. The left-hand side of this equation is straightforwardly approximated by the difference expression $(r^{n+1} - r^n)/\Delta t$, where the superscript n denotes the value at time t^n. If we equate this expression to u^n, r^{n+1} may be calculated directly from the known quantities r^n and u^n, and the difference equation is said to be explicit. If however the unknown quantity u^{n+1} or a combination of u^n and u^{n+1} is used, the difference equation is implicit, and new values of the variables can be solved for only by some iterative technique.

The methods commonly used for fluid dynamical problems, as described for example by Richtmyer and Christy, have used difference equations which are effectively explicit. In order to ensure stability of these explicit difference equations, it is necessary to restrict the time step to a value less than the time required for sound to travel between two adjacent shell boundaries. In the present project it was desired to avoid this limitation on the time step, which would have been intolerably restrictive in some phases of the collapse. Therefore we have used only stable implicit differencing schemes.

In the Lagrangian method used in the early stages of this project, the time differencing scheme used was of the form

$$\frac{r^{n+1} - r^{n}}{\Delta t} = \frac{(1+\delta)u^{n+1} + (1-\delta)u^{n}}{2} \tag{A.1}$$

$$\text{where } 0 \leq \delta \leq 1 .$$

This type of difference equation is theoretically stable for any time step. If $\delta = 0$, the right-hand side is just the average of u^n and u^{n+1}, and the equation is accurate to second order in the time step. The use of a finite δ, although it detracts slightly from the accuracy, was found to be desirable in order to damp out small errors and perturbations which inevitably arise in the calculations; with $\delta = 0$ these perturbations are not necessarily damped, and they may cause some "rough sailing" in the calculations. When a finite δ is used the coefficient of u^n in eqn. (A.1) is reduced, so that the effect of any error in u^n is less strongly felt at time t^{n+1}. In most of the calculations a δ of about 0.2 or 0.3 was used, although it was later found that a value as large as 1 could be used to advantage without causing any large error in the results.

The more strongly implicit equations obtained with a finite δ also have the effect of damping out perturbations of physical origin, such as the very complicated radial pulsations which arise in the central core after it stops collapsing. Damping of these pulsations is desirable because computing them in detail would be time consuming and not particularly worthwhile for the present purposes.

In the Eulerian case, partly for simplicity and partly because of experience with the Lagrangian method, a purely implicit form of the difference equations was used, corresponding to $\delta = 1$ in eqn. (A.1). Thus for example the difference equation corresponding to the differential equation (6.6) has the form

$$\frac{m^{n+1} - m^{n}}{\Delta t} = -\left(\frac{4\pi r^{2} u}{V}\right)^{n+1} . \qquad (A.2)$$

(Since most of the quantities occurring in the equations will be evaluated at time t^{n+1} we shall henceforth omit the superscript n+1.) In general, experience suggests that in a project such as the present one, where unforeseen numerical problems are numerous and high accuracy is not an important consideration, the completely implicit form of the difference equations as exemplified by eqn. (A.2) is the best one to use.

Shock fronts have been treated in the calculations by the von Neumann-Richtmyer artificial viscosity method as described by Richtmyer (1957). This method involves adding to the thermal pressure P an artificial pseudo-viscous pressure Q, which provides a macroscopic analog of the molecular level processes determining the actual shock structure. The effect of this term is to change the shock front from a discontinuity into a smooth transition extending over several adjacent mass zones, which can then be calculated with adequate accuracy using the normal difference equations. This allows shock fronts to be handled automatically wherever they may arise, without the need for any special treatment.

A.2 The Lagrangian Difference Equations

The Lagrangian method was the first one used in the calculations, because it is the standard method and because it has some definite advantages over the Eulerian method, as has been discussed by Richtmyer (1957). We give below the complete difference equations finally adopted corresponding to the Lagrangian differential equations (6.1) - (6.5). In the following equations P' denotes the total pressure $P + Q$, and $m_{i+\frac{1}{2}}$ is defined as $\frac{1}{2}(m_i + m_{i+1})$.

$$\frac{r_i - r_i^n}{\Delta t} = \tfrac{1}{2}(1 + \delta)u_i + \tfrac{1}{2}(1 - \delta)u_i^n \qquad \text{(A.3)}$$

$$\begin{aligned}\frac{u_i - u_i^n}{\Delta t} &+ \tfrac{1}{2}(1+\delta)\left[\frac{Gm_i}{r_i^2} + 4\pi r_i^2 (P'_{i-\frac{1}{2}}P'_{i+\frac{1}{2}})^{\frac{1}{2}} \frac{\ln P'_{i+\frac{1}{2}} - \ln P'_{i-\frac{1}{2}}}{m_{i+\frac{1}{2}} - m_{i-\frac{1}{2}}}\right] \\ &+ \tfrac{1}{2}(1-\delta)\left[\frac{Gm_i}{(r_i^n)^2} + 4\pi (r_i^n)^2 (P'^n_{i-\frac{1}{2}}P'^n_{i+\frac{1}{2}})^{\frac{1}{2}} \frac{\ln P'^n_{i+\frac{1}{2}} - \ln P'^n_{i-\frac{1}{2}}}{m_{i+\frac{1}{2}} - m_{i-\frac{1}{2}}}\right] = 0 \qquad \text{(A.4)}\end{aligned}$$

$$\begin{aligned}\frac{E_{i-\frac{1}{2}} - E^n_{i-\frac{1}{2}}}{\Delta t} &+ (P'_{i-\frac{1}{2}}V_{i-\frac{1}{2}}P'^n_{i-\frac{1}{2}}V^n_{i-\frac{1}{2}})^{\frac{1}{2}} \frac{\ln V_{i-\frac{1}{2}} - \ln V^n_{i-\frac{1}{2}}}{\Delta t} \\ &+ \tfrac{1}{2}(1 + \delta)\frac{L_i - L_{i-1}}{m_i - m_{i-1}} + \tfrac{1}{2}(1 - \delta)\frac{L_i^n - L_{i-1}^n}{m_i - m_{i-1}} = 0 \qquad \text{(A.5)}\end{aligned}$$

$$V_{i-\frac{1}{2}} = \frac{4\pi}{3} \frac{r_i^{\,3} - r_{i-1}^{\,3}}{m_i - m_{i-1}} \tag{A.6}$$

$$L_i = \frac{256\,\pi^2\sigma}{3} r_i^{\,4} \left(\frac{T_{i-\frac{1}{2}}^{\,3}}{\kappa_{i-\frac{1}{2}}} \frac{T_{i+\frac{1}{2}}^{\,3}}{\kappa_{i+\frac{1}{2}}} \right)^{\frac{1}{2}} \frac{T_{i-\frac{1}{2}} - T_{i+\frac{1}{2}}}{m_{i+\frac{1}{2}} - m_{i-\frac{1}{2}}} \tag{A.7}$$

where

$$P'_{i-\frac{1}{2}} = P_{i-\frac{1}{2}} + Q_{i-\frac{1}{2}} \,,$$

$$Q_{i-\frac{1}{2}} = \begin{cases} C \dfrac{(u_{i-1} - u_i)^2}{V_{i-\frac{1}{2}}} & \text{if } u_{i-1} - u_i > 0 \\ 0 & \text{otherwise} \;. \end{cases} \tag{A.8}$$

In equation (A.8) C is an arbitrary constant of order unity which determines how many mass zones a shock front is spread out over. Satisfactory results were obtained with a value for C of about 3; shock fronts were then spread out over about 2 or 3 mass zones.

In the difference approximation for the pressure gradient employed in equation (A.4) we have replaced $\partial P/\partial m$ by $P\, \partial \ln P/\partial m$ and applied the differencing to $\ln P$ instead of to P itself. This was done because circumstances are encountered in the calculations where P varies by an order of magnitude or more between adjacent shells; in such cases a straight difference of the form $P_{i+\frac{1}{2}} - P_{i-\frac{1}{2}}$ no longer represents even approximately the pressure gradient at the shell boundary i, whereas the logarithmic difference still retains some validity as an approximation to the pressure gradient. The logarithmic difference formula is accurate if $\ln P$ varies nearly linearly with m; while this is not always a good approximation, it seems that the logarithmic difference formula is probably the best simple formula for general use in a wide range of circumstances, particularly where large variations between adjacent shells may occur.

The same type of logarithmic difference formula has been used to represent $\partial V/\partial t$ in eqn. (A.5). For rather similar reasons, differencing has been applied to T rather than to T^4 in eqn. (A.7); T^4 may vary by more than an order of magnitude between adjacent shells, whereas T varies more slowly and in general more nearly linearly with m. Also, wherever a mean of quantities in adjacent shells or at successive time points is required, the geometric mean rather than the arithmetic mean has been used, since the geometric mean is in general more accurate than the arithmetic mean when quantities vary by a large factor between adjacent shells.

The difference equations must be modified slightly at the outer boundary, depending on the form of the boundary conditions. If the boundary conditions consist of a specification of the boundary pressure P_N and the boundary temperature T_N, equations (A.4) and (A.7) are modified for $i = N$ by replacing the subscript $N + \frac{1}{2}$ by N. If the boundary conditions include a specification of r_N or u_N, equations (A.3) and (A.4) simply drop out for $i = N$.

We consider now the procedure for solving the difference equations. We note that only 3 of the equations contain time differences; correspondingly we need solve explicitly for new values of only 3 of the unknowns, for example r, u, and T. If values of these variables are given at all points, values of the remaining unknowns V and L may be calculated from the remaining equations (A.6) and (A.7), regarded as auxiliary relations. Since r_i is simply related to u_i by eqn. (A.3), we can further reduce the number of basic unknowns to 2, which we take as u and T. We then have two basic difference equations (A.4) and (A.5), and the remaining 3 difference equations take the status of auxiliary relations.

Considering the difference equations for all shells, we then have a system of $2N - 2$ equations in the $2N - 2$ unknowns $u_2 \ldots u_N$ and $T_{1\frac{1}{2}} \ldots T_{N-\frac{1}{2}}$. (If u_N is given, we have $2N - 3$ equations in $2N - 3$ unknowns.) We have solved these equations by the standard technique for such problems, namely Newton's iterative method for calculating successive corrections to an initial approximation to the solution. This is the same technique used in Henyey's method for stellar interiors, and the principles are described for example by Larson and Demarque (1964). The procedure involves solving a set of linear equations whose coefficients are partial derivatives of the difference expressions with respect to the unknowns. Calculation of the partial derivatives is straightforward, but the expressions for them are rather lengthy and will not be reproduced here. In solving the linear equations a special routine must be written to take account of the special structure of the matrix of coefficients, in which elements occur only near the diagonal, but the procedure is again quite straightforward and need not be described in detail here.

In providing first approximations to the new values of u and T at time t^{n+1}, the procedure generally used has been to extrapolate u one time step ahead using the difference approximation to $\partial u/\partial t$ at time t^n; thus the first approximation to u^{n+1} is taken to be $u^n + (\partial u/\partial t)^n \Delta t$. The temperature is not extrapolated, so that the first approximation to T^{n+1} is just T^n. Other procedures involving varying degrees of extrapolation of u and T have been tried, but they have in general been found to provide no advantage over the above procedure.

Because of the low level of accuracy sought in these calculations, it was not necessary to require a high degree of convergence for the iterations. It was found that if the iterations were continued until the last corrections were of the order of 5% or less, the difference equations were nearly always solved to an accuracy of better than 1%. This was a negligible source of error in the results, as was verified by some calculations made with a higher degree of convergence. Typically about 2 or 3 iterations per time step were required to produce this degree of convergence.

A.3 Space and Time Steps for the Lagrangian Method

As has been discussed in section 7.1, it was not thought worthwhile in this project to seek results of high numerical accuracy. Also, it was desired to be able to carry through the calculations without using large amounts of computer time, so that a variety of different cases could be tried. Therefore the calculations have been made with rather coarse space and time steps, usually as large as seemed reasonable without leading to serious inaccuracies. An accuracy of the order of 10 - 20% in most quantities was aimed at, and as is discussed later in section A.7, it is believed that accuracies of this order were in fact generally attained.

We consider first the Lagrangian mass division. It seemed most reasonable to set the shell masses initially at equal intervals in the radius r, i.e., since the density is initially uniform, at equal intervals in $m^{1/3}$. The shell masses are then much smaller near the center than in the outer parts of the cloud; this turns out to be desirable because a situation soon arises in which the physical variables near the center change by large amounts over a small range in mass. In most of the calculations an initial division into 20 shells was used. With this mass division, it turns out somewhat fortunately to be possible to calculate the collapse with fairly good accuracy without altering the mass division until the central density has risen several orders of magnitude above its initial value.

When the calculations are carried further, one finds that not only the physical variables such as density and pressure but also the shell radii r_i change by a large factor between adjacent shells. Under such conditions the error in the difference equations becomes large unless a finer mass division is introduced. It appeared that the best criterion for the insertion of new shell boundaries would be the change of r_i by more than some specified factor between adjacent shell boundaries. Usually a new shell boundary was interpolated between two adjacent shell boundaries whenever they differed in radius by more than a factor of 2. The value of m at the new shell boundary was taken such as to divide the old shell into equal intervals in $m^{1/3}$, and the new radius value was set equal to the geometric mean of the neighboring radius values. New values of the velocity and temperature were interpolated using linear and parabolic interpolation respectively. The interpolation procedure of course requires slight modification when new points are inserted right at the center.

After the formation of a central core bounded by a shock front, the shell boundaries become very closely crowded together inside the shock front and it becomes necessary to delete many of them to avoid an excessive number of mass shells. Accordingly in the calculations shell boundaries were deleted whenever the distance Δr between them became smaller than a rather arbitrary value considered adequate to ensure reasonable accuracy. In practice the insertion and deletion of mass points was found to be one of the more troublesome aspects of the Lagrangian calculations, since it can cause non-negligible perturbations to the dynamics if not carefully done. After some experience a procedure was arrived at which was more or less satisfactory in all of the circumstances encountered, but it was not possible to eliminate completely the perturbations to the dynamics.

At the final stage reached with the Lagrangian calculations, i.e. soon after the formation of the final stellar core, the number of mass shells was about 50. These 50 shells cover about 7 orders of magnitude in radius and 18 orders of magnitude in density.

We discuss now the choice of time step. During the phases of rapid collapse at the center the numerical calculations work well with quite large time steps, and it is desirable to impose some time step limitation for the sake of accuracy. It was thought reasonable to limit the time step so that the central density does not increase by more than a factor of 3 in one time step. While this might seem a large factor, experience has shown that adequate accuracy was nevertheless maintained. The time step was controlled simply by monitoring the extrapolated value of r^{n+1} near the center and reducing the time step until the extrapolated change in r was small enough (as determined empirically) to produce the desired change in density.

When there is a nearly stationary central core bounded by a shock front, the most rapid changes occur in those mass shells just passing through the shock front. A practical upper limit on the time step then arises from the fact that the Lagrangian method always requires at least 2 or 3 time steps to compute the passage of each mass shell through the shock front. If it is attempted to use a larger time step, the changes occurring in one time step become so large that the iterative method used for solving the difference equations fails to converge. Since it appeared that adequate accuracy was attained using the maximum time step possible in these circumstances, the time step was usually made approximately the maximum consistent with good convergence. One obvious condition on the time step which must be satisfied to ensure convergence is that the extrapolated positions of the shell boundaries must not be allowed to cross over or come unreasonably close together. It was found that if the time step was limited so that the extrapolated distance between neighboring shell boundaries was never allowed to decrease by more than a factor of 5 in one time step, this was usually sufficient to ensure good convergence without making the time step unnecessarily small. If at any time the iterations still failed to converge, the time step was automatically reduced until convergence was achieved. A simple and reasonably efficient procedure was found to be to allow a maximum of 4 iterations; if adequate convergence was still not achieved after 4 iterations, the time step was reduced by a factor of about 0.8 and the iterations were repeated. If on the other hand convergence was achieved after only 2 iterations, the time step was subsequently increased by about 20%, if this was allowed by the other time step limits.

The number of time steps required to cover the early stages of the collapse, i.e. up to the formation of the final stellar core, varied from about 50 to 200, depending on the circumstances. In the latter case most of the time steps went into calculating the passage of mass shells through the first (outer) shock front. The execution time required on the IBM 7094 averaged close to one second per time step.

A.4 The Eulerian Difference Equations

The use of an Eulerian method for calculating the early stages of the collapse was not originally contemplated; it was only after an Eulerian method had been developed for the later stages of the collapse that it was decided to try applying it to the early stages for comparison with results already calculated with the Lagrangian method. As it turned out, the Eulerian method proved to have some important advantages of its own; also, the use of an Eulerian method for the early stages as well as the later stages of the collapse provides a consistent method of calculation throughout. Therefore most of the results presented in section 7 have in fact been calculated with the

Eulerian method.

We give below the difference equations finally adopted to approximate the Eulerian differential equations (6.6) - (6.10). As was discussed in section A.1, in the Eulerian case the completely implicit form of the difference equations has been used. In the following equations P' again denotes $P + Q$, and $r_{i+\frac{1}{2}}$ is defined as $\frac{1}{2}(r_i + r_{i+1})$.

$$\frac{m_i - m_i^n}{\Delta t} = - \frac{4\pi r_i^2 u_i}{(V_{i-\frac{1}{2}} V_{i+\frac{1}{2}})^{\frac{1}{2}}} \tag{A.9}$$

$$\frac{u_i - u_i^n}{\Delta t} + u_i \left(\frac{u_{i+1} - u_i}{r_{i+1} - r_i} \right) + \frac{Gm_i}{r_i^2}$$

$$+ (P'_{i-\frac{1}{2}} V_{i-\frac{1}{2}} P'_{i+\frac{1}{2}} V_{i+\frac{1}{2}})^{\frac{1}{2}} \frac{\ln P'_{i+\frac{1}{2}} - \ln P'_{i-\frac{1}{2}}}{r_{i+\frac{1}{2}} - r_{i-\frac{1}{2}}} = 0 \tag{A.10}$$

$$\frac{E_{i-\frac{1}{2}} - E^n_{i-\frac{1}{2}}}{\Delta t} + (P'_{i-\frac{1}{2}} V_{i-\frac{1}{2}} P'^n_{i-\frac{1}{2}} V^n_{i-\frac{1}{2}})^{\frac{1}{2}} \frac{\ln V_{i-\frac{1}{2}} - \ln V^n_{i-\frac{1}{2}}}{\Delta t}$$

$$+ u_i \left[\frac{E_{i+\frac{1}{2}} - E_{i-\frac{1}{2}}}{r_{i+\frac{1}{2}} - r_{i-\frac{1}{2}}} + (P'_{i-\frac{1}{2}} V_{i-\frac{1}{2}} P'_{i+\frac{1}{2}} V_{i+\frac{1}{2}})^{\frac{1}{2}} \frac{\ln V_{i+\frac{1}{2}} - \ln V_{i-\frac{1}{2}}}{r_{i+\frac{1}{2}} - r_{i-\frac{1}{2}}} \right]$$

$$+ \frac{3}{4\pi} V_{i-\frac{1}{2}} \frac{L_i - L_{i-1}}{r_i^3 - r_{i-1}^3} = 0 \tag{A.11}$$

$$\frac{1}{V_{i-\frac{1}{2}}} - \frac{3}{4\pi}\,\frac{m_i - m_{i-1}}{r_i^{\,3} - r_{i-1}^{\,3}} = 0 \tag{A.12}$$

$$L_i = \frac{64\pi\sigma}{3}\; r_i^{\,2}\left(\frac{V_{i-\frac{1}{2}}T_{i-\frac{1}{2}}^{\,3}}{\kappa_{i-\frac{1}{2}}}\;\frac{V_{i+\frac{1}{2}}T_{i+\frac{1}{2}}^{\,3}}{\kappa_{i+\frac{1}{2}}}\right)^{\frac{1}{2}}\frac{T_{i-\frac{1}{2}} - T_{i+\frac{1}{2}}}{r_{i+\frac{1}{2}} - r_{i-\frac{1}{2}}} \tag{A.13}$$

where

$$P'_{i-\frac{1}{2}} = P_{i-\frac{1}{2}} + Q_{i-\frac{1}{2}}$$

$$Q_{i-\frac{1}{2}} = \begin{cases} C\,\dfrac{(u_{i-1} - u_i)^2}{V_{i-\frac{1}{2}}} & \text{if } u_{i-1} - u_i > 0 \\[2ex] 0 & \text{otherwise .} \end{cases} \tag{A.14}$$

In the Eulerian case satisfactory results were obtained with $C = 1$ in most cases; again this gave shock fronts which were spread out over about 2 or 3 mass shells.

In these equations logarithmic differences and geometric means have been used in the same way and for the same reasons as in the Lagrangian case. Apart from equation (A.9), which we shall discuss below, the principal difference from the Lagrangian equations is that additional terms occur in equations (A.10) and (A.11), representing the transport of momentum and energy respectively across the fixed shell boundaries. The form adopted for these terms is the one recommended by Richtmyer (1957) for $u_i < 0$, i.e. for an inward flow of material. For $u_i > 0$ a different form must be used to ensure stability; fortunately, however, positive velocities are found not to occur in the Eulerian calculations, so we need not be concerned with this problem here. These difference expressions for the transport term are accurate only to first order in the space step Δr, unlike the other spatial difference terms which are accurate to second order in Δr. As Richtmyer shows, however, other more accurate forms which one might think of using are unstable and therefore cannot be used; thus a certain loss in accuracy seems to be an unavoidable disadvantage of the Eulerian method.

The use of equation (A.9) requires some discussion, since this equation was found in practice to produce unstable behavior in the freely infalling material just outside the shock front bounding a stationary core. The density of this material is determined mainly through the continuity equation (A.9), and since this equation contains only the product of the densities in adjacent shells, it allows errors of opposite sign to arise in neighboring density values. For this reason the following stable but less accurate difference equation was tried in place of eqn. (A.9):

$$\frac{m_i - m_i^n}{\Delta t} = - u_i \frac{m_{i+1} - m_i}{r_{i+1} - r_i} = - \frac{4\pi}{3} \frac{r_{i+1}^3 - r_i^3}{r_{i+1} - r_i} \frac{u_i}{V_{i+\frac{1}{2}}} \qquad (A.15)$$

This equation was found however to lead to serious inaccuracies in the shock front bounding the final stellar core, where quantities vary by large factors between adjacent shells. Since eqn. (A.9) is in general more accurate, and since the instability problems were fortunately found not to become very serious during the early stages of the collapse, it was decided to use eqn. (A.9) for these early stages of the collapse.

As in the Lagrangian case, the difference equations must be modified slightly at the outer boundary. In this case, our mechanical boundary condition is $u_N = 0$, so equations (A.9) and (A.10) drop out for $i = N$. In equation (A.13), $T_{N+\frac{1}{2}}$ has been replaced by T_N and $V_{N+\frac{1}{2}}$ has been replaced by $V_{N-\frac{1}{2}}$.

The Eulerian difference equations have been solved by a method quite similar to that used in the Lagrangian case. In the Eulerian case it would be quite complicated to reduce the 3 basic unknown variables to 2, so we have retained 3 unknowns, taken to be u, V, and T. The corresponding basic difference equations are (A.10), (A.11), and (A.12), the remaining two equations being regarded as auxiliary relations. Considering the difference equations for all shells, we then have $3N - 4$ equations in the $3N - 4$ unknowns $u_2 \ldots u_{N-1}$, $V_{1\frac{1}{2}} \ldots V_{N-\frac{1}{2}}$, and $T_{1\frac{1}{2}} \ldots T_{N-\frac{1}{2}}$. These equations have been solved by the same iterative technique as was used for the Lagrangian equations. In the Eulerian case initial approximations to the new values of the variables at the advanced time t^{n+1} have been taken simply as the values of these variables at time t^n, without any extrapolation. This was done partly for simplicity and partly because it appeared that little advantage would be gained by the extrapolation.

A.5 Space and Time Steps for the Eulerian Method

It appeared from experience with the Lagrangian calculations that an important consideration in setting up the division into shells was that the ratio of radii of neighboring shell boundaries should not become too large. On the other hand, this ratio should not be too small either or the number of shells required becomes excessive. In the Eulerian case the shell boundaries are fixed in space, and they can be set up from the start at reasonable intervals in radius, without the need for any insertion or deletion of new shells. For the present purposes the simplest and best procedure appears to be to choose a constant ratio between the radii of neighboring shell boundaries, i.e. to distribute the shell boundaries at equal intervals in $\ln r$. In the Lagrangian case the maximum ratio allowed between neighboring radius values was 2; in the Eulerian case, since the difference equations are less accurate, it is desirable for equivalent accuracy to use a somewhat smaller ratio. A ratio of $\sqrt{2}$ was thought reasonable, and this value has been used in all of the calculations. The number of shells required to cover the necessary 7 orders of magnitude in radius is then about 50.

In all of the calculations, the space grid was set up at the start over the whole required range of r and was used without modification throughout the early stages of the collapse. (This was possible because the required range in r was already known from the Lagrangian calculations.) This means that the initial phases of the collapse are calculated with far more points than necessary at small radii; however the extra computing time thereby required is not a large fraction of the total computing time, and it was not thought worthwhile to modify the program to avoid this situation.

The procedure used for time step control was much the same as in the Lagrangian case. Again during the near free fall phases of the collapse the time step was limited so as not to allow the central density to increase by more than a factor of 3 in one time step. (Since this is the same limitation as was used in the Lagrangian case, while the Eulerian time differencing scheme is less accurate than the Lagrangian one, the Eulerian results for these phases of the collapse are somewhat less accurate. In fact, however the error appears to be mainly one of overall time scale, and is not too serious for our purposes; further discussion of the accuracy will be given in section A.7.) It appeared that after the formation of a nearly stationary core adequate accuracy was attained using the maximum time step consistent with good convergence of the iterative method; accordingly the time step was again determined mainly by the criterion of good convergence, just as in the Lagrangian case.

In the Eulerian calculations one does not encounter the rather severe time step limitation which arose in the Lagrangian case in connection with the passage of the Lagrangian mass shells through a shock front; therefore fewer time steps were usually required in the Eulerian case. Typically 50 to 70 time steps were required for the early stages of the collapse; the average computing time per time step was about 1.5 - 2.0 seconds.

A.6 Comparison of the Lagrangian and Eulerian Methods

In this section we shall summarize the advantages of the Lagrangian and Eulerian methods and discuss the reasons for preferring one method or the other in various applications. We give first the advantages of the Lagrangian method:

(1) The Lagrangian method is more versatile for exploratory work. Different kinds of boundary conditions are more easily incorporated; also, nothing need be known in advance about the mass division required, since mass shells are automatically inserted and deleted as required.

(2) The Lagrangian difference equations are more accurate than the Eulerian ones. The Lagrangian spatial differences are accurate to second order in the space step, compared with only first order in the Eulerian case. Also in our case the Lagrangian time differences are more accurate, although this is not an intrinsic feature of the method.

(3) The Lagrangian difference equations are simpler, and the method of solution is also somewhat simpler, involving only 2 unknowns instead of 3. Hence, other things being equal, the Lagrangian calculations require less computing time per time step than the Eulerian ones, although the difference is not large.

In contrast, the Eulerian method has the following advantages:

(1) In the Eulerian case a suitable space division can be set up from the start and used throughout the calculations without modification.

This eliminates the necessity for insertion and deletion of points, which was sometimes troublesome in the Lagrangian case and unavoidably caused some perturbations and inaccuracies in the calculations.

(2) Disturbances, whether of numerical or physical origin, are more effectively damped out in the Eulerian case. For example, the rebound and complicated radial pulsations of the core as found in the Lagrangian calculations do not occur at all in the Eulerian calculations and hence do not cause trouble or require a long computing time to follow them out. In general, the Eulerian calculations were found to run more smoothly and reliably than the Lagrangian ones.

(3) The Lagrangian method encounters a serious and inescapable time step limitation once a central core has formed: because of the necessity of following in detail the motion of each mass shell as it falls into the core and passes through the shock front, the Lagrangian time step is limited to a value of the order of or somewhat less than the time scale for infall of the material just outside the core. The Eulerian time step, on the other hand, is related to the time scale for change of the overall flow pattern, which after the formation of the core becomes much longer than the time scale for infall of material in the immediate vicinity of the core. In these circumstances, in fact, the Eulerian method is more physically reasonable than the Lagrangian one because it is really the overall flow pattern which is of interest and not the motion of individual particles.

(4) Finally, the Eulerian method appears to have given more accurate results for the strong shock front bounding the final stellar core; in particular, the Eulerian method seems to give a more accurate conversion of kinetic energy to thermal energy in the shock front. The reason for this is not completely clear, and it may be that some modification to the Lagrangian method would give improved results. However it does appear that the Eulerian method has an intrinsic advantage in this respect, since the decrease of kinetic energy and the increase of thermal energy produced by the pseudo-viscosity term are calculated by spatial difference expressions of the same form, whereas in the Lagrangian method the deceleration is produced by a spatial difference expression (the pressure gradient) but the increase of thermal energy involves a time difference. Since space differences are in general much greater than time differences, this may allow uncompensated errors to arise in the Lagrangian case, especially if the shock front covers only very few mass shells.

For the reasons we have outlined, the Lagrangian method appears to be more versatile and more suitable for exploratory work where nothing is known in advance about the nature of the results. It is also probably preferable for the near free fall phases of the collapse, where it can be expected to give better accuracy than the Eulerian method. On the other hand, the Eulerian calculations run more smoothly and reliably than the Lagrangian ones, and in some respects more accurately, without running into unreasonable time step restrictions; thus the Eulerian method seems generally preferable. For these reasons most of the early exploratory calculations, made with difference choices of boundary conditions and other parameters, were done with the Lagrangian method, whereas most of the more final and systematic results described in section 7 have been computed with the Eulerian method.

A.7 Accuracy of the Results

It was hoped in this project to be able to attain numerical accuracies of the order of 20% or so without using large amounts of computing time, and this turned out for the most part to be a reasonable goal. In the course of developing and testing the numerical methods, it was usually possible to get an idea of their accuracy by trying different space and time steps or by comparing results calculated with different forms of the difference equations; if the accuracy was not of the desired order, modifications were made or the step sizes were reduced to improve the accuracy. It appears that the hoped for order of accuracy was usually achieved, and that even in the worst case errors do not exceed about 50%. In fact, even in some of the early attempts where serious errors might have been expected, for example because of very large space or time steps, the errors seem in general to have been moderate, not usually exceeding a factor of 2. Thus there can at least be no doubt about the qualitative or order of magnitude correctness of the results.

The best check on the accuracy of the results is believed to be provided by a comparison of the results obtained with the Lagrangian and Eulerian methods, which are two entirely different and independent

APPENDIX B

NUMERICAL METHODS FOR THE LATER STAGES OF THE COLLAPSE

B.1 General Considerations

It was explained in Appendix A that the time step for the Lagrangian method is limited to a value somewhat less than the free fall time for the material just outside the shock front. In the later stages of the collapse this time becomes as short as a few hours or less, whereas the time required for infall of all the material into the core is of the order of 10^5 years. Thus if the Lagrangian method were to be used, it would require more than 10^9 time steps, or about 100 years of computing time on the 7094. Clearly another method must be found, and it was for this reason that the Eulerian method was first tried. The superiority of the Eulerian method in this respect has already been described in Appendix A.

During the later stages of the collapse it becomes necessary to improve on the pseudoviscosity method for treating the shock front bounding the stellar core. As the collapse proceeds, this shock front becomes stronger and stronger, and if the pseudoviscosity method is used the variation of quantities between adjacent shells in the shock front becomes so extreme that it becomes difficult to believe in the validity of the results. Also, after the shock front is no longer effectively adiabatic one encounters a purely numerical difficulty connected with the rapid increase in opacity with increasing temperature in the shock front. As the shock front moves outward over a particular Eulerian shell and the temperature in this shell rises, the radiative cooling rate drops rapidly because of the increasing opacity. The close balance between the mechanical heating and radiative cooling rates is then upset and the shell heats up essentially in the radiative relaxation time, which is orders of magnitude shorter than the accretion time scale. Thus the time step must be decreased by several orders of magnitude each time a shell passes through the shock front; this is clearly quite inconvenient and time consuming. For these reasons, as well as for the reasons mentioned in section 8.1, we have adopted a shock fitting technique for calculating the shock front.

The physical assumptions and the equations adopted for the shock fitting procedure have been discussed in section 8.1. We have 3 shock jump equations, namely eqns. (8.1), (8.5), and (8.10), relating the values of the flow variables on the two sides of the shock front. The incorporation of these equations into the numerical calculations is in principle straightforward. A special grid point is defined at the position of the shock front, associated with which there are two sets of unknown variables, namely u_1, ρ_1, T_1 and u_2, ρ_2, T_2 in the notation of section 8.1. Adding the 3 shock jump relations to the usual Eulerian difference equations on both sides of the shock front we have enough equations to determine values for all of the unknowns in the problem. The complete set of equations can be solved by the same iterative technique as was outlined in Appendix A for solving the Lagrangian difference equations.

In setting up the details of the computational techniques, it is important to give some consideration to the actual physical situation to be represented. The shock front divides our "collapsing protostar" into two regions of quite different properties. The stellar core inside the shock front is an object in hydrostatic equilibrium, resembling in many respects an ordinary star; at the end of the collapse, in fact, it becomes essentially a conventional pre-main sequence stellar model. The numerical method must be capable of adequately representing the structure of the core at all times, and it must include the relevant physics, such as convective energy transport. To satisfy these requirements, some modifications of technique are required in treating the stellar core. On the other hand, outside the shock front we still have a relatively tenuous gas cloud collapsing nearly in free fall, and the methods used for the early stages of the collapse are still adequate here. Thus the calculation of the later stages of the collapse separates naturally into two problems, namely the structure of the stellar core and the dynamics of the infalling gas cloud, which are to be solved simultaneously but with somewhat different numerical techniques.

For convenience in developing and using the numerical methods, we have treated these two problems separately as far as possible, without worrying at first about the details of the interaction between them. Thus for example in the calculations for the shock front and the stellar core it is assumed that the values of the flow variables just outside the shock front are known from the solution of the infall problem. We shall describe first the methods used for the stellar core and for the infalling cloud, and then we shall describe how they have been coupled together.

B.2 The Stellar Core and Shock Front

The most important consideration in treating the stellar core is to set up some form of shell division capable of adequately representing its structure at all times. The problem is similar in many ways to that of computing a stellar interior model, particularly toward the end of the collapse when the stellar core becomes essentially an ordinary pre-main sequence star. It is necessary for example to use a very fine shell division near the surface of the core; this is because it is essential to represent with reasonable accuracy the structure of the surface layers of the core, where the temperature and density may vary by orders of magnitude over a very small range in radius. The Lagrangian shell division usually used in stellar interiors calculations cannot be used here, so some form of Eulerian scheme must be used.

A reasonable grid structure must be maintained in the stellar core as it expands or contracts by a factor of 10 or more in radius; in particular, the fine spacing required in the surface layers must follow the surface as it expands or contracts in radius. This would be rather impracticable with an ordinary Eulerian scheme, in which the shell boundaries remain fixed in space. Therefore we have adopted a modified Eulerian scheme: the core is divided into a fixed number of shells, such that neighboring shell boundaries always maintain the same ratio of radii but the whole grid structure expands or contracts by a constant scale factor as the core radius R varies. Thus if the radii of the shell boundaries are denoted by r_i, $i = 1 \ldots N$, we have set

$$r_i = Rs_i, \quad i = 1 \ldots N \tag{B.1}$$

where R is the core radius and s_i is a fixed set of numbers suitably distributed between 0 and 1 ($s_1 = 0$, $s_N = 1$). The relation (B.1) is substituted wherever r_i occurs in the difference equations, and R is treated as one of the unknowns to be solved for. The extra equation required to determine this additional unknown is provided by a specification of the mass of the core, which we assume to be known from the solution of the infall problem outside the shock front.

A reasonably satisfactory point distribution for all the circumstances encountered was achieved with a smoothly varying spacing of the s_i values, having a maximum spacing in s_i of 0.1 near $s = \frac{1}{2}$ and smaller spacings near the surface and also near the center of the core. Near the surface the points were spaced at intervals of a factor of 2 in $(1 - s)$, the smallest value of $(1 - s)$ being about .0005. Near the center the points were spaced by factors of $\sqrt{2}$ in s, the smallest value of s being about .005. The close spacing at the center is required to represent the very small region of low entropy which develops at the center of the core. The total number of shells in the core was usually about 26 or 27.

The difference equations which we have used in the stellar core are exactly the same as the Eulerian difference equations which were given in section A.4, i.e. eqns. (A.9) - (A.14). The unstable behavior described in section A.4 in connection with eqn. (A.9) does not occur in the core, so this equation is quite satisfactory for use in the core.

In this case the variables in the difference equations are interpreted slightly differently, since they refer to points in our expandable grid rather than to points strictly fixed in space. Thus u for example denotes the velocity relative to the moving grid points and not the true velocity of the material. As long as the core remains in hydrostatic equilibrium, however, all dynamical effects are negligible anyway, so the difference equations (A.9) - (A.14) remain valid.

Although they are of course negligible when the core is in hydrostatic equilibrium, the acceleration terms in eqn. (A.10) were retained in case a third dynamical collapse phase should occur associated with the pressure ionization of hydrogen. As it turned out, this happened only in Case 4. In this case it was necessary to take account of the difference between u_i and the true velocity at grid point r_i. This was done by replacing u_i in the first term of eqn. (A.10) by $u_i + s_i dR/dt$ and representing dR/dt by a backward time difference of the form $(R - R^n)/\Delta t$.

It was mentioned in section A.4 that the form of the Eulerian difference equations which we have used is recommended only for $u_i < 0$; if $u_i > 0$ these equations become unstable and another form must be used to maintain stability. It turns out that positive values of u_i do in fact occur in the central part of the core during some phases of the collapse. These positive values of u_i are however small, and apparently not large enough to cause any serious instability problems. At any rate, no evidence of serious errors or instabilities was found in the results of the calculations, and there appeared to be no reason to alter the difference equations, even though they are in theory unstable.

In the stellar core one addition to the difference equations is necessary in order to account for convective energy transfer. In writing a difference equation corresponding to the differential equation (8.12) for the convective flux, it is important that $T\,dS = dE + P\,dV$ be represented by the same type of difference expression as was used to represent $\partial E/\partial r + P\,\partial V/\partial r$ in the differential equation (6.8), i.e.

$$dE + P\,dV \rightarrow E_{i+\frac{1}{2}} - E_{i-\frac{1}{2}} + (P_{i-\frac{1}{2}}V_{i-\frac{1}{2}}P_{i+\frac{1}{2}}V_{i+\frac{1}{2}})^{\frac{1}{2}}(\ln V_{i+\frac{1}{2}} - \ln V_{i-\frac{1}{2}}) .$$

The convective luminosity term to be added to eqn. (A.13) can then be written

$$(L_c)_i = -2\pi r_i^{\,2}\alpha v \left[\frac{E_{i+\frac{1}{2}} - E_{i-\frac{1}{2}}}{(V_{i-\frac{1}{2}}V_{i+\frac{1}{2}})^{\frac{1}{2}}(\ln V_{i+\frac{1}{2}} - \ln V_{i-\frac{1}{2}})} + (P_{i-\frac{1}{2}}P_{i+\frac{1}{2}})^{\frac{1}{2}}\right]. \qquad (B.2)$$

This term is to be included only if the expression in square brackets is <u>negative</u>, corresponding to a negative entropy gradient; if the entropy gradient is positive, the material is stable against convection. In order to avoid certain numerical difficulties, the decision on whether or not to include the convective term at a particular grid point has been based on whether or not the entropy gradient at that grid point was negative in the <u>preceding</u> core model. This introduces negligible error in the results, at least for our purposes. The equations (A.9) - (A.14) with the addition of equation (B.2) then provide the complete set of difference equations required for the interior of the stellar core.

At the boundary of the core where $i = N$, the difference equations have been slightly modified by replacing the subscripts $N + \frac{1}{2}$ and $N + 1$ by N. The values of the variables right at the boundary, i.e. u_N, ρ_N, T_N, etc., have been identified with the values of these variables just inside the shock front, as denoted in section 8.1 with a subscript 1. To allow determination of all of the unknowns in the problem, the Eulerian difference equations for the core are supplemented with the 3 shock jump relations, i.e. eqns. (8.1), (8.5), and (8.10). In these equations the values of the variables u, ρ, and T just outside the shock front are assumed to be specified as functions of the shock radius R from a knowledge of the inflow outside the shock front; the details of this will be described later in section B.3. In addition, the difference equation (A.9) must be replaced for $i = N$ by a specification of the total mass m_N of the core, again assumed known from a solution of the inflow problem. We then have a sufficient number of equations to determine values for all of the unknowns in the problem, including R.

B.3 The Infalling Cloud

Outside the shock front, the Eulerian shell structure used for the early stages of the collapse is still satisfactory and has been retained in calculating the later stages of the collapse. In this scheme the shell boundaries are fixed in space and are spaced by factors of $\sqrt{2}$ in radius. If this shell structure is continued to small enough radii, the shock radius R will in general fall within one of the shells; clearly it is unnecessary to retain any complete shells inside this point. The practice followed in the calculations has been to add or delete shell boundaries at small radii (always maintaining a spacing of a factor of $\sqrt{2}$ in r) so that the shock front position always falls within the first shell, i.e. between the first and second shell boundaries.

The treatment of the infall problem is simplified by the fact that the inflow just outside the shock front is always supersonic, so that dynamical effects cannot propagate outward in the flow. Also, the heating effect of the radiation emitted from the shock front is unimportant for the dynamics just outside the shock front, since the material in this region is very nearly in free fall anyway. Thus the dynamical properties of the inflow at a point outside the shock front are nearly independent of whatever happens inside that point; in particular, they are nearly independent of the radius and luminosity of the core. This allows us to solve the inflow problem without an exact knowledge of the core radius and luminosity; for example, we can use the radius and luminosity for the previous time step, without bothering to update them. Thus it is possible at least approximately to separate the calculations for the infalling cloud from those for the stellar core.

To obtain the values of the flow variables at the shock radius R as required for the core calculations, our procedure has been to calculate the values of the flow variables in the innermost shell as if the shock front were not there and then interpolate (or extrapolate) the required values at the position of the shock front. The dependence of the flow variables on radius near the shock front is well represented by simple power law formulas of the form

$$u = u_o r^{-\nu} \quad , \tag{B.3}$$

with similar expressions for ρ, T, and m. Interpolation formulas of this form have been fitted to the values of the variables at the first two grid points and the constants u_o, ν, etc. have been used as inputs for the core calculations. The values used in the core calculations for the inflow variables just outside the shock front are then always the correctly interpolated values at whatever value of the shock radius R comes out of the calculations.

The treatment of the temperature and luminosity just outside the shock front requires a special discussion. The temperature may vary rather rapidly with radius just outside the shock front due to heating of the infalling material by radiation from the shock, and this may make accurate interpolation of the temperature difficult. Since the temperature just outside the shock front is not very important anyway we have just set it equal to the temperature at the mid-point of the first shell. This choice is correct on the average, since the shock front falls on the average at the mid-point of the first shell.

The luminosity emitted from the shock front must be incorporated in some way as a boundary condition in the infall problem. As was discussed in section 8.1, we have assumed this luminosity to be given by

$$L = e^{-\tau} 4\pi R^2 \sigma T_e^{\;4} \tag{B.4}$$

where the factor $e^{-\tau}$ is intended to roughly take account of the reduction in radiative flux due to absorption in a layer of optical depth τ. It is numerically inconvenient to associate this luminosity with a special grid point at the shock radius R, since this causes difficulties when R gets close to one of the regular shell boundaries. Instead, for purposes of calculating the temperature and radiation transfer in the infalling material we have assumed the stellar surface to be located at the innermost shell boundary (which is actually inside the shock radius R) and we have assumed the luminosity to be specified at that point. For τ we have taken the optical depth corresponding to half of the thickness of the first shell, which is the distance between the assumed position of the stellar surface and the point where the temperature outside the shock front is defined. This procedure introduces some small errors during the initial stages of the core accretion process, but the errors become negligible during the later stages.

The difference equations which have been used in the infalling cloud are the same as the Eulerian difference equations used for the early stages of the collapse, i.e. eqns. (A.9) - (A.14), with one exception. As was mentioned in Appendix A, equation (A.9) shows unstable behavior in the infalling cloud but it was retained for the early stages of the collapse because the stable alternative, eqn. (A.15), was not considered sufficiently accurate when applied with the pseudoviscosity method in a strong shock front. In the present case the difference equations are no longer required to represent a strong shock front, and to avoid all possibility of instability problems we have used eqn. (A.15) in place of eqn. (A.9). The difference equations and the method of solution of course require some slight modifications at the inner boundary of the collapsing cloud, but these are fairly straightforward and will not be described here.

B.4 The Time Step Procedure

Ideally the stellar core and the infalling cloud should be solved together, the unknowns all being advanced simultaneously in each time step. In the present method the core and gas cloud calculations have been separated, but one could still effectively advance the core and gas cloud simultaneously in each time step by alternating the corrections in the iterative procedure, i.e. by applying the corrections alternately to the core and to the gas cloud until adequate convergence is obtained for both. This procedure was tried, but it was found to have certain unsatisfactory features, including sometimes poor convergence of the iterations. Therefore it was decided to separate completely the time step calculations for the core and for the infalling cloud and to advance the core and the cloud alternately by one complete time step. The error caused by this procedure is small enough to be negligible for our purposes.

It has been mentioned that the inflow problem is not very sensitive to the exact properties of the core, and that a new solution for the infalling cloud can be calculated to adequate accuracy using the previous values for the core radius and luminosity. Therefore our procedure has been to first advance all quantities in the infalling cloud by one time step, neglecting any changes in the core and shock front during this time. Using the values of the inflow variables at the advanced time, a new solution for the core and shock front at this advanced time is calculated. The main error in this procedure is that the luminosity used in the infall calculations is always one time step behind. Since the luminosity is unimportant for the dynamics anyway, at least within our assumptions, this error has a negligible effect as far as the properties of the core are concerned.

Again the time step for the calculations has been determined mainly by the criterion of good convergence of the iterations. If at any time the iterations for either the core or the gas cloud failed to converge after a reasonable number of iterations (usually 4 or 5), the time step was reduced until convergence was achieved. If on the other hand convergence to good accuracy was achieved after only 2 iterations for both the core and the cloud, the time step was increased. It was found reasonable to change the time step by a factor of about 1.5 in each case. With this procedure the time steps were typically such that the core mass increased by about 10% per time step, unless other effects required a shorter time step. The total number of time steps required for the later stages of the collapse varied from about 130 to 300, depending on the number of physical complications and numerical problems encountered. When all was running well, the computing (execution) time averaged about $2\frac{1}{2}$ seconds per time step.

It may perhaps be mentioned that often all did <u>not</u> run well, and that unexpected numerical difficulties were frequently encountered in the calculations. We shall not describe the gruesome details here. Some of these problems were avoided by using various tricks or small modifications in the computer program, sometimes at a slight expense of accuracy. In some other cases it appeared that substantial modifications to the method would be required to properly eliminate a particular numerical problem. Since this has been only an exploratory project, it was not always considered worthwhile to invest substantial amounts of time in developing new techniques; the calculations were then just pushed through by "brute force" techniques, sometimes involving for example a larger number of time steps than would otherwise be reasonable.

APPENDIX C

THE EQUATIONS OF STATE

As was mentioned in section 2.1, we adopt Gaustad's (1963) composition for the protostellar material. At low temperatures (below about 2000 °K, depending on density) the hydrogen is by assumption essentially all in molecular form. At the low densities relevant at these temperatures the material behaves as a perfect gas, at least as far as the pressure is concerned, and it satisfies the perfect gas law

$$P = \rho \mathcal{R} T \tag{C.1}$$

where $\mathcal{R} = 3.36 \times 10^7$ ergs/gm/deg K for our assumed mixture of molecular hydrogen plus helium and heavier elements.

The calculation of the internal energy of molecular hydrogen is complicated by the fact that at temperatures below about 200 °K the rotational degrees of freedom of the H_2 molecules begin to "freeze out" because of the finite spacing of the rotational energy levels. It is necessary to distinguish between parahydrogen (even rotational quantum numbers) and orthohydrogen (odd rotational quantum numbers), since transitions between these two forms are relatively rare and their relative abundances may not be in accordance with thermodynamic equilibrium. In fact, it is believed that H_2 molecules form as parahydrogen in the ground rotational level (Osterbrock 1962), and it is known that purely radiative transitions between para and ortho forms are highly improbable (Raich and

Good 1964); thus it may be that the protostellar hydrogen remains entirely in the para form, unless collisional processes become sufficiently important to produce a significant amount of orthohydrogen.

The specific internal energy E of para- and orthohydrogen and the equilibrium para-ortho ratio have been tabulated by Woolley et al. (1948). Examination of these data shows that for temperatures of about 300 °K or higher parahydrogen and equilibrium hydrogen have essentially the same internal energy, the dependence of internal energy on temperature being given by a straight line of slope $5/2\,\mathcal{R}$, as expected for a gas with 5 degrees of freedom. For temperatures of about 200 °K or less the curves of E vs. T for parahydrogen and equilibrium hydrogen deviate significantly in opposite directions from this straight line relation, but at a temperature of about 30 °K the two curves converge again to a common curve very close to this same straight line. Since the composition of the protostellar hydrogen is unknown but presumably somewhere between pure para H_2 and equilibrium H_2, we have as a rough approximation represented the dependence of E on T throughout by a straight line of slope $5/2\,\mathcal{R}$, which for the most part is intermediate between the curves for para H_2 and equilibrium H_2. The possible error in this procedure, while not negligible, is not expected to make any major difference to the results.

At temperatures above about 1000 °K the vibrational degrees of freedom of the H_2 molecules start to become excited, and the internal energy rises above the straight line relation mentioned above. We have represented the data of Woolley et al. with a simple quadratic formula for $T \geq 600\ ^{\circ}K$. The complete adopted dependence of specific internal energy on temperature for pure molecular hydrogen is then as follows (CGS units):

$0 \leq T \leq 600$:

$$E(H_2) = 1.031 \times 10^8\ T$$

$T \geq 600$:

$$E(H_2) = 2.99 \times 10^9 + 9.32 \times 10^7\ T + 8.30 \times 10^3\ T^2 \ . \tag{C.2}$$

The dissociation of hydrogen molecules, assuming thermodynamic equilibrium, is governed by the equilibrium equation

$$\frac{P(H)^2}{P(H_2)} = K(T) \ . \tag{C.3}$$

If we define a degree of dissociation y by

$$y \equiv \frac{\rho(H)}{\rho(H_2) + \rho(H)} \tag{C.4}$$

and assume that the degree of ionization remains negligible while the dissociation is taking place, so that we can write $\rho(H_2) + \rho(H) = 0.651\ \rho$, equation (C.3) can be written

$$\frac{y^2}{1-y} = 9.31 \times 10^{-9}\ \frac{K(T)}{\rho T} \ . \tag{C.5}$$

The data for K(T) given by Tsuji (1964) may be represented to good accuracy by the following approximation:

$$\frac{K(T)}{T} = 3.49 \times 10^{8} e^{-52490/T} . \tag{C.6}$$

If we substitute this into eqn. (C.5) we get

$$\frac{y^2}{1-y} = 3.25\, \rho^{-1} e^{-52490/T} . \tag{C.7}$$

This is a simple quadratic equation in y, from which the value of y is readily obtained as a function of ρ and T.

The ionization of hydrogen is governed by the Saha equation (see for example Aller 1963, p. 118), which for our purposes may be written

$$\frac{N(e)^2}{N(H)} = \frac{(2\pi mkT)^{3/2}}{h^3} e^{-\chi_0/kT} . \tag{C.8}$$

We neglect the ionization of all elements other than hydrogen, since this will for our purposes make only a minor difference to thermodynamic properties of the material; we then have $N(e) = N(H^+)$. We also assume, as will be justified below, that dissociation of H_2 molecules is complete by the time ionization becomes important. Then, defining the degree of ionization x by

$$x \equiv \frac{N(e)}{N(H) + N(e)} = \frac{\rho(H^+)}{\rho(H) + \rho(H^+)} \tag{C.9}$$

and putting $\rho(H) + \rho(H^+) = 0.651\,\rho$, the Saha equation (C.8) becomes

$$\frac{x^2}{1-x} = 6.20 \times 10^{-9} \rho^{-1} T^{3/2} e^{-157770/T} . \qquad (C.10)$$

Again this is a simple quadratic equation from which the value of x is readily obtained.

Once the degree of dissociation y and the degree of ionization x have been calculated it is straightforward to express the pressure P and the specific internal energy E in terms of y and x by simply adding up the contributions of the various constituents, including of course the energies of dissociation and ionization. The resulting expressions as used in this project are as follows:

$$P = 2.686 \times 10^7 (1.251 + y + 2x) \rho T \qquad (C.11)$$

$$E = .651(1-y)E(H_2) + 8.06 \times 10^7 (y+x) T$$
$$+ 1.011 \times 10^7 T + 1.395 \times 10^{12} y + 8.48 \times 10^{12} x \qquad (C.12)$$

where $E(H_2)$ is the specific internal energy for molecular hydrogen as given by eqn. (C.2). Equations (C.11) and (C.12) together with equations (C.7) and (C.10) then provide equations of state which are satisfactory under most of the conditions encountered.

At the center of the stellar core, however, we encounter conditions of high density and relatively low temperature, under which the effects of close crowding together of hydrogen atoms become important and the above equations are no longer adequate. One such effect is pressure ionization; it is clear for example that if the mean spacing between atoms becomes of the order of one Bohr radius or less, the electrons can no longer remain bound and the hydrogen becomes ionized. A simple heuristic procedure for taking pressure ionization into account has been suggested by Rouse (1964), who suggests multiplying the right-hand side of the Saha equation by a factor of the form e^{ρ/ρ_o} where the constant ρ_o is approximately the density at which pressure ionization becomes important. The value of ρ_o corresponding to a density of one H atom per sphere of radius a_o (the Bohr radius) is 2.7 gm/cm^3; however, it is likely that pressure ionization becomes important at even larger atomic spacings, and Rouse has considered values up to $3a_o$, corresponding to $\rho_o = 0.1$ gm/cm^3.

A similar situation has been considered by Unsöld (1948) and by Elste and Jugaku (1957); these authors considered the destruction of atomic energy levels by the perturbing effects of nearby ions. According to Unsöld (1948), the ground state of an H atom will be destroyed and the electron will no longer remain bound if a perturbing H^+ ion comes within $6\,a_o$ of the nucleus. The density corresponding to one H^+ ion per sphere of radius $6\,a_o$, assuming for example a half ionized mixture, is .025 gm/cm^3, and the corresponding probability of an atom remaining neutral is given by $e^{-\rho/\rho_o}$ with $\rho_o = .025$ gm/cm^3 (see Elste and Jugaku, 1957). This is similar to the modification of the Saha equation proposed by Rouse, except that a smaller value of ρ_o is suggested. We have arbitrarily adopted $\rho_o = 10^{-1}$ gm/cm^3 and inserted a factor e^{ρ/ρ_o} into the Saha equation, as suggested by Rouse; equation (C.10) then becomes

$$\frac{x^2}{1-x} = 6.20 \times 10^{-9} \rho^{-1} T^{3/2} e^{10\,\rho - 157770/T} . \qquad (C.13)$$

The curves of constant x in a log T - log ρ diagram are illustrated by the dashed lines in Fig. 12 (p. 140); it is evident in this diagram that the degree of ionization increases rapidly with increasing density at densities above about 10^{-1} gm/cm^3.

In addition to pressure ionization, there must also be a pressure dissociation effect for H_2 molecules, and presumably it becomes important at a lower density than the pressure ionization discussed above. We have taken this pressure dissociation effect into account in the same rough way as pressure ionization by inserting a factor e^{ρ/ρ_o} into equation (C.7); we have arbitrarily set $\rho_o = 5 \times 10^{-2}$ gm/cm^3 in this case. The degree of dissociation then increases rapidly with increasing density for densities above about 5×10^{-2} gm/cm^3.

We can now justify our assumption that molecular dissociation and ionization are not simultaneously important. With the modifications to the equations of state described above, the maximum overlap of molecular dissociation and ionization occurs at a density of about 5×10^{-2} gm/cm^3 and a temperature of about 2.5×10^4 °K; at this point the hydrogen is approximately 4% in molecular form and 4% ionized, the rest being in atomic form. The error in the equation of state caused by neglecting this overlap is only of the order of 1% or less and is negligible for our purposes.

In addition to pressure dissociation and ionization, there are other effects of high density which we have not taken into account even approximately, for example the reduction of the ionization potential due to the lowering of the ionization continuum. Also, degeneracy starts to become important at high densities, but this has not been taken into account. For these reasons our equation of state is still not really correct at high densitites; for example, because of the reduction of the ionization potential, the decrease in γ caused by pressure ionization will in reality be less than in our calculations. Thus the brief dynamical collapse at the center of the stellar core which occurs in Case 4 (see p. 133) when pressure ionization reduces γ below $4/3$ may in reality never occur. Fortunately, as is discussed in section 9, the properties of the low entropy material at the center of the core are of little consequence anyway; even the brief dynamical collapse phase found in Case 4 appears to make very little difference to the subsequent evolution of the core. Thus the uncertainties and errors in the equation of state at high densities are unimportant for the present project.

APPENDIX D

ASYMPTOTIC SIMILARITY SOLUTIONS FOR THE ISOTHERMAL COLLAPSE

First we show that from one isothermal collapse solution another "homologous" solution may be obtained simply by changing all the variables by appropriate scale factors. The relevant differential equations are either (6.1), (6.2), and (6.4) or (6.6), (6.7), and (6.9), where T is taken to be a constant. We consider two sets of variables related by constant scale factors as follows:

$$t = C_t t', \quad r = C_r r', \quad u = C_u u', \quad \rho = C_\rho \rho', \quad m = C_m m' .$$

Then it can easily be shown by substituting these relations into the differential equations that if the unprimed variables satisfy the equations, so also do the primed variables provided that

$$C_u = 1, \quad C_t = C_m = C_r, \quad C_\rho = C_r^{-2} . \tag{D.1}$$

Thus at corresponding points in homologous solutions we would have for example $m \propto r$ and $\rho \propto r^{-2}$.

Suppose now that we consider a collapse solution in which the velocity, density, and mass distributions have the same functional forms at all times, differing only by scale factors which vary as a function of time. It can again be shown by substitution in the equations that a solution of this form is possible if the scale factors, which in this case are functions of time, are related in the same way as the

the constant scale factors in the homology relations (D.1). The constant scale factors in (D.1) can all be expressed in terms of a single constant, for example C_r; correspondingly our variable scale factors can all be expressed in terms of a single function of time, which we shall take as the (variable) radius scale factor. Hereafter we shall use the notation $z = z(t)$ for the variable radius scale factor corresponding to C_r in the homology relations. Let $u'(r')$, $\rho'(r')$, and $m'(r')$ represent the invariant functional forms of the velocity, density, and mass distributions; these functions may be thought of as being the actual distributions at some standard instant in time when $z(t) = 1$ and $r = r'$. Using the homology relations, the distributions $u(r)$, $\rho(r)$, and $m(r)$ at an arbitrary time may then be expressed in terms of these invariant functional forms as follows:

$$\begin{aligned} r &= z(t)r' \\ u(r) &= u'(r') \\ \rho(r) &= z(t)^{-2}\rho'(r') \\ m(r) &= z(t)m'(r') \end{aligned} \tag{D.2}$$

The initial and boundary conditions of course do <u>not</u> change with time according to these relations, so it is clear that a solution of this form is valid only as a limiting approximation when we are far enough from the initial instant and from the boundary that the initial and boundary conditions no longer have much influence in the region of interest.

We now substitute the relations (D.2) into the Eulerian differential equations (6.6), (6.7), and (6.9). After some rearrangement and some straightforward substitutions to eliminate m' in favor of u' and ρ', thus reducing the number of equations from 3 to 2, we obtain

$$\left(\frac{r'}{\tau} + u'\right)\frac{du'}{dr'} + 4\pi G\rho'(r' + u'\tau) + \Re T\,\frac{d\ln\rho'}{dr'} = 0$$

$$\frac{du'}{dr'} + \left(\frac{r'}{\tau} + u'\right)\left(\frac{d\ln\rho'}{dr'} + \frac{2}{r'}\right) = 0 \qquad (D.3)$$

where $\tau \equiv -\left(\frac{dz}{dt}\right)^{-1}$ is a fixed (positive) constant independent of both r and t.

We thus have two first order differential equations for the two functions $u'(r')$ and $\rho'(r')$, with one undetermined parameter τ. For further analysis it is convenient to reduce these equations to non-dimensional form by means of the following transformations:

$$x = \frac{r'}{\tau\sqrt{\Re T}}\,, \qquad \xi = \frac{u'}{\sqrt{\Re T}}\,, \qquad \eta = 4\pi G\rho'\tau^2 \,. \qquad (D.4)$$

With these substitutions, equations (D.3) become

$$(x + \xi)\frac{d\xi}{dx} + \frac{d\ln\eta}{dx} + (x + \xi)\eta = 0$$

$$\frac{d\xi}{dx} + (x + \xi)\frac{d\ln\eta}{dx} + (x + \xi)\frac{2}{x} = 0 \qquad (D.5)$$

from which we obtain, solving for $d\xi/dx$ and $d\ln\eta/dx$,

$$\frac{d\xi}{dx} = \frac{(x+\xi)}{x} \frac{2 - \eta x(x+\xi)}{(x+\xi)^2 - 1} \tag{D.6}$$

$$\frac{d \ln \eta}{dx} = \frac{(x+\xi)}{x} \frac{\eta x - 2(x+\xi)}{(x+\xi)^2 - 1} \quad . \tag{D.7}$$

For these two first order differential equations we need two boundary conditions, which may for example be taken as the values of ξ and η at $x = 0$. One of these boundary conditions is obvious, i.e. $\xi = 0$ at $x = 0$; the value of η at $x = 0$ is however unknown, so that we still have one undetermined parameter in the problem. Thus it would appear that we have a whole one-parameter family of solutions satisfying our assumption of invariant functional forms for the velocity and density distributions. We notice however that the expressions for $d\xi/dx$ and $d\ln\eta/dx$ become singular when $(x+\xi) = 1$ unless $\eta x = 2$ at this point. Since this singularity is physically inadmissible, this singles out only one solution and one value of the undetermined parameter as an admissible solution to the problem. Thus the invariant functional forms of the velocity and density distributions, represented by the functions $\xi(x)$ and $\eta(x)$, are uniquely determined.

Even without integrating equations (D.6) and (D.7) numerically, we can easily find the limiting properties of the velocity and density distributions. The limit of interest here is $x \gg 1$, since this is the limit approached at a particular value of r as the collapse progresses and the radius scale factor z decreases. If we put $x \gg 1$ in equation (D.6) we get

$$\frac{d\xi}{dx} = \frac{2}{x(x+\xi)} - \eta \rightarrow 0 \quad \text{for} \quad x \gg 1, \tag{D.8}$$

since η decreases strongly with increasing x. Thus ξ approaches a constant value at large x. This means that as the collapse proceeds the collapse velocity u should approach a constant value independent of r; this is in fact approximately verified in the results of our calculations. Similarly from eqn. (D.7) we obtain for large values of x

$$\frac{d\ln\eta}{d\ln x} = \left(\frac{x}{x+\xi}\right)\eta - 2 \rightarrow -2 \quad \text{for} \quad x \gg 1 \quad . \tag{D.9}$$

Thus we have $\eta \propto x^{-2}$ for large x, implying that the density distribution in the collapsing cloud should approach the form $\rho \propto r^{-2}$; again this is approximately verified in the results of our collapse calculations, as was mentioned in section 7.2 (see Fig. 2, p. 46).

APPENDIX E

PROOF OF EQUATION (8.4)

The following derivation is based on the equation of radiative transfer in the greybody approximation. This equation may be written

$$\cos\theta \frac{dI}{d\tau} = I - S \tag{E.1}$$

where $I = I(\theta)$ is the specific radiation intensity integrated over all frequencies, and S is the source function, assumed isotropic. We define the following moments of the radiation field:

$$H = \frac{1}{4\pi}\int I \cos\theta \, d\omega \ , \quad K = \frac{1}{4\pi}\int I \cos^2\theta \, d\omega \tag{E.2}$$

(see for example Aller 1963, p. 215). Multiplying equation (E.1) by $\cos\theta$ and integrating over ω, we get

$$\frac{dK}{d\tau} = H \ . \tag{E.3}$$

We apply this relation in the region of radiative cooling just inside the shock front. Since the net radiative flux is always outward, we have $H > 0$ and consequently

$$\frac{dK}{d\tau} > 0 \tag{E.4}$$

throughout this region. Hence we must have $K_1 > K_s$, where K_1 is the value of K at r_1 (see Fig. 4, p. 70) and K_s is the value of K right at the shock jump. We assume r_1 to be at a sufficiently large optical depth that the radiation intensity is isotropic and equal to the blackbody intensity $B(T_1)$. We then have $K_1 = \frac{1}{3} B(T_1)$, and since $K_1 > K_s$ we therefore have

$$\frac{1}{3} B(T_1) > K_s . \tag{E.5}$$

We now establish a lower limit for K_s in terms of H_s, the value of H at the shock jump. From equations (E.2) it is clear that the smallest ratio of K to H is obtained when the radiation intensity $I(\theta)$ is largest in a direction nearly perpendicular to the outward normal. In the present situation it is in fact the case that the radiation intensity at the shock jump is largest for θ near $\frac{\pi}{2}$, since most of the radiation comes from a thin layer of high temperature and small optical depth just inside the shock jump. The limiting case is obtained with a thin layer of zero optical depth, in which case $I(\theta) \propto (\cos\theta)^{-1}$. If we substitute this in equations (E.2), neglecting any contribution for $\theta > \frac{\pi}{2}$, we get $K_s = \frac{1}{2} H_s$. This is a lower limit for K_s, and in reality we will have

$$K_s > \frac{1}{2} H_s . \tag{E.6}$$

Finally, making use of the definition of T_e we have

$$H_s = \frac{F_s}{4\pi} = \frac{\sigma T_e^4}{4\pi} = \frac{1}{4} B(T_e) . \tag{E.7}$$

Combining equations (E.5), (E.6), and (E.7) we obtain

$$\frac{1}{3} B(T_1) > \frac{1}{8} B(T_e)$$

or

$$T_1^{\,4} > \frac{3}{8} T_e^{\,4} \;, \quad \text{q.e.d.} \tag{E.8}$$

This derivation has assumed the grey approximation, i.e. the absorption coefficient κ_ν is assumed to be independent of frequency. Unfortunately it does not seem possible to give a correspondingly simple and rigorous derivation in the non-grey case, although it appears unlikely that the result would be changed. The crucial relation on which the proof is based is eqn. (E.4). In the frequency dependent case we can derive a relation analogous to eqn. (E.3), i.e.

$$\frac{dK_\nu}{d\tau_\nu} = H_\nu \quad ,$$

from which we obtain, integrating over all frequencies,

$$dK = \int dK_\nu \, d\nu = - \rho \, dr \int \kappa_\nu H_\nu \, d\nu \; . \tag{E.9}$$

The crucial question is thus whether $\int \kappa_\nu H_\nu \, d\nu$ is always positive. We know that $\int H_\nu \, d\nu$ is positive, but this does not guarantee $H_\nu > 0$ for all ν. In the present situation it seems likely in fact that H_ν will be negative at very high frequencies, since there will be more high frequency radiation travelling inward from the very hot material just inside the shock front than there will be travelling outward from the cooler material farther inside the shock front. Thus if κ_ν should be large at these higher frequencies and small at lower frequencies it is conceivable that $dK/d\tau$ could be negative. This seems unlikely to happen, however, considering that the general trend is for κ_ν to decrease with increasing frequency.

APPENDIX F

CALCULATION OF THE FUNCTIONS $G_n(\tau_\lambda)$

As was mentioned in section 10.2, the functions $G_n(\tau_\lambda)$ are defined by substituting equation (10.5) into equation (10.4); this gives

$$G_n(\tau_\lambda) \equiv \frac{1}{2r}\int_0^r \frac{s\,ds}{\sqrt{r^2-s^2}}\left[\exp\left\{-K_\lambda\int_s^\infty \frac{dr}{r^{n-1}\sqrt{r^2-s^2}}\right.\right.$$

$$\left.\left. -K_\lambda\int_s^r \frac{dr}{r^{n-1}\sqrt{r^2-s^2}}\right\} + \exp\left\{-K_\lambda\int_r^\infty \frac{dr}{r^{n-1}\sqrt{r^2-s^2}}\right\}\right] \qquad (F.1)$$

where τ_λ is related to r by

$$\tau_\lambda = \frac{K_\lambda}{n-1} r^{-n+1} . \qquad (F.2)$$

We consider first the evaluation of the function $G_n(\tau_\lambda)$ for $n = 3/2$. It is necessary first of all to evaluate the integrals occurring in the exponents in equation (F.1). These may be expressed in terms of elliptic integrals by means of the substitution $r = s\sec^2\phi$; we then obtain for example

$$\int_s^r \frac{dr}{\sqrt{r(r^2-s^2)}} = \sqrt{\frac{2}{s}}\int_0^\phi \frac{d\phi}{\sqrt{1-\frac{1}{2}\sin^2\phi}} = \sqrt{\frac{2}{s}}\, F\!\left(\frac{1}{\sqrt{2}}, \phi\right) \qquad (F.3)$$

where $F(k,\phi)$ is the Elliptic Integral of the First Kind. If we apply the same substitution of variables to the other integrals in equation

(F.1) and make use of the fact that $F(k,\phi)$ is an odd function of ϕ, we can write equation (F.1) for $n = 3/2$ in the form

$$G_{3/2}(\tau_\lambda) = \int_{-\frac{\pi}{2}}^{\frac{\pi}{2}} \frac{\cos^3\phi \, d\phi}{\sqrt{1+\cos^2\phi}} \exp\left\{ \frac{\tau_\lambda}{\sqrt{2}\cos\phi} \left[F\left(\frac{1}{\sqrt{2}}, \phi\right) - F\left(\frac{1}{\sqrt{2}}, \frac{\pi}{2}\right) \right] \right\}, \tag{F.4}$$

where we have made use of the relation $\tau_\lambda = 2K_\lambda r^{-1/2}$ valid for $n = 3/2$.

We have used equation (F.4) to calculate the function $G_{3/2}(\tau)$ numerically, using a subroutine available at the Caltech computing center to evaluate the elliptic integrals. The results are tabulated in Table 9 (p.258). We have attempted to find a simple analytic formula to approximate the function $G_{3/2}(\tau)$ with adequate accuracy. For values of τ less than about 2.3 the following approximation is valid to an accuracy of $\frac{1}{2}\%$ or better:

$$G_{3/2}(\tau) \doteqdot \frac{e^{-0.94\tau}}{1+0.594\tau} . \tag{F.5}$$

This simple approximation has been used in place of $G_{3/2}(\tau)$ in most of the calculations. In one case where it was thought that the error in this approximation at large values of τ might have a significant effect on the emitted spectrum, $G_{3/2}(\tau)$ was evaluated essentially exactly by interpolation in a table of $\log G_{3/2}(\tau)$ vs. $\log \tau$. However this was found to make negligible difference to the emitted spectrum.

For comparison we have also calculated the function $G_2(\tau)$. If we substitute $n = 2$ in equation (F.1) and employ transformations similar to those used for $n = 3/2$, we readily obtain

$$G_2(\tau) = \frac{1}{2}\int_0^{\pi} \sin\phi \exp\left\{-\frac{\tau\phi}{\sin\phi}\right\} d\phi . \qquad \text{(F.6)}$$

This integral has been evaluated numerically in the same way as $G_{3/2}(\tau)$, and the results are also given in Table 9. The function $G_2(\tau)$ is less well represented by a simple approximation of the form (F.5) than $G_{3/2}(\tau)$, but since the case $n = 2$ is less important we have considered the following adequate:

$$G_2(\tau) \doteqdot \frac{e^{-0.9\tau}}{1+1.12\tau} . \qquad \text{(F.7)}$$

This approximation is accurate to about 2% or better for $\tau < 2.5$.

It may be noted that the functions $G_{3/2}(\tau)$ and $G_2(\tau)$ are both intermediate between $e^{-\tau}$ and the second exponential integral $E_2(\tau)$. In fact, $G_{3/2}(\tau)$ is roughly the geometric mean of $e^{-\tau}$ and $E_2(\tau)$, and $G_2(\tau)$ is roughly the geometric mean of $G_{3/2}(\tau)$ and $E_2(\tau)$. It can be shown that in the limit of large n the function $G_n(\tau)$ approaches $\frac{1}{2}E_2(\tau)$. This is easily understood physically, since for large n the density and optical depth increase very rapidly with decreasing radius, so that only a small range of radii is important and we approach the plane atmosphere limit. With $G(\tau) = \frac{1}{2}E_2(\tau)$, equation (10.2) then becomes identical with equation (10.1), as expected. On the other hand, as n approaches 1 we approach the limit of an infinite spherical "atmosphere," and $G_n(\tau)$ approaches $e^{-\tau}$.

TABLE 9

τ	$G_{3/2}(\tau)$	$G_2(\tau)$
0.0	1.000	1.000
0.1	8.573-1	8.072-1
0.2	7.385-1	6.688-1
0.3	6.385-1	5.614-1
0.4	5.538-1	4.754-1
0.5	4.815-1	4.051-1
0.6	4.195-1	3.469-1
0.7	3.662-1	2.983-1
0.8	3.202-1	2.574-1
0.9	2.804-1	2.227-1
1.0	2.459-1	1.932-1
1.2	1.897-1	1.463-1
1.4	1.470-1	1.116-1
1.6	1.143-1	8.555-2
1.8	8.911-2	6.591-2
2.0	6.967-2	5.099-2
2.2	5.460-2	3.959-2
2.6	3.374-2	2.407-2
3.0	2.099-2	1.478-2
3.4	1.313-2	9.141-3
3.8	8.257-3	5.692-3
4.2	5.213-3	3.563-3
4.6	3.303-3	2.241-3
5.0	2.100-3	1.415-3
5.8	8.555-4	5.703-4
6.6	3.517-4	2.323-4
7.4	1.457-4	9.552-5
8.2	6.074-5	3.956-5
9.0	2.546-5	1.649-5
9.8	1.072-5	6.911-6
10.6	4.533-6	2.910-6

REFERENCES

Aller, L. H. 1963, *The Atmospheres of the Sun and Stars* (New York: Ronald Press), ch. 5.

Becklin, E. E., and Neugebauer, G. 1967, Ap. J., 147, 799.

Bodenheimer, P. 1965, Ap. J., 142, 451.

Bodenheimer, P. 1966a, Ap. J., 144, 103.

Bodenheimer, P. 1966b, Ap. J., 144, 709.

Bonnor, W. B. 1956, M. N., 116, 351.

Bonnor, W. B. 1957, M. N., 117, 104.

Chapman, R. D. 1966, Ap. J., 143, 61.

Christy, R. F. 1964, Rev. Mod. Phys., 36, 555.

Christy, R. F. 1967, Methods in Computational Physics, *v. 7: Astrophysics*, p. 191.

Cox, A. N. 1966: Unpublished opacity table supplied privately to P. R. Demarque for the composition "Demarque I."

Danielson, R. E., Woolf, N. J., and Gaustad, J. E. 1965, Ap. J., 141, 116.

Davidson, K., and Harwit, M. 1967, Ap. J., 148, 443.

Ebert, R. 1955, Z. Ap., 37, 217.

Elste, G., and Jugaku, J. 1957, Ap. J., 125, 742.

Ezer, D., and Cameron, A. G. W. 1963, Icarus, 1, 422.

Ezer, D., and Cameron, A. G. W. 1965, Can. J. Phys., 43, 1497.

Gaustad, J. E. 1963, Ap. J., 138, 1050; see also unpublished thesis, Princeton University, 1962.

Hartmann, W. K. 1967, Ap. J. Letters, 149, L87.

Hayakawa, S., Nishimura, S., and Takayanagi, K. 1961, Pub. Astr. Soc. Japan, 13, 184.

Hayashi, C. 1966, Annual Review of Astronomy and Astrophysics, 4, 171.

Hayashi, C., Hoshi, R., and Sugimoto, D. 1962, Prog. Theor. Phys. Suppl., No. 22.

Hayashi, C., and Nakano, T. 1965, Prog. Theor. Phys., 34, 754.

Herbig, G. H. 1962, Advances in Astronomy and Astrophysics, 1, 47.

Herbig, G. H. 1967, Scientific American, 217, No. 2, 30.

Hoyle, F., and Wickramasinghe, N. C. 1962, M. N., 124, 417.

Hulst, H. C. van de. 1949, Rech. Astr. Obs. Utrecht, 11, Part 2.

Iben, I. 1965, Ap. J., 141, 993.

Jeans, J. H. 1928, Astronomy and Cosmogony (Cambridge University Press), p. 345.

Johnson, H. L. 1965a, Ap. J., 141, 923.

Johnson, H. L. 1965b, Comm. Lunar and Planetary Lab., 3, 73 (No. 53).

Johnson, H. L., and Borgmann, J. 1963, B. A. N., 17, 115.

Kleinmann, D. E., and Low, F. J. 1967, Ap. J. Letters, 149, L1.

Krishna Swamy, K. S., and O'Dell, C. R. 1967, Ap. J., 147, 937.

Kuhi, L. V. 1966, J. Roy. Astr. Soc. Canada, 60, 1.

Larson, R. B., and Demarque, P. R. 1964, Ap. J. 140, 524.

Liepmann, H. W., and Roshko, A. 1957, Elements of Gasdynamics (New York: Wiley and Sons), ch. 2.

McCrea, W. H. 1957, M. N., 117, 562.

Mendoza, E. E. 1966, Ap. J., 143, 1010.

Osterbrock, D. E. 1962, Ap. J., 136, 359.

Penston, M. V. 1966, Roy. Obs. Bull., No. 117, 299.

Raich, J. C., and Good, R. H. 1964, Ap. J., 139, 1004.

Raimond, E., and Eliasson, B. 1967, Ap. J. Letters, 150, L171.

Richtmyer, R. D. 1957, Difference Methods for Initial Value Problems (New York: Interscience), ch. 10. Since the present project was completed a second edition by R. D. Richtmyer and K. W. Morton has appeared (1967).

Rouse, C. A. 1964, Ap. J., 139, 339.

Seaton, M. J. 1955, Ann. d'Ap., 18, 188.

Tsuji, T. 1966, Pub. Astr. Soc. Japan, 18, 127.

Unsöld, A. 1948, Z. Ap., 24, 355.

Vitense, E. 1953, Z. Ap., 32, 135.

Walker, M. F. 1961, Comptes Rendus, 253, 383.

Walker, M. F. 1963, A. J., 68, 298.

Walker, M. F. 1964, Roy. Obs. Bull., No. 82, p. 69.

Woolley, H. W., Scott, R. B., and Brickwedde, F. G. 1948, U.S.N.B.S. Journal of Research, 41, 379.

Yamashita, Y. 1962, Pub. Astr. Soc. Japan, 14, 390.